MICROCOPY RESOLUTION TEST CHART

NATIONAL BUREAU OF STANDARDS-1963-A

THE OHIO STATE UNIVERSITY

AD-A180 044

RADAR TARGET IDENTIFICATION TECHNIQUES APPLIED TO A POLARIZATION DIVERSE AIRCRAFT DATA BASE

Alex J. Kamis
E.K. Walton
F.D. Garber

The Ohio State University

ElectroScience Laboratory

Department of Electrical Engineering
Columbus, Ohio 43212

DTIC
SELECTE
MAY 0 1 1987
D

87 4 30 107

NOTICES

When Government drawings, specifications, or other data are
used for any purpose other than in connection with a definitely
related Government procurement operation, the United States
Government thereby incurs no responsibility nor any obligation
whatsoever, and the fact that the Government may have formulated,
furnished, or in any way supplied the said drawings, specifications,
or other data, is not to be regarded by implication or otherwise as
in any manner licensing the holder or any other person or corporation,
or conveying any rights or permission to manufacture, use, or sell
any patented invention that may in any way be related thereto.

50272-101

REPORT DOCUMENTATION PAGE	1. REPORT NO.	2.	3. Recipient's Accession No.

AD A 130 044

4. Title and Subtitle	5. Report Date
RADAR TARGET IDENTIFICATION TECHNIQUES APPLIED TO A POLARIZATION DIVERSE AIRCRAFT DATA BASE	March 1987
	6.

7. Author(s) A.J. Kamis, E.K. Walton, F.D. Garber	8. Performing Organization Rept. No. 717220-2

9. Performing Organization Name and Address	10. Project/Task/Work Unit No.
The Ohio State University ElectroScience Laboratory 1320 Kinnear Road Columbus, Ohio 43212	11. Contract(C) or Grant(G) No (C) N00014-85-K-0321 (G)

12. Sponsoring Organization Name and Address	13. Type of Report & Period Covered
Department of the Navy Office of Naval Research 800 N. Quincy Street Arlington, Virginia 22217	Technical
	14.

15. Supplementary Notes

16. Abstract (Limit: 200 words)

This report investigates the performance of several types of multi-frequency radar systems employing a data base of measured monostatic radar signatures as descriptors for Radar Target Identification (RTI). The approach, a Monte-Carlo computer simulation, enables the evaluation of radar systems exploiting various aspects of RTI techniques. These aspects, examined by misclassification percentage curves, are: the number of interrogation frequencies, operating bandwidths, classification algorithm types, larger target aspect zones, and target descriptors called "feature vectors". The data base of radar signatures was obtained at The Ohio State University ElectroScience Laboratory Compact Range facility, and consisted of scale model monostatic calibrated radar measurements from five commercial aircraft. It is shown that the fully-coherent radar feature vectors HH, VV, RR, LL, and RL perform very effectively for target identification with signal to noise ratios of 0 dB. It is also shown that the low-frequency sector of the data base provides good classification performance versus noise power, and that the number of frequencies within a given bandwidth is optimised by Shannon's sampling theorem.

17. Document Analysis   a. Descriptors

b. Identifiers/Open-Ended Terms

c. COSATI Field/Group

18. Availability Statement	19. Security Class (This Report)	21. No. of Pages
Approved for public release; distribution is unlimited.	Unclassified	145
	20. Security Class (This Page) Unclassified	22. Price

(See ANSI-Z39.18)   See Instructions on Reverse

OPTIONAL FORM 272 (4-77)
(Formerly NTIS-35)
Department of Commerce

TABLE OF CONTENTS

QUALITY
INSPECTED
2

/ Codes

Dist | Avail and / or
       Special

A-1

iii

LIST OF TABLES

LIST OF FIGURES

viii

CHAPTER I

INTRODUCTION

Radar Target Identification (RTI) techniques have been developed over the past several years. Work at The Ohio State University (OSU) ElectroScience Laboratory (ESL) has established basic concepts and algorithms that form a wide base of methods for solving the RTI problem [1 - 17]. Research areas have included the investigation of optimal frequency ranges [13], where wavelengths extend from the Rayleigh region to the optical region, and polarization studies [6] involving various linear and non-linear combinations of the radar scattering coefficients. Various identification algorithms have also been analyzed by computer simulation techniques and applied to different radar class structures, such as land vehicles, ocean ships, and aircraft [13 - 17].

Ksienski [1] concluded that the optimal frequency range for radar target identification should lie in the Rayleigh - resonance frequency range where the wavelength is about the same size or larger than the size of the target. In the Rayleigh region the scattered field is descriptive of the shape and volume of the target. In the resonance region the scattered field is due to re-radiating surface currents set up on the target body and also carries target shape and size information. In both of these regions a desired feature for target identification is found; shape and size information and small changes in aspects have little effect on the character of the radar return.

In contrast, in the optical region, where the wavelength is small compared to the target size, small changes in aspects can cause significant changes in the scattering characteristics. The scattering mechanism in the optical region are related to the interaction of the specular points and contain information on the finer details of the target. If the separation of the specular points is large compared the incident wavelength; small changes in aspects cause significant changes in the scattering characteristics.

The ESL has developed a multi-frequency data base consisting of ocean ship, aircraft, and ground vehicle radar signatures, and has explored radar detection methods and various classification methods for each class of targets [5]. The ESL has also been involved with the statistical analysis in system simulations, model developments, and evaluation of system performance by means of Monte Carlo simulations [7].

To apply target identification techniques, one must have a library of information or features (i.e., feature space) describing each target to be identified. The feature space is a multidimensional space containing vector quantities. In the feature space one would like to have linear separability between all the targets, thus forming distinct hyperplanes between elements contained in the feature space. In the case of complex targets, such as aircraft, ships, and ground vehicles, one might attain distinct hyperplanes (i.e., separability between the three classes). However within a class, say of small jet fighters, features creating distinct hyperplanes may be impossible to determine.

For the radar problem, the feature space consists of information contained in the electromagnetic energy return from the scattering object. Information available from this energy spectrum depends on both the transmitter and the scatterer. Features such as the transmitted frequency, received amplitude, transmitted po-

larization, received polarization, and target range, are available to most radar systems. Others features, such as received phase, target speed, target direction, and Radar Cross Section (RCS) can also be obtained.

It is apparent that feature selection is a very important consideration of the radar target identification problem. Of course one would like to have a large catalog of features to choose from in order to make the best possible decision that identifies the target correctly. However, by selecting more features, the complexity of the measurement, the cost of the system, the dimensionality of the classification vector, and the data processing, all increase. To minimize the cost and expedite the decision making process, one needs to select optimum features that meet some level of target identification performance.

The properties of the polarization diverse data base allows the investigation of many new and different radar polarization states by creating circular polarization states and new identification target descriptors known as "feature vectors". With the goal of obtaining additional knowledge on optimal feature selection, this study analyzes the performance of many different radar polarization states, frequency ranges, and the number of frequencies by means of a Monte Carlo simulation. This study also validates earlier results based on optimal RTI methods by analyzing these methods on a more complete and realistic data base of commercial aircraft. With the contents of the report, we hope to give the RTI designer some insight on the tradeoffs and characteristics of the aircraft class of targets.

CHAPTER II

DATA AND DATA BASE FORMAT

2.1 Introduction

In order to implement a Monte Carlo simulation, a data base is required. The data base for this simulation study consists of calibrated complex monostatic radar returns from five metallic coated scale model aircraft: Concord, DC10, 707, 727, and 747. The silhouettes and the full-scale dimensions of these commercial aircraft are shown in Figures 1 through 5.

The data base consists of calibrated complex (coherent) monostatic radar returns measured at various azimuth angles, frequencies, and polarizations, at an elevation and roll angle of 0°. The data was taken at the OSU ESL compact range facility [18] over the frequency bands of 1 to 12 GHz and 18 to 35 GHz (unscaled). Once the data were measured, a sequence of calibration steps were implemented to remove unwanted background clutter and receiver system effects. Using an enhanced sequence of calibration steps, described by Kimball [19], one can obtain an essentially error (noise) free measurement of unscaled coherent radar backscattering information. A brief description of the compact range, measurement squence, calibration steps, and data scaling are provided in the following sections.

4
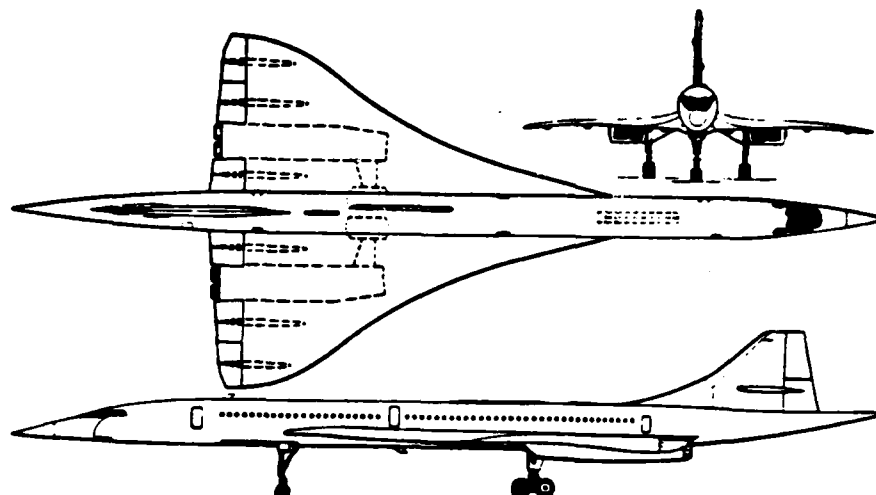
External Dimensions:

Length overall	202 ft	3.6 in (61.66m)
Height overall	40 ft	0.0 in (12.19m)
Wing span	83 ft	10.0 in (25.56m)

Figure 1: Concord Silhouette and Physical Data
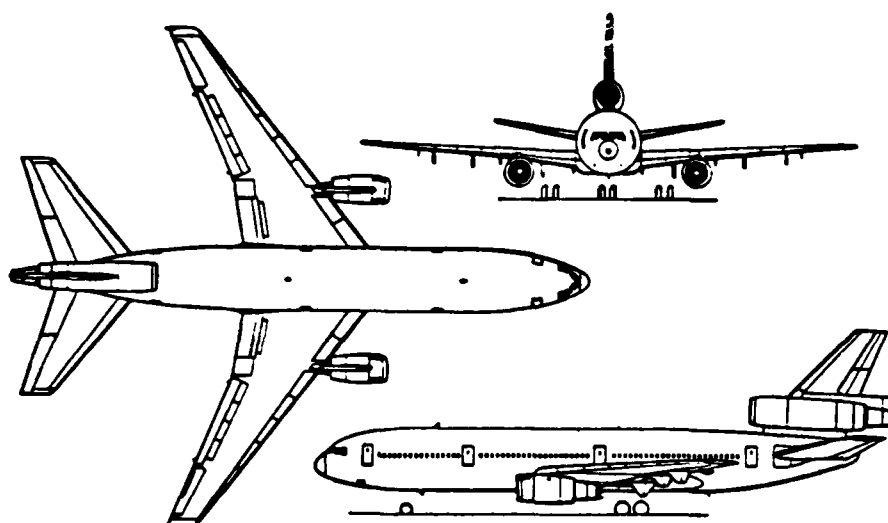
External Dimensions:

Length overall	181 ft	7.2 in (55.35m)
Height overall	57 ft	7.0 in (17.55m)
Wing span	165 ft	4.0 in (50.39m)

Figure 2: DC10 Silhouette and Physical Data
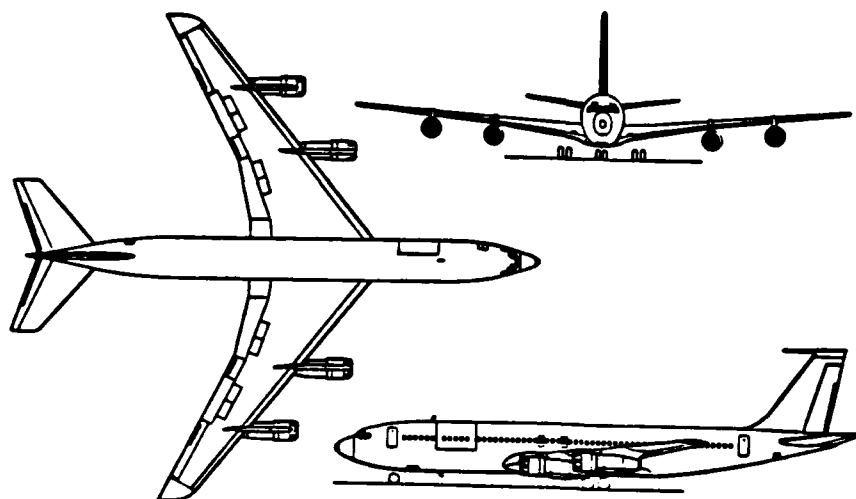
External Dimensions:

Length overall	152 ft 11.0 in (46.61m)
Height overall	42 ft 5.0 in (12.93m)
Wing span	145 ft 9.0 in (44.42m)

Figure 3: 707 Silhouette and Physical Data
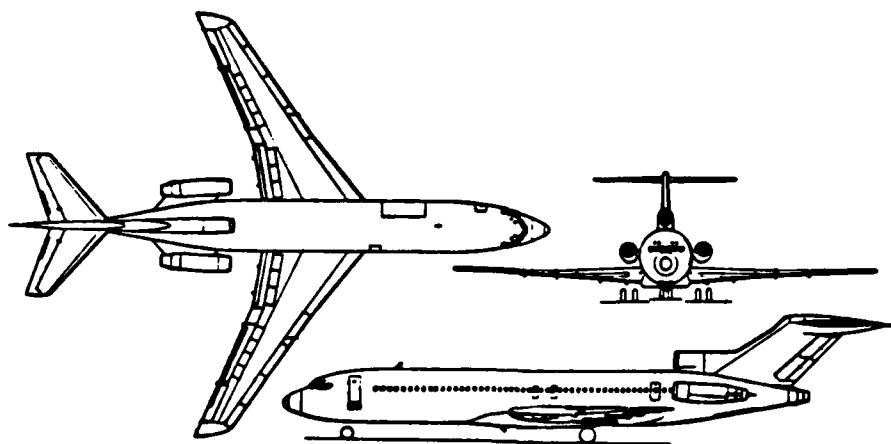
External Dimensions:

Length overall	153 ft 2.0 in (46.69m)
Height overall	34 ft 0.0 in (10.36m)
Wing span	108 ft 0.0 in (32.92m)

Figure 4: 727 Silhouette and Physical Data

6
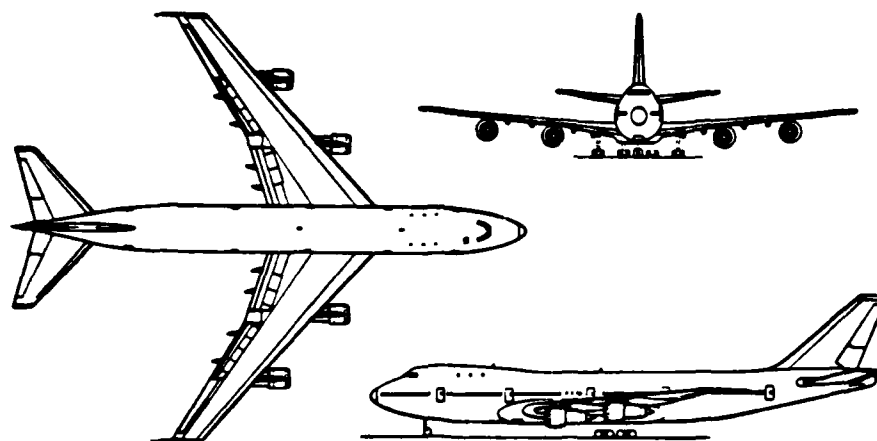
External Dimensions:

Length overall	231 ft	4.0 in	(70.51m)
Height overall	63 ft	5.0 in	(19.33m)
Wing span	195 ft	8.0 in	(59.64m)

Figure 5: 747 Silhouette and Physical Data

2.2 Measurment Facilities

The OSU ESL compact antenna range facility consists of a 60 foot long by 40 foot wide by 20 foot high anachoic chamber. The facility utilizes a Scientific Atlanta (SA) compact range parabolic reflector, a SA 1780 receiver, a Watkins Johnson WJ125OA frequency synthesizer, a Digital Equipment Corporation PDP-11/23 controlling computer, and a low radar cross section target positioner. A block diagram of this arrangement is shown in Figure 6 and a photograph of the compact range is shown in Figure 7.[1] By utillizing the compact antenna range in a monostatic radar operation, far field backscattered radar signatures of small targets can be obtained.

The SA parabolic reflector enables the facility to illuminate a 4 foot by 4

---

[1] 1984 aircraft measurement configuration. The range has been significantly improved in recent years.

7

foot target zone with a columnmated plane wave, simulating the far field condition (i.e., locally plane wave effect) of most real operational radar systems. The source, a highly accurate digitally controlled frequency synthesizer, is operated in a continous wave mode and feeds both the transmitting antenna and the reference channel of the SA 1780 receiver. The monostatic measurement is obtained by placing both transmitting and receiving antennas at the focus of the parabolic reflector. The antennas used in this process were rectangular aperture horn antennas, thus providing high cross polarization rejection. The antennas were placed in different arrangements to obtain radar signatures for three different polarization schemes. The polarization schemes measured are listed below as polarization types:

(HH)   Transmitting Horizontal polarization, Receiving Horizontal polarization.

(VV)   Transmitting Vertical polarization, Receiving Vertical polarization.

(HV)   Transmitting Horizontal polarization, Receiving Vertical polarization.

The polarization types HH, VV are commonly referred to as the co-pol polarizations, and the polarization type HV is referred to as the cross-pol polarization. From these three polarization types an orthogonal scattering matrix can be formed, and from this matrix other polarization states can be mathematically synthesized. Note that by the electromagnetic theorem of reciprocity, the polarization types VH (Transmitting Vertical polarization, Receiving Horizontal polarization) and HV are equal. Finally, the controller implements a frequency scan measurement by stepping the digitally controlled synthesizer, and phase locked receiver, and recording both the amplitude and phase of the backscattered signal.

8
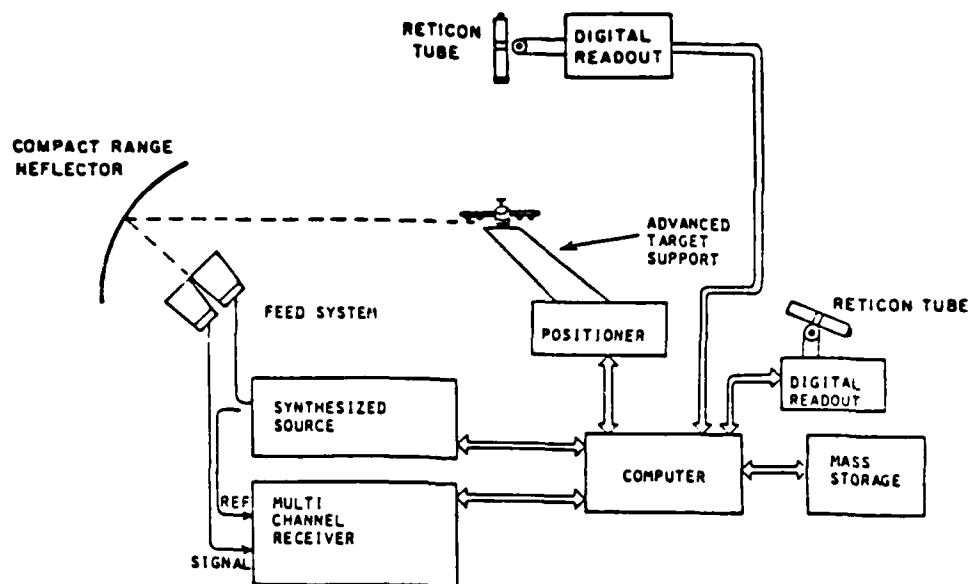
Figure 6: Compact Range Block Diagram
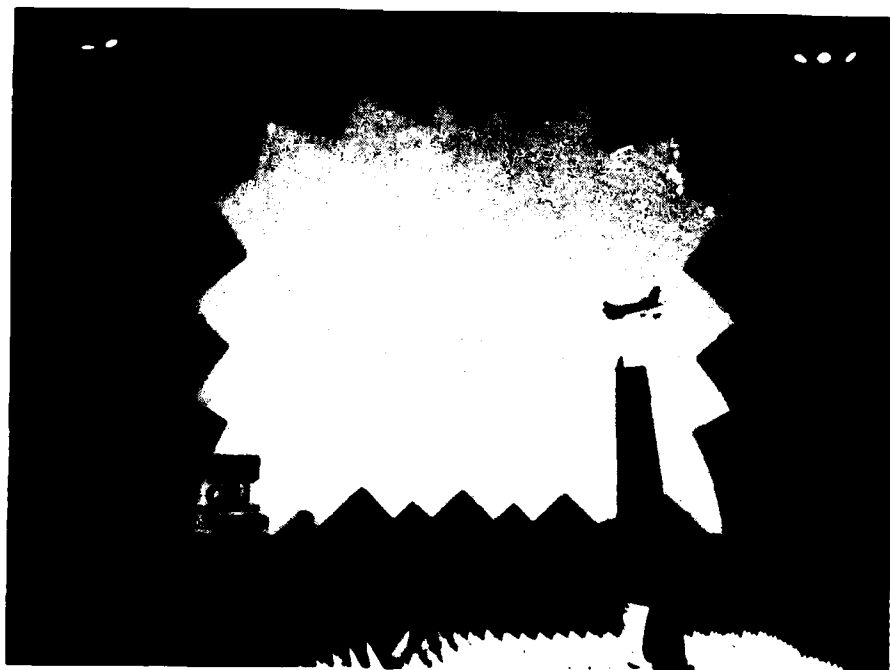
Figure 7: OSU ESL Compact Range with Aircraft Target

2.3   Low-Error Backscattered Target Signatures

To obtain the "low-error" signature, additional steps are required other than those described in the preceding section. These additional steps, as described in detail by Kimball [19], require a calibration sequence designed to remove unwanted background clutter from the target measurement and provide a scale correction factor based on a mathematical representation of a reference target. This process entails a measurement of the background environment (i.e., measurment of the chamber without the target present), and a measurement of a reference target such as a sphere for a co-pol measurement or a 45° tilted strip for a cross-pol measurment.

2.3.1   Calibration Equation

To remove the background clutter and to scale the data to its correct backscattered value, the following calibration equation is used:

$$\tilde{T}_C = \frac{\tilde{E}\left(\tilde{T} - \tilde{B}\right)}{\left(\tilde{R} - \tilde{B}\right)} \tag{2.1}$$

where :

$\tilde{T}_C$ is the calibrated complex backscattered target signal voltage.

$\tilde{E}$ is the computed (exact) complex backscattered signal voltage

from a reference calibration target (i.e., sphere for co-pol,

45° strip for cross-pol measurments).

$\tilde{T}$ is the measured complex backscattered signal voltage with

the target installed in the test chamber.

$\tilde{B}$ is the measured complex backscattered signal voltage with

no target present in the test chamber.

10

$\tilde{R}$ is the measured complex backscattered signal voltage with

   a reference target installed in the test chamber (i.e., sphere

   for co-pol, 45° strip for cross-pol).

To ensure the best results in the calibration process, background and reference target measurements are made after every five target measurements. Additional signal processing techniques are also employed to achieve the final form of the low-error target backscattered signature. For example, digital filtering is applied by the convolution of a Hanning window with the calibrated target data string, $\tilde{T}_C$, which results in an equivalent time domain gating of the target region. By selecting the proper parameters, a further suppression of background clutter is produced without affecting the target signature.

Finally a computer program called DATABASE [20] allows the storage of frequency formatted data strings at many different aspects angles and the three base line polarization types HH, VV, and VH, into one single random-accessed data file. The data base program also joins calibrated target data strings measured in subsectional frequency bands, and reformates the calibrated data strings to a standard 50 MHz frequency increment. The Database format allows easy access of calibrated target signatures by specifying the target name (file-name), azimuth angle, and polarization type in a Fortran call statement. The data bases were created for the purpose of RTI computer simulation and consists of two sets: a low-frequency data base set, and a high-frequency data base set. The low-frequency data base set consists mostly of continuous calibrated unscaled data strings from 1 to 12 GHz. The high-frequency data base set consists of unscaled data strings from 18 to 35 GHz. Listings from the DATABASE computer program characterizing the RTI aircraft data bases are shown in Figures 8 through 13.

11

The Ohio State Univesity ElectroScience Laboratory
Compact Range Experimental Data 1984
Scale factor -   Elevation angle - 0 degrees

LOW FREQUENCY FORMATTED DATA BASE (GHz)

ASPECT (Deg)	" HH "	POLARIZATION " HV "	" VV "
0	1-12	1-12	1-12
10	1-12	1-12	1-12
15	1-12	NULL	1-12
20	1-12	1-12	1-12
25	6-12	NULL	6-12
30	1-12	1-12	1-12
35	6-12	NULL	6-12
40	1-12	1-12	1-12
45	1-12	1-12	1-12
50	1-12	1-12	1-12
55	6-12	NULL	6-12
60	1-12	1-12	1-12
65	6-12	NULL	6-12
70	1-12	1-12	1-12
75	1-12	1-12	1-12
80	1-12	1-12	1-12
85	6-12	NULL	6-12
90	1-12	1-12	1-12
95	6-12	NULL	6-12
100	1-12	1-12	1-12
105	1-12	1-12	1-12
110	1-12	1-12	1-12
115	6-12	NULL	6-12
120	1-12	1-12	1-12
125	6-12	NULL	6-12
130	1-12	1-12	1-12
135	1-12	1-12	1-12
140	1-12	1-12	1-12
145	6-12	NULL	6-12
150	1-12	1-12	1-12
155	6-12	NULL	6-12
160	1-12	1-12	1-12
165	1-12	1-12	1-12
170	1-12	1-12	1-12
175	6-12	NULL	6-12
180	1-12	1-12	1-12

Figure 8: Concord Low-Frequency Data Base Map

12

The Ohio State Univesity ElectroScience Laboratory
Compact Range Experimental Data 1984
Scale factor =   Elevation angle = 0 degrees

LOW FREQUENCY FORMATTED DATA BASE (GHz)

ASPECT (Deg)		POLARIZATION	
	" HH "	" HV "	" VV "
0	1-12	1-12	1-12
10	1-12	1-12	1-12
15	1-12	1-12	1-12
20	1-12	1-12	1-12
30	1-12	1-12	1-12
40	1-12	1-12	1-12
45	1-12	1-12	1-12
50	1-12	1-12	1-12
60	1-12	1-12	1-12
70	1-12	1-12	1-12
75	1-12	1-12	1-12
80	1-12	1-12	1-12
90	1-12	1-12	1-12
100	1-12	1-12	1-12
105	1-12	1-12	1-12
110	1-12	1-12	1-12
120	1-12	NULL	1-12
130	1-12	NULL	1-12
135	1-12	NULL	1-12
140	1-12	1-12	1-12
150	1-12	1-12	1-12
160	1-12	1-12	1-12
165	1-12	1-12	1-12
170	1-12	1-12	1-12
180	1-12	1-12	1-12
270	1-12	1-12	1-12

Figure 9: DC10 Low-Frequency Data Base Map

13

The Ohio State Univesity ElectroScience Laboratory
Compact Range Experimental Data 1984
Scale factor =   Elevation angle = 0 degrees

LOW FREQUENCY FORMATTED DATA BASE (GHz)

ASPECT (Deg)	POLARIZATION		
	" HH "	" HV "	" VV "
0	1-12	1-12	1-12
10	1-12	NULL	1-12
15	1-12	1-12	1-12
20	1-12	1-12	1-12
25	6-12	NULL	6-12
30	1-12	1-12	1-6.3
35	6-12	NULL	6-12
40	1-12	1-12	1-12
45	1-12	1-12	1-12
50	1-12	1-12	1-12
55	6-12	NULL	6-12
60	1-12	1-12	1-12
65	6-12	NULL	6-12
70	1-12	1-12	1-12
75	1-12	1-12	1-12
80	1-12	1-12	1-12
85	6-12	NULL	6-12
90	1-12	1-12	1-12
95	6-12	NULL	6-12
100	1-12	1-12	1-12
105	1-12	1-12	1-12
110	1-12	1-12	1-12
115	6-12	NULL	6-12
120	1-12	1-12	1-12
125	6-12	NULL	6-12
130	1-12	1-12	1-12
135	1-12	1-12	1-12
140	1-12	1-12	1-12
145	6-12	NULL	6-12
150	1-12	1-12	1-12
155	6-12	NULL	6-12
160	1-12	1-12	1-12
165	1-12	1-12	1-12
170	1-12	1-12	1-12
175	6-12	NULL	6-12
180	1-12	1-12	1-12
270	6-12	NULL	1-12

Figure 10: 707 Low-Frequency Data Base Map

14

The Ohio State Univesity ElectroScience Laboratory
Compact Range Experimental Data 1984
Scale factor =   Elevation angle = 0 degrees

LOW FREQUENCY FORMATTED DATA BASE (GHz)

ASPECT (Deg)	POLARIZATION		
	" HH "	" HV "	" VV "
0	1-12	1-12	1-12
10	1-12	1-12	1-12
15	1-12	1-12	1-12
20	1-12	1-12	1-12
30	1-12	1-12	1-12
40	1-12	1-12	1-12
45	1-12	1-12	1-12
50	1-12	1-12	1-12
60	1-12	1-12	1-12
70	1-12	1-12	1-12
75	1-12	1-12	1-12
80	1-12	1-12	1-12
90	1-12	1-12	1-12
100	1-12	1-12	1-12
105	1-12	1-12	1-12
110	1-12	1-12	1-12
120	1-12	1-12	1-12
130	1-12	1-12	1-12
135	1-12	1-12	1-12
140	1-12	1-12	1-12
150	1-12	1-12	1-12
160	1-12	1-12	1-12
165	1-12	1-12	1-12
170	1-12	1-12	1-12
180	1-12	1-12	1-12
270	1-12	1-12	1-12

Figure 11: 727 Low-Frequency Data Base Map

15

The Ohio State Univesity ElectroScience Laboratory
Compact Range Experimental Data 1984
Scale factor -   Elevation angle - 0 degrees

LOW FREQUENCY FORMATTED DATA BASE (GHz)

ASPECT (Deg)	" HH "	POLARIZATION " HV "	" VV "
0	1.5-12	1-12	1-12
10	1.5-12	1-12	NULL
15	6-12	1-12	1-12
20	1.5-12	1-12	NULL
25	6-12	NULL	NULL
30	1.5-12	1-12	1-12
35	6-12	NULL	NULL
40	1.5-12	1-12	NULL
45	1.5-12	1-12	1-12
50	1.5-12	1-12	NULL
55	6-12	NULL	NULL
60	1.5-12	1-12	1-12
65	6-12	NULL	NULL
70	1.5-12	1-12	NULL
75	6-12	1-12	1-12
80	1.5-12	1-12	NULL
90	1.5-12	1-12	1-12
95	6-12	NULL	NULL
100	1.5-12	1-12	NULL
105	6-12	1-12	1-12
110	1.5-12	1-12	NULL
115	6-12	NULL	NULL
120	1.5-12	1-12	1-12
125	6-12	NULL	NULL
130	1.5-12	1-12	NULL
135	6-12	1-12	1-12
140	1.5-12	1-12	NULL
145	6-12	NULL	NULL
150	1.5-12	1-12	1-12
155	6-12	NULL	NULL
160	1.5-12	1-12	NULL
165	6-12	1-12	1-12
170	1.5-12	1-12	NULL
180	1.5-12	1-12	1-12

Figure 12: 747 Low-Frequency Data Base Map

16

```
All Aircraft

The Ohio State Univesity ElectroScience Laboratory
Compact Range Experimental Data 1984
Elevation angle - 0 degrees


HIGH FREQUENCY FORMATTED DATA BASE (GHz)

ASPECT (Deg)                  POLARIZATION
                 " HH "          " HV "          " VV "

     0           18-35           NULL           18-35
    15           18-35           NULL           18-35
    30           18-35           NULL           18-35
    45           18-35           NULL           18-35
```

Figure 13: High-Frequency Data Base Map

2.4 Data Scaling

In order to obtain data in the resonance region of the commercial aircraft used in the simulation study, the interrogation frequencies lie in the HF band. Since the measurement of low-error backscatted radar signatures of such large bodies in this frequency range would require facilities that do not exist, the common practice of data scaling was utilized. Using the scaling properties of electromagnetic waves, model aircraft coated with conducting paint can be used to represent the full-scale aircraft. As long as the wavelength is on the order of the model size, i.e., resonance region, the scale model provides a very close representation of the true full-scale backscattered signature. When scaling methods are employed, care must be taken to make sure the model adequately represents the features of interest. For example, when the wavelength becomes very small compared to the overall aircraft size, smaller features on the aircraft start to resonate and scatter such as engine inlets, cockpit cavities, and other fine grain variation on the aircraft. If these features are

17

not carefully represented on the scale models, the scale model no longer provides an accurate representation of the true backscattered signature. For near resonance region (i.e., where the wavelength is almost as large as the aircraft's largest dimension) the model can be a rough representation of the target, and still provide good measurements of the true backscattered radar signature. The model sizes used for the measurements ranged from scale factors of 1:130 to 1:200. A photo of the models used in the measurement process is shown in Figure 14.

The scaling process is defined by multiplying the amplitude and dividing the frequency by the model's scale factor (SF). The phase measurement is unaffected by the scaling process.

That is:

$$F_s = f_u \, / \, SF \tag{2.2}$$

$$A(F_s) = a(f_u) * SF \tag{2.3}$$

$$\Theta(F_s) = \theta(f_u) \tag{2.4}$$

where the entries on the left side of the equality represent the full-scaled quantities of frequency (F_s), amplitude (A), and phase (Θ). And the entries on the right side of the equality represent the unscaled measured model quantities of frequency (f_u), amplitude (a), and phase (θ).

The unscaled aircraft measured data, ranges between 1 and 12 GHz for the low-frequency data base and 18 to 36 GHz for the high-frequency data base. Appling the scaling relationship for frequency, the resulting net usable common bandwidths for both low and high-frequency data base are: 7.7 to 60 MHz (Low-Frequency Database) and 138.5 to 175 MHz (High-Frequency Database).

18

Figure 15 illustrates the three electromagnetic regions; Rayliegh, resonance, and optical, and where the two scaled frequency bands are categorized. The figure shows that all the available data is not quite categorized as resonance region data. Most of the low-frequency data base is categorized as near-resonance, and the high frequency data base lies in the optical region.

Since the data base contains unscaled data, the frequency selection and scaling routines are implemented in the computer simulation program. Frequency samples from one to the maximum number of frequency samples shown in Table 1 are available to choose from. Since frequency samples can be chosen that are not represented by scaled data points; an interpolation algorithm using a Hamming window weighting routine is implemented to create the desired frequency sample. The interpolation window is 100 MHz wide (unscaled) and centered at the desired frequency sample. After the sample frequency is calculated, it is then scaled to the format of decibel relative to one square meter (dBm^2). The equations for the frequency interpolation are described in detail in [21]. In Figures 16 through 18, some sample data plots are shown illustrating the calibration processes described in the preceding sections.

Table 1: Specifications of Data Bases

Low-Frequency Data Base

Frequency formatted data strings from 1 to 12 GHz

Availible polarizations:

Transmit Horizontal, Receive Horizontal (HH)

Transmit Vertical, Receive Vertical (VV)

Transmit Horizontal, Receive Vertical (VH)

Availible Azimuth angles @ Elevation $= 0°$:

$0°$ to $180°$ by $10°$ and $15°$ increments

Common aircraft bandwidth:

7.6 – 60 MHz "Scaled"

Maximum number of usable frequencies: 209

High-Frequency Data Base

Frequency formatted data strings from 18 to 35 GHz

Availible polarizations:

Transmit Horizontal, Receive Horizontal (HH)

Transmit Vertical, Receive Vertical (VV)

Availible Azimuth angles @ Elevation $= 0°$:

$0°$, $15°$, $30°$, $45°$ only

Common aircraft bandwidth:

139 – 175 MHz "Scaled"

Maximum number of usable frequencies: 146

Figure 14: Group Photo of Model Aircraft

TARGET CLASSIFICATION
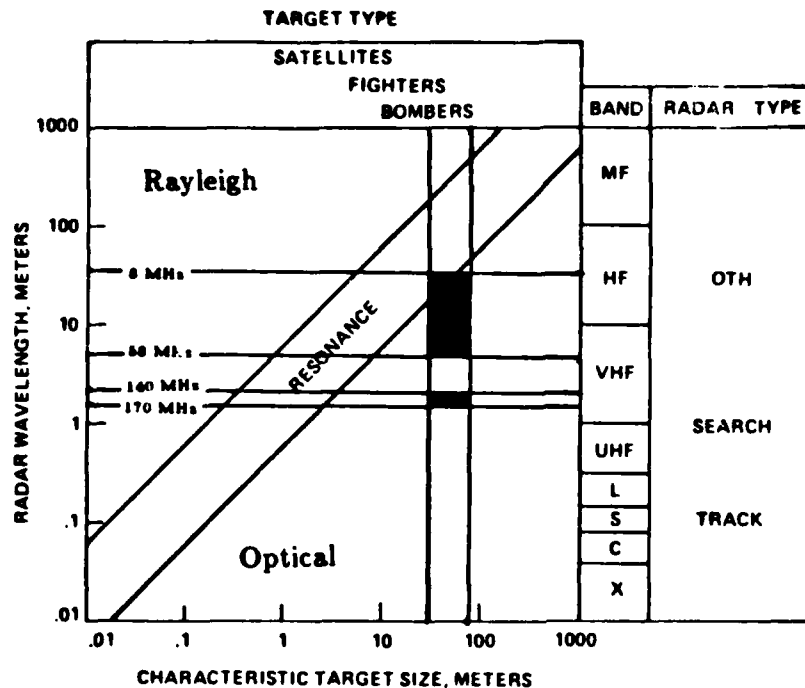
Rayleigh Region: Scattered fields are descripted of the Volume of the target.

Resonance Region: Scattered fields are descripted of the Surface Currents

that are in both the Lit and Shadow regions.

Optical Region: Scattered fields are descripted of the Principal

Curvatures of the Specular Points.

Figure 15: Electromagnetic Regions: Rayliegh, Resonance, and Optical

22
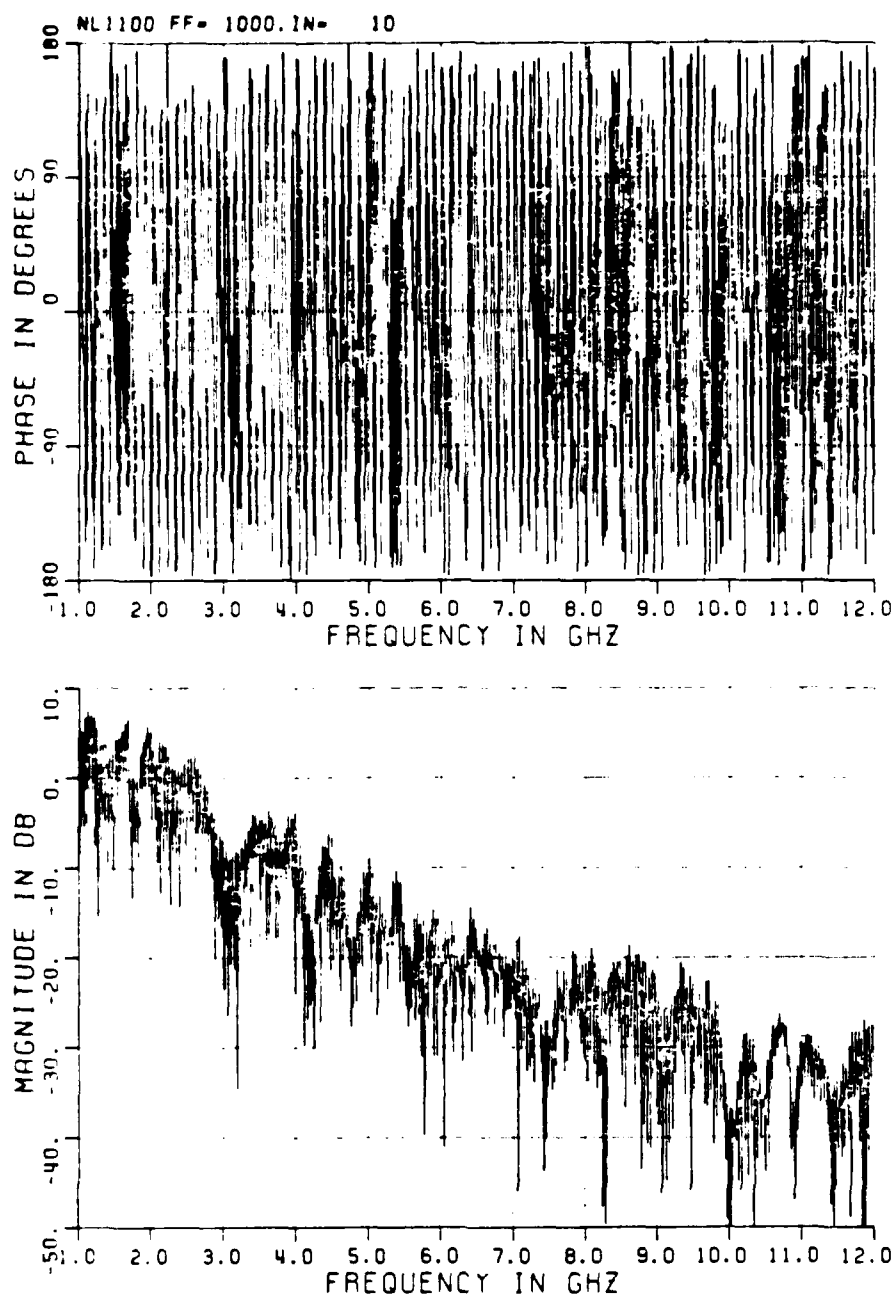
Figure 16: Raw Uncalibrated MonoStatic Radar Data

23
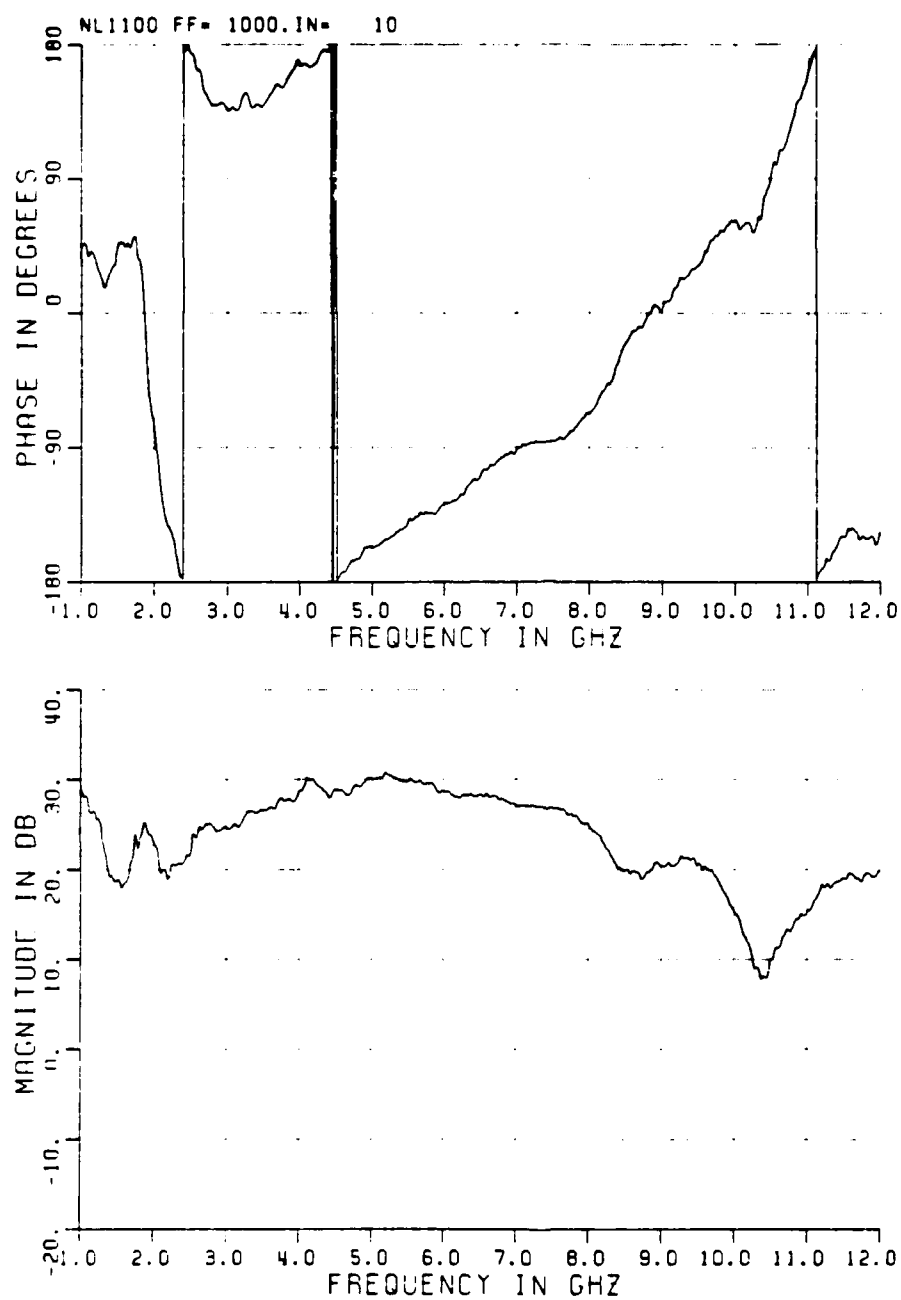
Figure 17: Calibrated MonoStatic Radar Data (10 MHz frequency increment)

24

NL 221 FF= 1000 IN= 50 AA = 90 POL = HH LINEAR
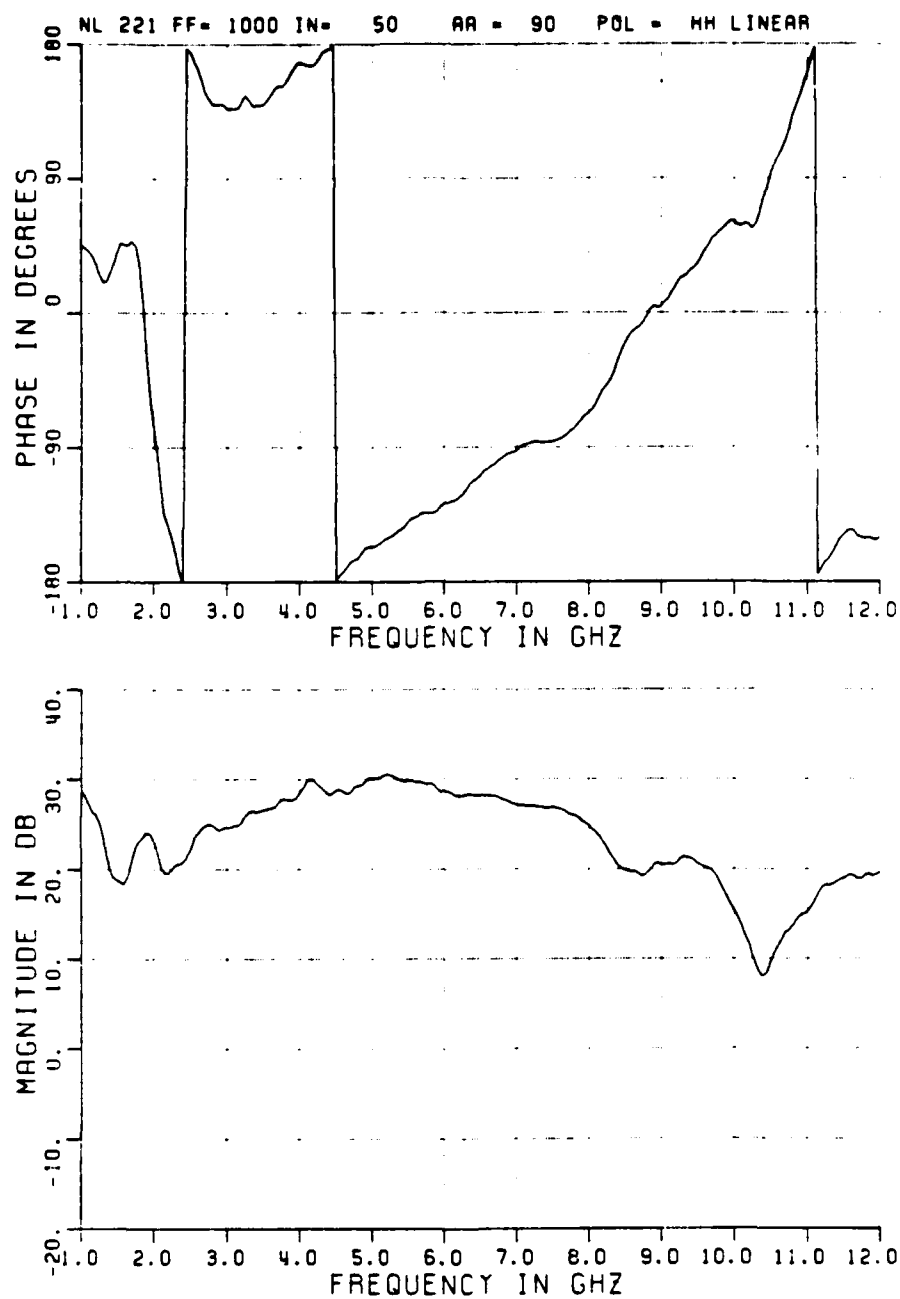
Figure 18: Database Formatted Radar Data (50 MHz frequency increment)

CHAPTER III

TARGET CLASSIFICATION TECHNIQUES

3.1   Introduction

The basic process of target classification is shown in Figure 19. The process defines a measurement system that gathers information on a target, and passes the information to a feature extractor. The feature extractor selects feature vectors (vectors derived from the information), and passes the feature vectors to the classifier. Finally the classifier, using "known" feature vectors to identify the extracted feature vectors, classifies the target.

For the Radar Target Identification problem of classifying aircraft the measurement system may consists of a low-frequency radar that provides initial search and resonance frequency data (which has been shown to provide good feature vectors for target identification [1,13]), and a high-frequency high-resolution radar to provide accurate information on bearing, speed, and range. The feature extractor may extract all or part of the information obtained by the measurement system. For example, the low-frequency measurement may be processed by the feature extractor to remove background clutter, doppler shift, and path length phase shift, to become the measured noisy "unknown target" feature vector. The classifier, using a predetermined identification algorithm, then compares the noisy feature vector to the selected catalog of low-error "known target" feature vectors for target identification. The target would be identified as a known member of the selected
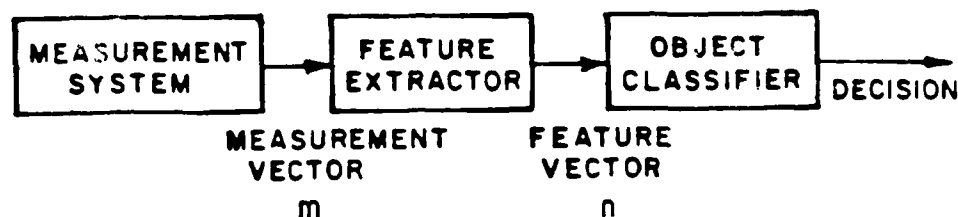
Figure 19: Basic Process of Target Classification

catalog, or a target belonging to some uncatalogued aircraft. Additionally, the data from the high-frequency radar may be used to tell the classifier to select a subsector of the feature vectors from the known target low-error data base. For example, a subsector might contain only feature vectors that have speeds at or faster than the target speed measured and aspect angles in the range of the bearing angle measured. The problem of determining whether an observed target is not a member of a selected set of target feature vectors has been discussed in [12] and will not be presented in this material.

3.2 Target Feature Extractor

The results presented in this document are from a simulation program called the OSU Radar System Simulation and Evaluation (RSSE) computer program [20]. This computer program was developed to implement the various processes described above. The RSSE computer program simulates the measurement systems of six different "polarization-oriented" monostatic radars. The RSSE feature extractor processes the six radars types to derive the various feature vectors used by the classifier for the RTI process. The six simulated monostatic radars are:

27

- LINEAR POLARIZED RADARS

1) Transmitting Horizontal, Receiving Horizontal   (HH)

2) Transmitting Vertical, Receiving Vertical   (VV)

3) Transmitting Horizontal, Receiving Vertical   (HV)

- CIRCULAR POLARIZED RADARS

4) Transmitting Right Circular, Receiving Right Circular   (RR)

5) Transmitting Left Circular, Receiving Left Circular   (LL)

6) Transmitting Right Circular, Receiving Left Circular   (RL)

The simulated radars provide the dominant far-field complex backscattered coefficients: $\tilde{\sigma}_{HH}^{BS}$, $\tilde{\sigma}_{VV}^{BS}$, $\tilde{\sigma}_{VH}^{BS}$, $\tilde{\sigma}_{RR}^{BS}$, $\tilde{\sigma}_{LL}^{BS}$, and $\tilde{\sigma}_{RL}^{BS}$.[1] Where the complex backscattered coefficient $\tilde{\sigma}$ is related to the Radar Cross Section (RCS) coefficient, σ, and its associated phase, φ, as follows:

$$\tilde{\sigma} = \sigma \epsilon^{2j\varphi} \qquad (3.1)$$

The three linearly polarized complex RCS coefficients $\tilde{\sigma}_{HH}$, $\tilde{\sigma}_{VV}$, and $\tilde{\sigma}_{VH}$, are quantities measured on the OSU compact range (see section 2.2). The other three backscattered coefficients (i.e., the circular polarized backscattered coefficients $\tilde{\sigma}_{RR}$, $\tilde{\sigma}_{LL}$, and $\tilde{\sigma}_{RL}$) were synthesized by using the three linearly polarized backscattered coefficients in the following polarization transformations:

$$\sqrt{\tilde{\sigma}_{LL}} = \sqrt{4\pi}\frac{\bar{E}_r}{\bar{E}_t} = \frac{1}{2}\left[\sqrt{\tilde{\sigma}_{VV}} - \sqrt{\tilde{\sigma}_{HH}}\right] - j\sqrt{\tilde{\sigma}_{VH}} \qquad (3.2)$$

[1]All subsequent backscattered coefficients, $\tilde{\sigma}^{BS}$, will suppresses the superscript ^{BS} for ease of notation.

28

$$\sqrt{\tilde{\sigma}_{RR}} = \frac{1}{2}\left[\sqrt{\tilde{\sigma}_{HH}} - \sqrt{\tilde{\sigma}_{VV}}\right] - j\sqrt{\tilde{\sigma}_{VH}} \tag{3.3}$$

$$\sqrt{\tilde{\sigma}_{LR}} = \sqrt{\tilde{\sigma}_{RL}} = \frac{-j}{2}\left[\sqrt{\tilde{\sigma}_{VV}} + \sqrt{\tilde{\sigma}_{HH}}\right] \tag{3.4}$$

Note that the quantity, $\sqrt{\tilde{\sigma}}$, provides a range independent feature for RTI applications. The derivation of the above polarization transformations can be found in Appendix A.

3.3 Feature Vectors

The feature vectors created by the feature extractor are represented by various linear and non-linear combinations of the six backscattered coefficients. The feature vectors are grouped into two categories: linear polarization radar feature vectors and circular polarization radar feature vectors. The feature vectors, usually comprised of multi-frequency data samples, are shown in Tables 2 through 6 for both the linear and circular polarized categories. These tables show the various combinations of the backscattered coefficients in the multi-frequency sample format. The backscattered coefficient has been changed to a voltage quantity by taking the principle root of the complex coefficient. The various feature vectors listed in the tables have properties uniquely associated with them. For instance, the circular polarization category of feature vectors tend to be less sensitive to changes in the roll angle of symmetric bodies. For aircraft, especially in the nose-on and tail-on aspect angles, a change in roll angle will change the vertical and horizontal scattering components in both amplitude and phase while the circular scattering components only undergo a change in phase. The ratio type feature vectors have the added advantage of a cancellation of multiplicative errors by the division of scattering component. This cancellation property may lead to better

29

error statistics in actual practice over the non-ratio type feature vectors. A ratio type feature vector also eliminates the need of a reference for exact calibration of the backscattered coefficients, since the division process makes the feature vector a relative quantity instead of an exact quantity. Finally the polarization diverse feature vector (i.e., the concatenation feature vector type) has the property of creating a large feature space with very few frequency samples.

3.4 Classification Algorithms

Listings of a feature vector for many targets under various observations constitute a feature space. In the simulation study, a subset of the feature space of low noise feature vectors linked to known target identities is defined as the catalog set. A set of feature vectors with unknown "noisy" target identities is referred to as the test set. The classifier function is to take the feature vectors in the test set and match them with feature vectors in the catalog set through the appropriate use of a classification algorithm. The classification algorithms studied in this report consist of two non-parametric methods (i.e., no *a priori* probabilistic information) of target identification, one a Euclidean distance-metric, and the other a cross-correlation routine.

3.4.1 Euclidean Distance Metric Algorithm

The euclidean distance metric coefficient is define by the following equation:

$$d_{ij} = \sqrt{\sum_{n=1}^{N} \left| \mathcal{FV}_i(n) - FV_j(n) \right|^2} \qquad (3.5)$$

where $\mathcal{FV}_i(n)$ and $FV_j(n)$ are feature vectors containing N elements. The identity of the unknown i^{th} noisy test target feature vector $\mathcal{FV}_i$ is chosen by choosing the smallest d_{ij} and classifying the ith unknown test target as the jth catalog target.

30

This method of classifying objects from a set of unknown samples is often reffered to as the Nearest Neighbor (NN) decision rule. Since equation (3.5) utilizes feature vectors containing both amplitude and phase information, it is referred to as the coherent NN algorithm.

The coherent distance metric presented above is used to analyze data with precise phase information obtained by a precise knowledge of range to a chosen phase reference. This algorithm can be used to analyze data with other types of phase data, such as relative phase between frequency samples, and will be discussed in the final chapter of this report. For a detailed discussion of methods to obtain radar phase measurements, the reader is reffered to [22]. For an amplitude-only radar simulation, a non-coherent NN algorithm is used in place of the coherent one. The non-coherent distance metric simply uses the magnitude of the elements of the feature vectors and is written as:

$$d_{ij} = \sqrt{\sum_{n=1}^{N} \left(|\mathcal{F}\mathcal{V}_i(n)| - \left| FV_j(n) \right| \right)^2} \tag{3.6}$$

3.4.2 Time Domain Cross Correlation (TDCC) Algorithm

Utilizing the multi-frequency nature of the simulated radar target interrogation and the discrete time frequency relationships, a synthesized discrete time representation of the feature vectors can be obtained through the use of the Inverse Discrete Fourier Transform (IDFT). For the six baseline polarization feature vectors (i.e., FV^{HH}, FV^{VV}, FV^{VH}, FV^{RR}, FV^{LL}, and FV^{RL}) the time domain representation provides a method of classification (i.e., cross correlation) that is independent of time shifts in the time domain or common phase reference in the frequency domain. This independence of a common phase reference between the

31

test and catalog targets is a desirable feature but the cost or penalty is the processing time required by the IDFT.

For feature vectors utilizing non-linear combinations of the six baseline polarizations (ex. $\frac{FV^{HH}}{FV^{VV}}$, $\frac{FV^{VV}}{FV^{HH}}$, $\frac{FV^{RR}}{FV^{LL}}$, ect ...), TDCC no longer represents a correlation between linear time shifted test and catalog radar signatures. Although the time domain cross correlation is still a valid procedure, the loss of the linear time shift property leads us to use the more robust coherent NN algorithm for the examination of the non-linear combinational feature vector types.

The normalized cross-corralation coefficient is written as:

$$c_{ij}(k) = \frac{DIFT\left(\mathcal{F}\mathcal{V}_i \, FV_j^*\right)}{\sqrt{\sum_{n=1}^{N} |\mathcal{F}\mathcal{V}_i(n)|^2} \sqrt{\sum_{n=1}^{N} \left|FV_j(n)\right|^2}} \tag{3.7}$$

where $*$ denotes complex conjugation. The identification decision rule is to choose the largest $c_{ij}(k)$, thus classifying the ith unknown test target as the jth known catalog target. Although the TDCC method works with as few as 2 frequency samples [23], a small number of frequency samples leads to poor resolution and poor classification results (see Section 5.4).

The equations for both the NN and TDCC algorithms described above are thoroughly presented and derived in [15].

32

Table 2: Linear Polarized Feature Vectors Types

Transmit *Horizontal*, Receive *Horizontal* feature vector:

$$FV^{HH} = \left(\sqrt{\tilde{\sigma}_{HH}(f_1)}, \sqrt{\tilde{\sigma}_{HH}(f_2)}, \cdots, \sqrt{\tilde{\sigma}_{HH}(f_N)} \right)$$

Transmit *Vertical*, Receive *Vertical* feature vector:

$$FV^{VV} = \left(\sqrt{\tilde{\sigma}_{VV}(f_1)}, \sqrt{\tilde{\sigma}_{VV}(f_2)}, \cdots, \sqrt{\tilde{\sigma}_{VV}(f_N)} \right)$$

Transmit *Vertical*, Receive *Horizontal* feature vector:

$$FV^{VH} = \left(\sqrt{\tilde{\sigma}_{VH}(f_1)}, \sqrt{\tilde{\sigma}_{VH}(f_2)}, \cdots, \sqrt{\tilde{\sigma}_{VH}(f_N)} \right)$$

Linear Polarization Diverse *Concatenation* feature vector:

$$FV^{CAT} = \left(\sqrt{\tilde{\sigma}_{HH}(f_1)}, \sqrt{\tilde{\sigma}_{VV}(f_1)}, \sqrt{\tilde{\sigma}_{VH}(f_1)}, \sqrt{\tilde{\sigma}_{HH}(f_2)}, \sqrt{\tilde{\sigma}_{VV}(f_2)}, \sqrt{\tilde{\sigma}_{VH}(f_2)}, \cdots, \right.$$
$$\left. \sqrt{\tilde{\sigma}_{HH}(f_N)}, \sqrt{\tilde{\sigma}_{VV}(f_N)}, \sqrt{\tilde{\sigma}_{VH}(f_N)} \right)$$

Linear Polarization Diverse *Complex Sum* feature vector:

$$FV^{CS} = \left(\sqrt{\tilde{\sigma}_{HH}(f_1)} + \sqrt{\tilde{\sigma}_{VV}(f_1)} + \sqrt{\tilde{\sigma}_{VH}(f_1)}, \sqrt{\tilde{\sigma}_{HH}(f_2)} + \sqrt{\tilde{\sigma}_{VV}(f_2)} + \sqrt{\tilde{\sigma}_{VH}(f_2)}, \cdots, \right.$$
$$\left. \sqrt{\tilde{\sigma}_{HH}(f_N)} + \sqrt{\tilde{\sigma}_{VV}(f_N)} + \sqrt{\tilde{\sigma}_{VH}(f_N)} \right)$$

33

Table 3: Circular Polarized Feature Vectors Types

Transmit *Left Circular* , Receive *Left Circular* feature vector:

$$FV^{LL} = \left(\sqrt{\tilde{\sigma}_{LL}(f_1)}, \sqrt{\tilde{\sigma}_{LL}(f_2)}, \cdots, \sqrt{\tilde{\sigma}_{LL}(f_N)} \right)$$

Transmit *Right Circular* , Receive *Right Circular* feature vector:

$$FV^{RR} = \left(\sqrt{\tilde{\sigma}_{RR}(f_1)}, \sqrt{\tilde{\sigma}_{RR}(f_2)}, \cdots, \sqrt{\tilde{\sigma}_{RR}(f_N)} \right)$$

Transmit *Right Circular* , Receive *Left Circular* feature vector:

$$FV^{RL} = \left(\sqrt{\tilde{\sigma}_{RL}(f_1)}, \sqrt{\tilde{\sigma}_{RL}(f_2)}, \cdots, \sqrt{\tilde{\sigma}_{RL}(f_N)} \right)$$

Circular Polarization Diverse *Concatenation* feature vector:

$$FV^{CAT} = \left(\sqrt{\tilde{\sigma}_{LL}(f_1)}, \sqrt{\tilde{\sigma}_{RR}(f_1)}, \sqrt{\tilde{\sigma}_{RL}(f_1)}, \ \sqrt{\tilde{\sigma}_{LL}(f_2)}, \sqrt{\tilde{\sigma}_{RR}(f_2)}, \sqrt{\tilde{\sigma}_{RL}(f_2)}, \cdots, \right.$$
$$\left. \sqrt{\tilde{\sigma}_{LL}(f_N)}, \sqrt{\tilde{\sigma}_{RR}(f_N)}, \sqrt{\tilde{\sigma}_{RL}(f_N)} \right)$$

Circular Polarization Diverse *Complex Sum* feature vector:

$$FV^{CS} = \left(\sqrt{\tilde{\sigma}_{LL}(f_1)} + \sqrt{\tilde{\sigma}_{RR}(f_1)} + \sqrt{\tilde{\sigma}_{RL}(f_1)}, \ \sqrt{\tilde{\sigma}_{LL}(f_2)} + \sqrt{\tilde{\sigma}_{RR}(f_2)} + \sqrt{\tilde{\sigma}_{RL}(f_2)}, \cdots, \right.$$
$$\left. \sqrt{\tilde{\sigma}_{LL}(f_N)} + \sqrt{\tilde{\sigma}_{RR}(f_N)} + \sqrt{\tilde{\sigma}_{RL}(f_N)} \right)$$

34

Table 4: Linear Polarization *RATIO* Feature Vectors Types

$$FV\,_{VV}^{HH} = \left(\frac{\sqrt{\tilde{\sigma}_{HH}(f_1)}}{\sqrt{\tilde{\sigma}_{VV}(f_1)}}, \frac{\sqrt{\tilde{\sigma}_{HH}(f_2)}}{\sqrt{\tilde{\sigma}_{VV}(f_2)}}, \ldots, \frac{\sqrt{\tilde{\sigma}_{HH}(f_N)}}{\sqrt{\tilde{\sigma}_{VV}(f_N)}} \right)$$

$$FV\,_{VH}^{HH} = \left(\frac{\sqrt{\tilde{\sigma}_{HH}(f_1)}}{\sqrt{\tilde{\sigma}_{VH}(f_1)}}, \frac{\sqrt{\tilde{\sigma}_{HH}(f_2)}}{\sqrt{\tilde{\sigma}_{VH}(f_2)}}, \ldots, \frac{\sqrt{\tilde{\sigma}_{HH}(f_N)}}{\sqrt{\tilde{\sigma}_{VH}(f_N)}} \right)$$

$$FV\,_{HH}^{VV} = \left(\frac{\sqrt{\tilde{\sigma}_{VV}(f_1)}}{\sqrt{\tilde{\sigma}_{HH}(f_1)}}, \frac{\sqrt{\tilde{\sigma}_{VV}(f_2)}}{\sqrt{\tilde{\sigma}_{HH}(f_2)}}, \ldots, \frac{\sqrt{\tilde{\sigma}_{VV}(f_N)}}{\sqrt{\tilde{\sigma}_{HH}(f_N)}} \right)$$

$$FV\,_{VH}^{VV} = \left(\frac{\sqrt{\tilde{\sigma}_{VV}(f_1)}}{\sqrt{\tilde{\sigma}_{VH}(f_1)}}, \frac{\sqrt{\tilde{\sigma}_{VV}(f_2)}}{\sqrt{\tilde{\sigma}_{VH}(f_2)}}, \ldots, \frac{\sqrt{\tilde{\sigma}_{VV}(f_N)}}{\sqrt{\tilde{\sigma}_{VH}(f_N)}} \right)$$

$$FV\,_{HH}^{VH} = \left(\frac{\sqrt{\tilde{\sigma}_{VH}(f_1)}}{\sqrt{\tilde{\sigma}_{HH}(f_1)}}, \frac{\sqrt{\tilde{\sigma}_{VH}(f_2)}}{\sqrt{\tilde{\sigma}_{HH}(f_2)}}, \ldots, \frac{\sqrt{\tilde{\sigma}_{VH}(f_N)}}{\sqrt{\tilde{\sigma}_{HH}(f_N)}} \right)$$

$$FV\,_{VV}^{VH} = \left(\frac{\sqrt{\tilde{\sigma}_{VH}(f_1)}}{\sqrt{\tilde{\sigma}_{VV}(f_1)}}, \frac{\sqrt{\tilde{\sigma}_{VH}(f_2)}}{\sqrt{\tilde{\sigma}_{VV}(f_2)}}, \ldots, \frac{\sqrt{\tilde{\sigma}_{VH}(f_N)}}{\sqrt{\tilde{\sigma}_{VV}(f_N)}} \right)$$

Table 5: Circular Polarization *RATIO* Feature Vectors Types

$$FV\frac{LL}{RR} = \left(\frac{\sqrt{\tilde{\sigma}_{LL}(f_1)}}{\sqrt{\tilde{\sigma}_{RR}(f_1)}}, \frac{\sqrt{\tilde{\sigma}_{LL}(f_2)}}{\sqrt{\tilde{\sigma}_{RR}(f_2)}}, \ldots, \frac{\sqrt{\tilde{\sigma}_{LL}(f_N)}}{\sqrt{\tilde{\sigma}_{RR}(f_N)}} \right)$$

$$FV\frac{LL}{RL} = \left(\frac{\sqrt{\tilde{\sigma}_{LL}(f_1)}}{\sqrt{\tilde{\sigma}_{RL}(f_1)}}, \frac{\sqrt{\tilde{\sigma}_{LL}(f_2)}}{\sqrt{\tilde{\sigma}_{RL}(f_2)}}, \ldots, \frac{\sqrt{\tilde{\sigma}_{LL}(f_N)}}{\sqrt{\tilde{\sigma}_{RL}(f_N)}} \right)$$

$$FV\frac{RR}{LL} = \left(\frac{\sqrt{\tilde{\sigma}_{RR}(f_1)}}{\sqrt{\tilde{\sigma}_{LL}(f_1)}}, \frac{\sqrt{\tilde{\sigma}_{RR}(f_2)}}{\sqrt{\tilde{\sigma}_{LL}(f_2)}}, \ldots, \frac{\sqrt{\tilde{\sigma}_{RR}(f_N)}}{\sqrt{\tilde{\sigma}_{LL}(f_N)}} \right)$$

$$FV\frac{RR}{RL} = \left(\frac{\sqrt{\tilde{\sigma}_{RR}(f_1)}}{\sqrt{\tilde{\sigma}_{RL}(f_1)}}, \frac{\sqrt{\tilde{\sigma}_{RR}(f_2)}}{\sqrt{\tilde{\sigma}_{RL}(f_2)}}, \ldots, \frac{\sqrt{\tilde{\sigma}_{RR}(f_N)}}{\sqrt{\tilde{\sigma}_{RL}(f_N)}} \right)$$

$$FV\frac{RL}{LL} = \left(\frac{\sqrt{\tilde{\sigma}_{RL}(f_1)}}{\sqrt{\tilde{\sigma}_{LL}(f_1)}}, \frac{\sqrt{\tilde{\sigma}_{RL}(f_2)}}{\sqrt{\tilde{\sigma}_{LL}(f_2)}}, \ldots, \frac{\sqrt{\tilde{\sigma}_{RL}(f_N)}}{\sqrt{\tilde{\sigma}_{LL}(f_N)}} \right)$$

$$FV\frac{RL}{RR} = \left(\frac{\sqrt{\tilde{\sigma}_{RL}(f_1)}}{\sqrt{\tilde{\sigma}_{RR}(f_1)}}, \frac{\sqrt{\tilde{\sigma}_{RL}(f_2)}}{\sqrt{\tilde{\sigma}_{RR}(f_2)}}, \ldots, \frac{\sqrt{\tilde{\sigma}_{RL}(f_N)}}{\sqrt{\tilde{\sigma}_{RR}(f_N)}} \right)$$

Table 6: *Axial Ratio* (AR) Feature Vectors Types

Transmitting *Right Circular* Polarization

$$RAR = \frac{|\sqrt{\tilde{\sigma}_{RL}}| - |\sqrt{\tilde{\sigma}_{RR}}|}{|\sqrt{\tilde{\sigma}_{RL}}| + |\sqrt{\tilde{\sigma}_{RR}}|}$$

$$FV^{RAR} = (RAR(f_1), RAR(f_2), \cdots, RAR(f_N))$$

Transmitting *Left Circular* Polarization

$$LAR = \frac{|\sqrt{\tilde{\sigma}_{LL}}| - |\sqrt{\tilde{\sigma}_{RL}}|}{|\sqrt{\tilde{\sigma}_{LL}}| + |\sqrt{\tilde{\sigma}_{RL}}|}$$

$$FV^{LAR} = (LAR(f_1), LAR(f_2), \cdots, LAR(f_N))$$

Concatenation of Axial Ratio Types

$$FV^{AR-CAT} = (RAR(f_1), RAR(f_2), \cdots, RAR(f_N), LAR(f_1), LAR(f_2), \cdots, LAR(f_N))$$

CHAPTER IV

EXPERIMENTAL CONSIDERATIONS

4.1 Introduction

In this chapter, the various experimental processes and performance specifications of the RSSE [20] computer program are described. This includes a discussion of: how the noise model injects error into the test targets feature vectors, the calculation of average feature vector signal power, and the statistical technique for estimating the probability of misclassification.

Figure 20 shows a flowchart illustrating the basic processing steps for the target identification code contained in the RSSE computer program. The flow chart begins with accessing the database files that contain the multi-frequency radar signatures at various aspect angles and the three polarization types. $A_j(f_k)$ denotes the amplitude data of the kth frequency sample of the jth target, and $\theta_j(f_k)$ denotes the phase component of the kth frequency sample of the jth target. After the target data bases have been accessed and the scaling routines applied, two data sets of feature vectors are created through linear or non-linear combinations of the linear polarized or synthesized circular polarized backscattered coefficients. The two data sets are called the test and catalog data sets, and the test set feature vectors are corrupted with noise. To create the noisy test set feature vectors, the low-error cross-sectional signatures of the data bases (i.e., the linear and circular polarization components $\sqrt{\tilde{\sigma}_{HH}}$, $\sqrt{\tilde{\sigma}_{VV}}$, $\sqrt{\tilde{\sigma}_{VH}}$, $\sqrt{\tilde{\sigma}_{RR}}$, $\sqrt{\tilde{\sigma}_{LL}}$, and $\sqrt{\tilde{\sigma}_{RL}}$)

38

Data Base

$A_j(f_k) : \theta_j(f_k)$

Scaling

See Section 2.4

$f_o = f_u / SF$

$A(f_o) = A(f_u) \cdot SF$

$\theta(f_o) = \theta(f_u)$

Scaling

See Section 2.4

Calculation of Noise Free Signal Power

$\dfrac{\sum\limits_{k=1}^{K} A_j^2(f_k)}{K}$ (See Tables 7 - 11)

$\sqrt{\sigma_j(f_k)} = A_j(f_k)e^{\theta_j(f_k)}$

$A_j(f_k)e^{\theta_j(f_k)} = I_j(f_k) + jQ_j(f_k)$

Calculation of Noise Free Signal Power

$\dfrac{\sum\limits_{k=1}^{K} A_j^2(f_k)}{K}$ (See Tables 7 - 11)

Insert Noise

$(I + N_p) + j(Q + N_q)$

$k = 1, 2, \ldots, K$ frequencies

$i = 1, 2, \ldots, I$ targets

$j = 1, 2, \ldots, J$ targets

Feature Vector Formation

See Tables 2-6

Feature Vector Formation

See Tables 2-6

Catalog Set

FV_j

Test Set

FV_i

Classification Algorithms

See Section 3.4

Nearest Neighbor

Cross Correlation

$c_{ij}(k) = \dfrac{DIFT\left(FV_i\, FV_j^*\right)}{\sqrt{\sum\limits_{n=1}^{N} |FV_i(n)|^2}\sqrt{\sum\limits_{n=1}^{N} |FV_j(n)|^2}}$

Non Coherent

$d_{ij} = \sqrt{\sum\limits_{n=1}^{N} \left(|FV_i(n)| - |FV_j(n)|\right)^2}$

Coherent

$d_{ij} = \sqrt{\sum\limits_{n=1}^{N} |FV_i(n) - FV_j(n)|^2}$

Decision

Compile Statistics

Figure 20: RSSE Classification Flowchart

39

are corrupted with noise before the combination of components. On the other hand, the catalog set (the low-error feature vector set) is created directly from combinations of the low-error cross-sectional signatures of the databases. Once the test set and catalog set of feature vectors are created, an identification algorithm is chosen. The statistical analysis is obtained by classifying the test set feature vectors several times with the catalog set feature vectors. Also, each experiment in the analysis is statistically independent.

The following sections describe various parts of the Monte-Carlo system simulation techniques, such as the noise model, the calculation of signal power, and the calculation of misclassification statistics. This detailed description serves the reader in interpreting the experimental results of Chapter 5. In the first section, the noise model is described along with the calculation of average signal power contained in a feature vector. From this information the Signal to Noise ratio (S/N) can be determined to serve the reader as a guide for the evaluation of various identification techniques examined. In the second section, the statistical method for estimating the probability of misclassification is presented along with the error margins associated with the estimating technique.

4.2 Noise Model

The operating environment of a radar system contains many different types of errors that can affect the radar target signature. The errors can consist of unwanted atmospheric, cosmic, solar, man-made, and clutter (unwanted radar echoes such as reflections from land, sea, rain, birds, and chaff) noise that can distort the desired radar return (additive noise types). Also, if the system is based on an over the horizon target detection scheme, the radar signal can be distorted through a variety ways, such as: ducting, focusing, differential absorption, Faraday

40

rotation, traveling ionospheric disturbances, and diurnal tilts in the ionosphere (multiplicative noise types).

Although a large part of these noise mechanisms can be calibrated or compensated for in an operational system; errors will appear to some degree of distortion in the final calibrated radar return. As presented above, there are many factors which can affect the noise present in a radar return. Since computer modeling the different noise mechanisms that may occur in a given radar environment is extremly difficult and complex, a simple and direct method of introducing noise into a low-error radar signature is used.

One of the most commonly used methods of simulating a noisy radar environment is by the use of the additive white zero mean Gaussian noise model. The additive white zero mean Gaussian noise model provides uncorrelated statistics between data samples (white), an unbiased corruption of the data samples (zero mean), and a multi-source representation of the noisy environment (Gaussian). These noise properties exist in most real-world operational radar systems. For if any correlated or biased noise statistics are found in the final calibrated radar return, the radar system is inefficient in its calibration routines and the noise level of the system is higher than it should be. In addition, the additive white Gaussian noise model has become a benchmark for the evaluation of the performance of a wide variety of systems. A complete treatment of computer generation of a pseudo-random quantity obeying Gaussian statistics within the limits of current machine accuracy is given in [24].

Implementing the additive white zero mean Gaussian noise model in the simulation process, the backscattered radar signatures are contaminated by adding in-phase and quadrature Gaussian noise components. This process is only applied to the linear and circular backscatter components $\sqrt{\bar{\sigma}_{HH}}$, $\sqrt{\bar{\sigma}_{VV}}$, $\sqrt{\bar{\sigma}_{VH}}$, $\sqrt{\bar{\sigma}_{RR}}$, $\sqrt{\bar{\sigma}_{LL}}$,

41

and $\sqrt{\tilde{\sigma}_{RL}}$, before a feature vector is created. An example of this process can be described as follows:

Suppose the feature vector RR/LL is to be created for the radar target identification simulation. First, the low-error multi-frequency backscatter signatures required to form the feature vector are obtained from the target databases. The signatures are then scaled by the appropriate scale factors and sent to the noise corruption routine. For the RR/LL feature vector, only the low-error synthesized backscattered components RR and LL in complex form would be present at this point. The additive white Gaussian noise is then applied by forming the vector sum: $\mathcal{RR} = RR + N_1$, where N is the complex Gaussian noise vector and $\mathcal{RR}$ is the noise corrupted complex radar return. Additionally, the vector sum: $\mathcal{LL} = LL + N_2$ is needed to form the unknown target noise corrupted feature vector $FV^{\mathcal{RR}/\mathcal{LL}}$. The noise vector N_1 and N_2 are "independent" quantities generated by forming the complex sum:

$$N = N_p + jN_q, \tag{4.1}$$

where $j = \sqrt{-1}$ and N_p and N_q are the independent Gaussian distributed random variables with zero mean and variance σ^2 (computed by methods described in [24]). The N_p and N_q components are the in-phase and quadrature deviates, where the power contained in the in-phase component N_p is equal to that of the quadrature component N_q. The average noise power is then given by :

$$N^2 = N_p^2 + N_q^2 = 2\sigma^2 \tag{4.2}$$

which is twice the variance. The noise phase θ_N, is given by:

$$\theta_N = tan^{-1} \begin{bmatrix} N_q \\ N_p \end{bmatrix} \tag{4.3}$$

42

Throughout the simulation study the noise power, $2\sigma^2$, is specified in units of decibels relative to one square meter (dBm^2). Figure 21 is a representation of the contamination of noise onto a noise free vector. The figure illustrates the Gaussian distribution of both the in-phase and quadrature noise components, thus corrupting the noise free data point to positions insided the shaded circular region. An expression for the signal to noise ratio can now be given as :

$$\frac{S}{N} = \frac{\left(I_s^2 + Q_s^2\right)}{\left(N_p^2 + N_q^2\right)} = \frac{A^2}{2\sigma^2} \tag{4.4}$$

where A^2 is the average signal power of the baseline polarization component used in creating the selected feature vector. Returning to the example of the RR/LL feature vector, the average signal power would be calculated as:

$$A_{\frac{RR}{LL}}^2 = \frac{\sum\limits_{i=1}^{N} \left|\sqrt{\tilde{\sigma}_{RR}\left(f_i\right)}\right|^2 + \sum\limits_{i=1}^{N} \left|\sqrt{\tilde{\sigma}_{LL}\left(f_i\right)}\right|^2}{2N} \tag{4.5}$$

and the average signal to noise ratio is $A_{\frac{RR}{LL}}^2/2\sigma^2$. In Tables 7 through 11, a listing of the formulas used for calculation of average signal power for the various feature vectors are presented for clarity.

It is common practice to view system performance as a function of signal to noise ratio, where the signal power is based on the combined average power of all the members of the catalog set. In this report the plots of misclassification percentages are specified versus noise power in decibels relative to one square meter, thus independent of target signal levels. Using this signal independent feature as a reference along with a listing of average power for each target in the catalog and test sets, the misclassification performance curves can be better understood. For example, the listing of each target's average power indicates

43
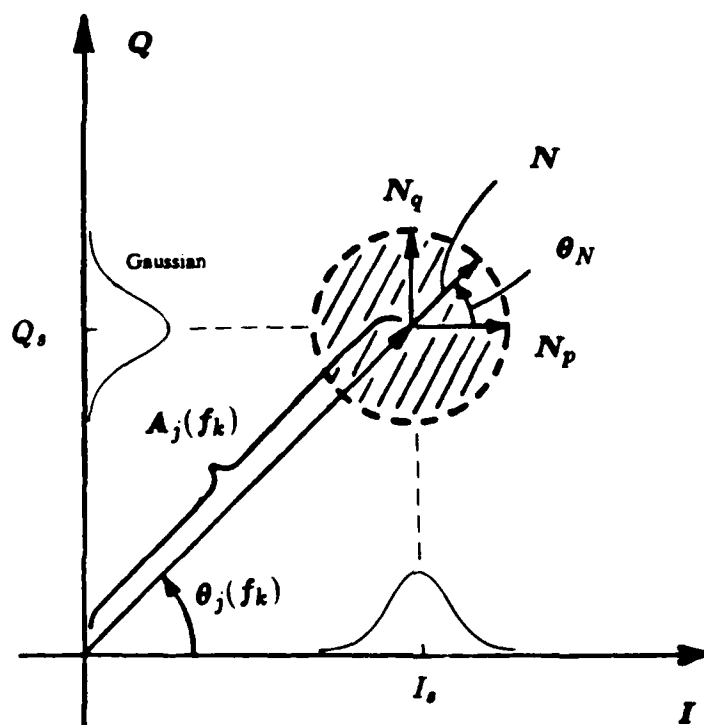
Figure 21: The Distribution of Noise about a Noise Free Data Point

44

whether or not the catalog set contains a close listing of interclass targets (i.e., it is unreasonable to place a target in a class where the average signal power of the other target signatures are orders of magnitude greater). When a large difference in magnitude exists between targets, the misclassification results tend to indicate a poorer overall performance then a set of targets with closer magnitudes would provide. That is, the targets with smaller signal powers misclassify at lower noise power levels then the larger targets, and the misclassification percentage numbers are bias to a higher level. The absolute reference of noise power also allows a fairer comparison of the different feature vector schemes. With this method the radar designer can now identify the feature vectors that are the most resistant to noise corruption; whereas the other method of specifing S/N tends to normalize this characteristic out of the misclassification curves. For example, if the specification of average signal power is not given, the S/N reference plots tend to imply that the classification performance results for a class of large cross sectional targets are the same for a class of small cross sectional targets at the same signal to noise level; even though the smaller targets might be at a noise power level of 10 dB and the larger targets at a noise power level of 20 dB.

4.3 Statistical Method for Estimating the Probability of Misclassification

In the Radar Target Identification (RTI) simulation study, estimating the probability of misclassification requires a number of independent experiments to be performed to calculate the percent of misclassification. The statistical analysis is obtained by using a different random seed for generating the independent noise in each of the experiments performed. The misclassification percentage of a target is then calculated by counting the number of times the target was incorrectly

45

classified and dividing by the total number of independent experiments performed. The average misclassification percentage is then calculated by adding all the individual target misclassification percentages and dividing by the total number of targets.

In equation form, the statistical technique for calculating the average misclassification percentage may be represented as:

$$P_E = \frac{1}{M} \sum_{j=1}^{M} \frac{m_j}{n_j} \tag{4.6}$$

where:

M is the number of signatures contained in the catalog set.

m_j is number of times test target j was incorrectly classified.

n_j is the number of independent classification experiments performed on test target j.

In any statistical analysis a margin of error is introduced, whenever a finite number of independent experiment is performed. In the RTI simulation study the statistical analysis is obtained by a finite number of experiments. To analyze the margin of error involed in a statistical analysis the confidence interval [25] must be given. The equation for the confidence interval for the RTI analysis is given as:

$$P_E = p_o \pm \xi_\alpha \sqrt{\frac{p_o(1 - p_o)}{mn}} \tag{4.7}$$

where:

m is the number of targets.

n is the number of independent experiments.

p_o is the desired probability of error.

ξ_α is such that:

46

$$\Phi(\xi_\alpha) = 1 - \frac{\alpha}{2} = \frac{1}{\sqrt{2\pi}} \int_{-\infty}^{\xi_\alpha} e^{-\frac{x^2}{2}} dx \tag{4.8}$$

where Φ is the cumulative distribution function with zero mean of a standardized normal radom variable [25].

For example, for a 90% confidence level that the misclassification level is 10%. The margin of error, with five targets and one hundred experiments, is found to be:

$$\alpha = 1 - 0.9 = 0.1$$

$$\Phi(\xi_\alpha) = 1 - \frac{\alpha}{2} = 0.95$$

$$\xi_\alpha = 1.65$$

$$p_o = 10\% = 0.1$$

$$P_E = .1 \pm 1.65 \sqrt{\frac{0.1(1-0.1)}{100*5}}$$

$$P_E = 10\% \pm 2.2\%$$

Hence, for a 90% confidence interval that the misclassification level is 10%, the margin of error is $\pm$ 2.2%.

Table 7: Average Power Calculations For Linear Polarized Feature Vectors Types

Transmit *Horizontal*, Receive *Horizontal* feature vector:

$$A^2_{HH} = \frac{\sum_{i=1}^{N} \left| \sqrt{\hat{\sigma}_{HH}(f_i)} \right|^2}{N}$$

Transmit *Vertical*, Receive *Vertical* feature vector:

$$A^2_{VV} = \frac{\sum_{i=1}^{N} \left| \sqrt{\hat{\sigma}_{VV}(f_i)} \right|^2}{N}$$

Transmit *Vertical*, Receive *Horizontal* feature vector:

$$A^2_{VH} = \frac{\sum_{i=1}^{N} \left| \sqrt{\hat{\sigma}_{VH}(f_i)} \right|^2}{N}$$

Concatenation and *Complex Sum* Linear Polarization Diverse feature vectors:

$$A^2_{LPD} = \frac{\sum_{i=1}^{N} \left| \sqrt{\hat{\sigma}_{HH}(f_i)} \right|^2 + \sum_{i=1}^{N} \left| \sqrt{\hat{\sigma}_{VV}(f_i)} \right|^2 + \sum_{i=1}^{N} \left| \sqrt{\hat{\sigma}_{VH}(f_i)} \right|^2}{3N}$$

48

Table 8: Average Power Calculations For Circular Polarized Feature Vectors Types

Transmit *Left Circular* , Receive *Left Circular* feature vector:

$$A_{LL}^2 = \frac{\sum\limits_{i=1}^{N} \left| \sqrt{\hat{\sigma}_{LL}(f_i)} \right|^2}{N}$$

Transmit *Right Circular* , Receive *Right Circular* feature vector:

$$A_{RR}^2 = \frac{\sum\limits_{i=1}^{N} \left| \sqrt{\hat{\sigma}_{RR}(f_i)} \right|^2}{N}$$

Transmit *Right Circular* , Receive *Left Circular* feature vector:

$$A_{RL}^2 = \frac{\sum\limits_{i=1}^{N} \left| \sqrt{\hat{\sigma}_{RL}(f_i)} \right|^2}{N}$$

Concatenation and *Complex Sum* Circular Polarization Diverse feature vectors:

$$A_{CPD}^2 = \frac{\sum\limits_{i=1}^{N} \left| \sqrt{\hat{\sigma}_{LL}(f_i)} \right|^2 + \sum\limits_{i=1}^{N} \left| \sqrt{\hat{\sigma}_{RR}(f_i)} \right|^2 + \sum\limits_{i=1}^{N} \left| \sqrt{\hat{\sigma}_{RL}(f_i)} \right|^2}{3N}$$

Table 9: Average Power Calculations For Linear Polarization $RATIO$ Feature
Vectors Types

$$A^2_{\substack{HH \\ VV}} = \frac{\sum\limits_{i=1}^{N} \left| \sqrt{\tilde{\sigma}_{HH}(f_i)} \right|^2 + \sum\limits_{i=1}^{N} \left| \sqrt{\tilde{\sigma}_{VV}(f_i)} \right|^2}{2N}$$

$$A^2_{\substack{HH \\ VH}} = \frac{\sum\limits_{i=1}^{N} \left| \sqrt{\tilde{\sigma}_{HH}(f_i)} \right|^2 + \sum\limits_{i=1}^{N} \left| \sqrt{\tilde{\sigma}_{VH}(f_i)} \right|^2}{2N}$$

$A^2_{\substack{VV \\ HH}}$ same as $A^2_{\substack{HH \\ VV}}$ above.

$$A^2_{\substack{VV \\ VH}} = \frac{\sum\limits_{i=1}^{N} \left| \sqrt{\tilde{\sigma}_{VV}(f_i)} \right|^2 + \sum\limits_{i=1}^{N} \left| \sqrt{\tilde{\sigma}_{VH}(f_i)} \right|^2}{2N}$$

$A^2_{\substack{VH \\ HH}}$ same as $A^2_{\substack{HH \\ VH}}$ above.

$A^2_{\substack{VH \\ VV}}$ same as $A^2_{\substack{VV \\ VH}}$ above.

50

Table 10: Average Power Calculations For Circular Polarization *RATIO* Feature
Vectors Types

$$A^2_{\substack{LL \\ RR}} = \frac{\sum\limits_{i=1}^{N} \left| \sqrt{\tilde{\sigma}_{LL}(f_i)} \right|^2 + \sum\limits_{i=1}^{N} \left| \sqrt{\tilde{\sigma}_{RR}(f_i)} \right|^2}{2N}$$

$$A^2_{\substack{LL \\ RL}} = \frac{\sum\limits_{i=1}^{N} \left| \sqrt{\tilde{\sigma}_{LL}(f_i)} \right|^2 + \sum\limits_{i=1}^{N} \left| \sqrt{\tilde{\sigma}_{RL}(f_i)} \right|^2}{2N}$$

$A^2_{\substack{RR \\ LL}}$ same as $A^2_{\substack{LL \\ RR}}$ above.

$$A^2_{\substack{RR \\ RL}} = \frac{\sum\limits_{i=1}^{N} \left| \sqrt{\tilde{\sigma}_{RR}(f_i)} \right|^2 + \sum\limits_{i=1}^{N} \left| \sqrt{\tilde{\sigma}_{RL}(f_i)} \right|^2}{2N}$$

$A^2_{\substack{RL \\ LL}}$ same as $A^2_{\substack{LL \\ RL}}$ above.

$A^2_{\substack{RL \\ RR}}$ same as $A^2_{\substack{RR \\ RL}}$ above.

51

Table 11: Average Power Calculations For *Axial Ratio* (AR) Feature Vectors Types

Transmitting *Right Circular* Polarization

$$A_{RAR}^2 = \frac{\sum_{i=1}^{N} \left|\sqrt{\tilde{\sigma}_{RR}(f_i)}\right|^2 + \sum_{i=1}^{N} \left|\sqrt{\tilde{\sigma}_{RL}(f_i)}\right|^2}{2N}$$

Transmitting *Left Circular* Polarization

$$A_{LAR}^2 = \frac{\sum_{i=1}^{N} \left|\sqrt{\tilde{\sigma}_{LL}(f_i)}\right|^2 + \sum_{i=1}^{N} \left|\sqrt{\tilde{\sigma}_{RL}(f_i)}\right|^2}{2N}$$

Concatenation of Axial Ratio Types

$$A_{AX-CAT}^2 = \frac{\sum_{i=1}^{N} \left|\sqrt{\tilde{\sigma}_{LL}(f_i)}\right|^2 + \sum_{i=1}^{N} \left|\sqrt{\tilde{\sigma}_{RR}(f_i)}\right|^2 + \sum_{i=1}^{N} \left|\sqrt{\tilde{\sigma}_{RL}(f_i)}\right|^2}{3N}$$

52

CHAPTER V

MONTE CARLO SIMULATION RESULTS

5.1 Introduction

This chapter presents the experimental results obtained through the Radar System Simulation and Evaluation (RSSE) computer study. The results are presented in five sections, where each section examines certain aspects of the radar identification techniques presented in Chapter 3 applied to the polarization diverse aircraft data base.

In Section two, a brief description of the misclassification curves are presented. In Section three, the aircraft data base is examined in two specific ways. These are:

1. Misclassification performance versus the number of frequencies.

2. Misclassification performance versus frequency bandwidth.

In Section four, misclassification performance versus classification algorithm is examined. In Section five, tradeoffs between the available feature vectors listed in Tables 2 - 6 are examined. Finally, in Section six, the examination of misclassification performance versus enlarged azimuth angle sectors.

5.2 Interpretation of Misclassification Precentage Curves

In the following sections, the classification performance of certain radar types is derived by the interpretation of the computer simulation misclassification curves.

53

In order to help clarify the reader's interpretation of the misclassification curves, a brief discussion of terms and plot characteristics is deemed appropriate.

Each curve presented in this chapter is compiled by combining the multiple output listings of the RSSE computer program for a given type of experiment. One type of experiment for a RSSE computer run may be the misclassification performance of the aircraft data base versus the number of frequencies. Another type of experiment may be the misclassification performance of the aircraft data base versus bandwidth. In Figure 22 a typical output listing of a RSSE computer run is shown. At the top of the listing, a single comment line stating the frequency bandwidth and the number of frequencies used in the radar simulation. Next, a cross-reference table mapping identification numbers to test and catalog targets at a given aspect angle, feature vector type, and average power (see Tables 2 - 6 for the feature vector types and Tables 7 - 11 for the average power calculations). For example, in the listing shown the test target ID#1 correspondes to plane #1 at a aspect angle of $0°$ azimuth and $0°$ elevation. The feature vector is the HH type (i.e., FV^{HH}) and the average power contained in the 10 frequency sample feature vector is 11.15 dBm^2.

The next portion of the output listing contains the confusion matrices at various noise power levels. In the confusion matrix, the elements in the top row correspond to the members of the catalog set and the elements in the first column correspond to the members of the test set. The numbers inside the confusion matrix represent the number of times a test target was classified as a member of the catalog set. The identification algorithm used in this example is the Non-coherent nearest neighbor distance metric. As shown in Figure 23, the 10 dBm^2 noise power level confusion matrix, test target #1 was classified eighty four times as catalog target #1, one time as catalog target #2, five times as catalog target

54

```
     140.0 - 170.0 MHz   10 Frequencies

         TEST TARGET INDEX MAPPING

  ID     TARGET        AZ (Deg) EL      TYPE     AVG POWER (DB_SM)
   1    PLANE # 1         0      0       HHP          11.15
   2    PLANE # 2         0      0       HHP          11.80
   3    PLANE # 3         0      0       HHP          15.93
   4    PLANE # 4         0      0       HHP          11.34
   5    PLANE # 5         0      0       HHP          19.96


        CATALOG TARGET INDEX MAPPING

  ID     TARGET        AZ (Deg) EL      TYPE     AVG POWER (DB_SM)
   1    PLANE # 1         0      0       HHP          11.15
   2    PLANE # 2         0      0       HHP          11.80
   3    PLANE # 3         0      0       HHP          15.93
   4    PLANE # 4         0      0       HHP          11.34
   5    PLANE # 5         0      0       HHP          19.96
```

Figure 22: Example; Output Header of a RSSE Computer Run

#3, ten times as catalog target #4, and no times as catalog target #5. A total of 100 independent experiments were performed (i.e., 84 + 1 + 5 + 10), and these 100 experiments represent the number of times the feature vector was contaminated by the additive multivariate white zero mean Gaussian noise model.

For the case shown in Figures 22 and 23, the members of the test and catalog set are identical. Therefore, the entries along the main diagonal represent the number of times the target was correctly classified while the other entries (i.e., off the main diagonal) represent the misclassification errors. At the right side of the confusion matrix a column of misclassification statistics for each test target feature vector are listed. At the bottom of the confusion matrix the average of these numbers is listed as the average misclassification percentage, and this is the number plotted in the misclassification performance curves.

A sample plot of various misclassification performance curves is shown in

```
140.0 - 170.0 MHz    10 Frequencies

Nearest Neighbor Algorithm - Vector "NON-COHERENT" distance metric

   Classification Table for Noise power =    10.00 DBSM

   TT#\CT#    1     2     3     4     5    % MIS-CLASS
           _____
      1      84     1     5    10     0      16.00
      2       4    86     3     7     0      14.00
      3       0     0   100     0     0       0.00
      4      13     9     5    73     0      27.00
      5       0     0     0     0   100       0.00
           _____


       Average mis-classification percentage :   11.40 %

  Mis-classification percentage is based on the test targets name.
```

Figure 23: Example; RSSE Confusion Matrix Computer Listing

Figure 24. The solid curve represents the result from the previously discussed confusion matrix. Every plot shown in this report will have the same format as shown in Figure 24. A header of information is provided at the top left hand corner of every plot explaining the characteristics of the radar simulation performed. The header is comprised as follows:

Line 1.   Data Base Type. (i.e., aircraft, ships, ect..)

Line 2.   Feature Vector Type. (See Tables 2 - 6)

Line 3.   Identification algorithm. Non-coherent,coherent nearest neighbor
           or time domain cross correlation.

Line 4.   Aspect Angle. Azimuth, elevation, and roll orientation.

Line 5.   Start and Stop frequencies. The frequency samples used are evenly
           spaced samples including the start and stop frequencies.

Line 6.   Number of frequencies.

Line 7.   Number of test and catalog targets.

Line 8.   Number of independent experiments performed.

Line 9.   90% confidence interval at the 10% misclassification level.

If any of the parameters in the header block is replaced by the word "key", then this parameter is the tradeoff parameter of a multi-curve misclassification plot. Each curve in the misclassification plot is identified in the key located at the bottom of the plot. The key will contain an identifing line type with a brief explanation of what the line type represents. In the example misclassification plot shown in Figure 24, the key has a listing of two parameters representing curves with the non-coherent and coherent nearest neighbor identification algorithm.
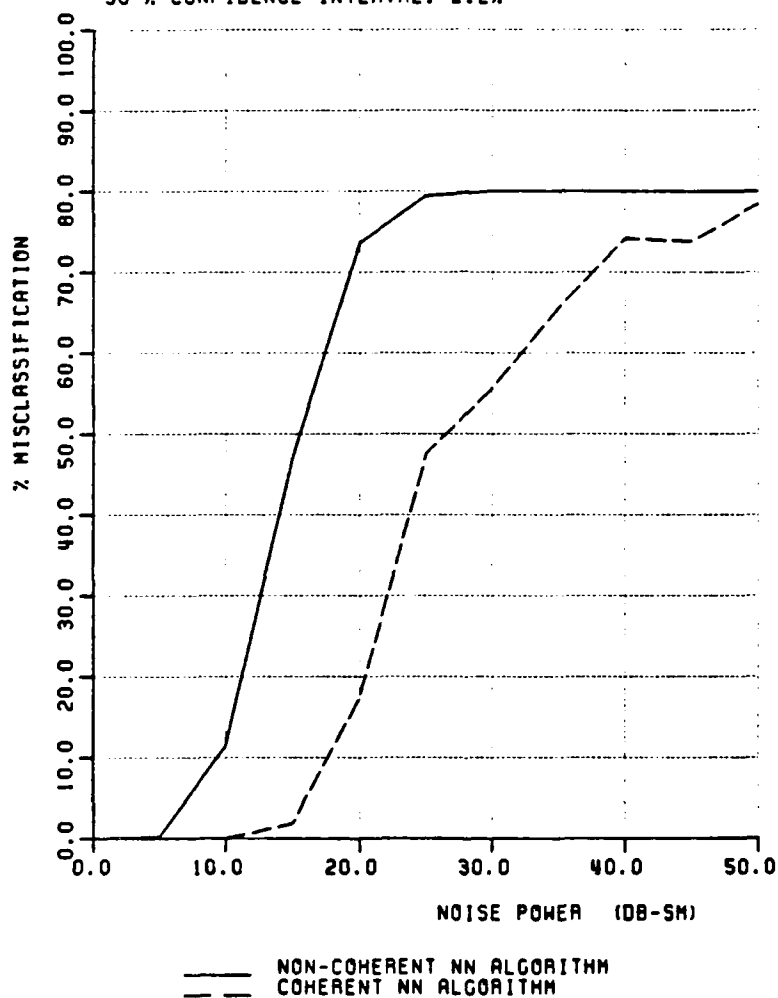
Figure 24: Example; Plot of Misclassification performance Curves

58

5.3 Number of Frequencies, and Bandwidth Study

This section presents a number of misclassification curves in order to examine various bandwidths, and the number of frequency samples required within the bandwidth, that provide optimum levels of classification performance.

Five frequency bands were chosen to examine the performance of the classification parameters. The bands spanned the entire range of the usable data in the data base and consisted of one 8 MHz band, three 30 MHz bands, and one 50 MHz band. Four of these bands were created from the low-frequency aircraft data base, and consisted of overlapping frequency bands that resulted in additional insight on the aircraft behavior to the identification techniques employed. The four scaled frequency bands from the low-frequency data base are: 8-16 MHz, 8-38 MHz, 30-60 MHz, and 8-58 MHz. The high-frequency 30 MHz band is 140-170 MHz.

From previous discussions, it is expected that the lower frequency data base should provide good classification performance. Since the frequencies in the 8 - 58 MHz band are closer to the resonance region (see Figure 15), the radar signature will tend to vary less as the aspect angle changes compared with that of higher frequencies in the 140 - 170 MHz band. In terms of scattering centers, at the lower frequencies the spacing between two scattering centers is relatively small in terms of wavelengths; therefore, the scattering mechanisms are less sensitive to small changes in aspect. For example, the two source single plane phase interference equation, $\frac{2\pi d}{\lambda}cos(\theta)$, shows that a higher frequency will produce a much faster slope change versus aspect angle due to the $\frac{1}{\lambda}$ term. So for a complex target (i.e., one with many scattering centers), a small change in aspect angle will generally produce a greater change in the radar signatures at a higher frequency then a lower one. Therefore, the lower frequency bands should be more reliable

59

and should provide better overall classification performance.

In choosing the correct number of frequencies, the time - frequency - distance relationships of electromagnetics can serve as a guideline of design. To illustrate this concept Figure 25 shows a time domain representation of a fictious backscattered response of a plane wave (impulse) traveling along the length of the aircraft. If a receiver were positioned at the nose of the aircraft to receive the backscattered energy, it would see the response from the nose as soon as the plane wave reached the aircraft (i.e., at time t_0). The response due to scattering at 25 meters down the length of the aircraft would be seen at $t_0 + 2t_1$ (i.e., the time it takes the wave to travel down 25 meters, scatter and travel back to the nose of the aircraft), and the end of the aircraft would be seen at $t_0 + 2t_2$. From the time-frequency-distance relationship $\frac{c}{\Delta f} = 2l$, where l is the length of the target, Shannon's sampling theorem requires that the frequency sampling rate Δf satisfy $\Delta f \leq \frac{c}{2l}$.

The five aircraft used in this simulation study have an average length of approximately 50 meters. This implies that the sampling rate has to be at least 3 MHz. So for bandwidth 8, 30, and 50 MHz, approximately 3, 10, and 17 evenly spaced frequencies, respectively, are needed to represent the target signature and meet Shannon's criterion. However, since higher order mechanism do exists, such as double diffraction, creeping wave, and the ringing associated with the resonance condition, the time duration of the target's signature tends to be increased beyond the time it takes to traverse the physical length of the target (i.e., $t_0 + 2t_2$).

Examination of the transformed frequency samples to the time domain reveals that the response of the aircraft scatterers typically die out before 3.5 transit times across the overall length of the target. Therefore, the sampling rate becomes $\Delta f \leq \frac{c}{3.5l}$.

60
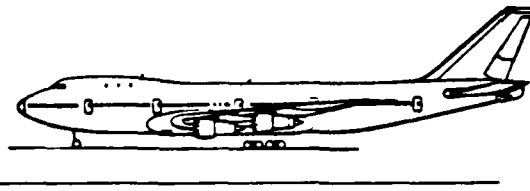
t_0 t_1 $t_2 = 166.6$ n-sec

0 meters   25 meters   50 meters

t_0 $t_0 + 2t_1$ $t_0 + 2t_2$

                                                 333.3 n-sec

0 meters   50 meters   100 meters
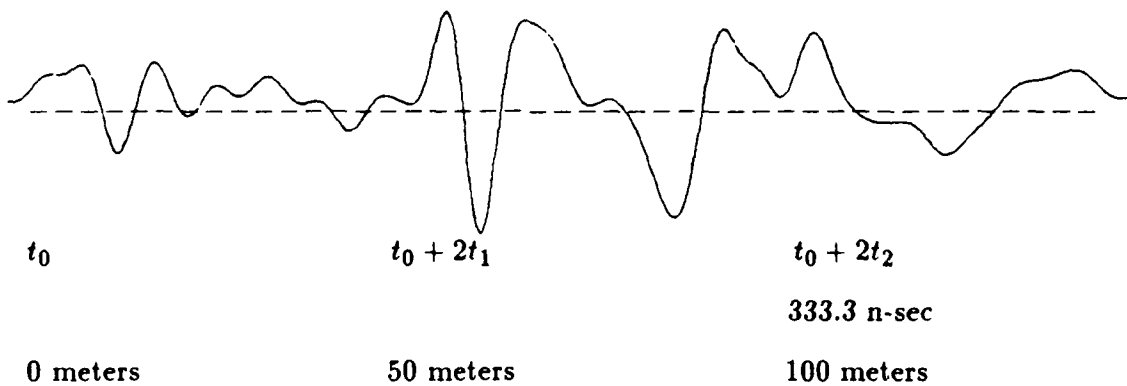
Frequency/Time/Distance relationship for 3.5 transit lengths

$$Tc = \frac{c}{\Delta f} = 3.5 * 50 = 175 \text{ meters}$$

So for a bandwidth of:

     8 MHz, need $\approx$ 5 frequencies

     30 MHz, need $\approx$ 18 frequencies

     50 MHz, need $\approx$ 29 frequencies

Figure 25: Time Domain Plane Wave Backscattered Response

Figures[1] 26 through 30 show a set of misclassification plots for the nose on (i.e., 0 degree azimuth) aspect angle. The five figures illustrate the misclassification performance curves for each of the five bandwidth versus the number of frequencies samples. The non-coherent distance metric was used in each of the plots and the average signal power of the combined targets in the catalog set is identified on each plot by the symbol "AP". Note that the clustered breakaway point from the 0% misclassification level starts at about 15 frequencies for the 30 MHz bandwidths. If 15 frequencies are chosen, the time-frequency-distance relationship calculates a length of 150 meters as the effective target length. This calculated length supports the statement that the backscattered response typically dies out before 3.5 transit times across the overall length of the targets.

Examination of the five plots simultanously, reveals that the 8 - 16 MHz band provides the best classification performance versus noise power. The average signal levels of the feature vector elements in this band are larger than those in the other bands. For this reason the elements have a better noise immunity and thus provides better classification performance. Further examination of the plots show that when the number of frequencies do not meet the Shannon sampling criterion large drops in classification performance can be expected. At 2 frequencies, the 8 MHz bandwidth plot shows a 15 dB or more drop in noise immunity. When the sampling rate is much more than the required Shannon rate, little or no improvement in classification performance is gained while the cost and time required to process the additional frequencies is increased.

In Figures 31 through 34, bar graphs are shown comparing the misclassification performance at four different aspect angles at the 20 dBm^2 noise power level for the 10 frequency case. Even though the 10 frequency case may not be fair

---

[1] All remaining figures are located at end of Chapter 5.

62

when comparing different size bandwidths (i.e., Shannon's argument for minimum number of frequencies), it allows the radar designer to compare performance as a function of frequency samples. Ten frequencies were chosen because they provided good classification performance in all the examined bandwidths. The results show that the 8-16 MHz band also provides the best overall classification performance for the four aspect angle examined.

Another aspect which should be mentioned when comparing the performances of the five bandwidths is the background clutter and noise characteristics across the frequency bands. Before a final decision can be made on the best frequency band for radar target identification, a study on the background clutter and noise characteristics over the frequency bands of interest must be made. Once the background noise levels are found; the corresponding misclassification levels for each bandwidth can be found from the plots presented above, and the best performing bandwidth can be chosen.

5.4   Classification Algorithm Study

In this section, the three identification algorithms available in the RSSE computer program are examined. The three algorithms are the non-coherent nearest neighbor, the coherent nearest neighbor, and the time domain cross correlation methods as discussed in Chapter 3. As with the first section of results, the performance of the identification algorithms are examined by the simulation results contained in the percent misclassification performance curves generated by the RSSE computer program.

Figures 35 through 40 show the misclassification performance results for the three algorithm types in the 8-16 MHz and 8-38 MHz frequency bands. Each plot contains three curves of the HH feature vector type, and each curve represents one

63

of the three algorithm types. Additionally, the plots show the misclassification performance levels of the algorithms at 2, 5, and 10 frequencies for the 8-16 MHz band in Figures 35, 36, and 37, respectively, and 5, 10, and 15 frequencies for the 8-38 MHz band in Figures 38, 39, and 40, respectively. In each case, at the 5% misclassification level, approximately a 6 dB improvement in noise immunity is gained over the Non-coherent Nearest Neighbor algorithm by the Time Domain Cross Correlation algorithm (TDCC), and another 3 to 5 dB improvement is gained over the TDCC algorithm by the Coherent Nearest Neighbor algorithm. The plots also reveal that an identification error rate as low as 5% can be achieved at a signal to noise ratio of about 0 dB when accurate intrinsic phase information is available (i.e., coherent nearest neighbor algorithm). This result shows that the cost of using phase information is clearly worth the effort in both processing and measuring. A 10 dB improvement in noise immunity over the non-coherent method is a significant gain in classification performance.

While measuring the intrinsic phase of a target for coherent nearest neighbor processing requires an extremly accurate knowledge of range to a target phase reference, the time domain cross correlation method has the property of range independence through the correlation process. Tradeoff such as the processing time for the correlation process and the range resolution requirements for the coherent nearest neighbor must be examined if both methods meet the desired classification performance levels.

Another option for utilizing phase information, without the stringent range or process requirement, has been presented in earily works [16,17]. The method uses the coherent nearest neighbor algorithm but employs the use of the relative phase between the frequency samples instead of the intrinsic phase of the target.

64

The relative phase method is defined as :

$$W_i = \theta_i \lambda_i - \theta_{i+1} \lambda_{i+1} \tag{5.1}$$

where θ_i is the measured phase at wavelength λ_i and i = 1, ... N - 1 (where N = number of frequency samples). Equation (5.1) assumes that the range to the target between frequency interrogations differ by a small amount.

While this method also avoids the processing time required by the TDCC method by utilizing the coherent nearest neighbor algorithm, the W_i method of phase processing can present even poorer classification performance than processing without any phase information at all (i.e., non-coherent nearest neighbor). This situation arises when the relative phase difference is small in value, the noise corruption will tend to blend the samples together in such a way that the level of classification performance is worse than the non-coherent processing method.

5.5   Classification Results for Feature Vector Types

5.5.1   Introduction

In this section, the misclassification performance levels of the 26 feature vectors available in the RSSE computer program are examined. As discussed in Chapter 3, various feature vector types provide properties that may be advantagous to certain target identification situations. For example, the ratio feature vector types such as the $FV^{HH/VV}$ and $FV^{VV/HH}$ have the property to cancel out multiplicative type errors by virtue of the division of the backscattered coefficients. The circular polarized feature vectors tend to be insensitive to roll of the aircraft especially in the symmetric cases of nose-on and tail-on incident angles.

It must be remembered the the characteristics mentioned above for the ratio type and circular type feature vectors were not explicitly exploited in this report.

65

That is, a multiplicative noise model was not available nor was other aspects angles that included roll angles other than 0 degrees.

However, the tradeoff between the feature vector types is examined from the stand point of performance versus additive multivariant white Gassian noise. In this tradeoff analysis of feature vector types, the performance is analyzed by keeping the feature space at a constant size and calculating the error probabilities by a pairwise classification between all possible pairs formed by the five airplanes: Concord, DC10, 707, 727, and 747. Most of the performance curves presented in this section are representative of the 8-16 MHz band, 10 sample frequencies, and the coherent Nearest Neighbor distance metric. This combination was chosen because it provided the highest immunity to additive noise.

5.5.2 Linear Polarized Feature Vectors

Figures 41 through 43 show curves representing misclassification results for the three linear polarization types. The misclassification performance curves for the feature vectors FV^{HH}, FV^{VV}, and FV^{VH}, are plotted in Figures 41, 42, and 43. respectively. Four performance curves are plotted in each figure, each representing one of four different radar illumination aspect angles. The aspects are at $0°$, $45°$, $90°$, and $180°$ azimuth, with $0°$ elevation and roll. In the KEY, beside each aspect entry, the average power contained in the catalog set is listed.

Examination of the plots shows that the horizontal-horizontal feature vector, FV^{HH}, that consists of the backscattered radar returns of incident illumination parallel to the fuselage and the wings at low incident elevation angles, tend to produce higher backscattered energy return than the vertical transmit-receive feature vector FV^{VV}. This property results in a higher noise immunity and better classification performance levels. It is also noted that the signal to noise ratio.

66

between the 0% misclassification breakaway point is smaller for the VV feature vector type than for the HH feature vector type. This would tend to indicate that the VV feature vector type may have a better discrimination property that its orthogonal counter part (i.e., the HH feature vector type). A close grouping of misclassification performance curves for both the HH and VV feature vector types is encountered for the four different aspect angle examined. Misclassification levels lower than 10% at signal to noise ratios of 0 dB are also achieved when accurate phase information is available.

The third plot (Figure 43), which represents the VH feature vector type, shows that the classification performance is highy aspect dependent. For the 0° and 180° aspect angles a large drop in classification performance is encountered. The cross-pol feature vector has the characteristic of a null backscattered radar return for symmetric objects. Symmetry is encountered at the 0° and 180° aircraft aspects; therefore, resulting in a low backscattered radar return for the VH polarization scheme. The VH feature vector type can always be expected to have a lower backscattered signal return than the HH and VV feature vector types; unless, the target's major axis is oriented along a 45° angle relative to the horizontal and vertical polarizations. The 45° orientation would result in backscattered energy returns comparable to the HH and VV radar types.

For the linear polarization feature vector types the 90° azimuth angle tends to produce the best classification results in the all bandwidths studied. While this is not surprizing, since at this aspect the large surface area of scattering produces a high energy return signal, earlier studies based on a signal to noise ratio normalization did not indicate this result.

5.5.3 Circular Polarized Feature Vectors

The next series of figures are the circular polarized feature vectors FV^{RR}, FV^{LL}, and FV^{RL}. These feature vectors were found to have performance levels of classification very close to that of the Linear Co-polarized feature vectors (i.e., FV^{HH}, and FV^{VV}). While the circular polarized radars at HF frequencies do not exhibit any added advantage of clutter rejection over the linear polarized radars (they do in the microwave region). The circular polarized radars do have a better aircraft roll independence especially in the head-on and tail-on aspect angles. Because of the symmetry of a aircraft at nose-on and tail-on incidence, most of the circular polarization backscattered responses from the co-polarized RR and LL feature vectors types are the result of secondary and higher interaction effects with the electromagnetic signal. For example, the first ordered scattered radar return from an infinite plate perpendicular to the propagation direction of a incident right circular wave is left circular, and the backscattered energy not be received by a right circular transmitting antenna.

Figures 44 and 45 show the performance curves for the circular co-polarized feature vectors FV^{RR} and FV^{LL}. The curves, at the same aspect angles shown previously in the linear polarized feature vectors performance curves, exhibit classification performance levels very close to that of the co-polarized linear feature vectors. While the HH and VV linear feature vector types provide better classification performance at the symmetric aspect angles of $0°$ and $180°$ than the asymmetrical aspect angle of $45°$, the LL and RR circular feature vector types do not. Because of the LL and RR feature vectors second order nature to symmetric aircraft look angles, the $0°$ and $180°$ aspect angles misclassification performance levels are below that of the $45°$ aspect angle. Note also that the $0°$ and $180°$

68

performance curves in LL feature vector plot are almost identical to the 0° and 180° curves in the RR feature vector plot. This should be expected, since the linear to circular polarization transformations for the LL and RR backscattered coefficients become identical for any target positioned at a symmetric look angle (see Appendix A).

The RL feature vector plot (Figure 46) shows that the performance curves still hold levels of classification performance close to that of the co-polarized circular feature vectors. The circular cross-pol feature vector (FV^{RL}) maintains a good grouping of performance curves versus the change in aspect as opposed to that of the linear cross-pol feature vector (FV^{VH}) shown in Figure 43. At the 0° and 180° aspect angle, the RL backscattered signal return is now a first order effect and dominates the other aspect angles in the region below the 5% misclassification level.

5.5.4 Ratio Feature Vector Types

5.5.4.1 Linear Polarized Ratio Feature Vectors

The ratio feature vectors provided a varying degree of performance levels. The performance for most of the ratio feature vector types has shown to be highly dependent on the interrogation angle. Figures 47 through 52 show the misclassification performance plots for the six possible ratio combinations of the linear polarization backscattered components $\sqrt{\tilde{\sigma}_{HH}}$, $\sqrt{\tilde{\sigma}_{VV}}$, and $\sqrt{\tilde{\sigma}_{VH}}$ (see Table 4). As with the previous data shown in this chapter, the plots illustrate a pairwise classification of alike catalog and test sets containing five feature vectors (i.e., one for each of the five aircraft). Again, 100 experiment and the coherent NN distance metric were used for the RTI simulation.

Comparing the six plots shows that the feature vector type VV/HH give the

best classification results at each of the aspects examined (i.e., 0°, 45°, 90°, and 180° aspects). The other plots illustrating the ratio feature vector types with the $\sqrt{\tilde{\sigma}_{VH}}$ and $\sqrt{\tilde{\sigma}_{VV}}$ backscattered components in the denominator tend to have a wide spread in misclassification performance versus aspect angle. This is especially evident in the feature vector types HH/VH and VH/VH. In both cases at the aspect angles of 0° and 180° the misclassification levels are very high relative to the other curves at 45° and 90°. At these angles (i.e., 0° and 180°) the VH backscattered coefficients are at a very low level due to the symmetry of the target at these aspects. This causes the VH backscattered coefficient to be very unstable at high noise levels causing the ratio feature vectors containing the $\sqrt{\tilde{\sigma}_{VH}}$ component in the denominator to attain poor classification performance. In fact, all the ratio types that have a component in the denominator which contains less signal energy than that of the numerator component exhibit poor classification performance. As for the best performing linear polarized ratio feature vector, $FV^{VV/HH}$, the HH co-pol radar contains the strongest field components and provides the most stable term for the denominator. This fact is evident by the close grouping of performance curves for the four aspect angle tested in the $FV^{VV/HH}$ feature vector, the 0% misclassification breakaway point spans a noise power range of approximately 12 dB while the other ratio feature vectors may span as much as 20 to 30 dB in noise power.

Compared to the HH feature vector performance curves presented in Figure 41, where the 0% misclassification level for all aspects is at a noise power level of approximately 20 dB, the performance of the ratio type feature vectors generate little excitement. But one must be careful not to make such a direct comparison between the two types of feature vectors without considering the reasons that a ratio feature vector type may be implemented. As stated in Chapter 3, the

70

ratio feature vector (a relative relationship) may be more useful in an environment where intrinsic (exact) measurements may be hard to obtain, such as in an Over The Horizon (OTH) radar system where ionospheric propagation tend to make calibration of intrinsic data very difficult. Also the ionospheric induced errors contain multiplicative components that the ratio quantity has higher immunity too by virtue of cancellation by division of the two backscattered coefficients.

5.5.4.2 Circular Polarized Ratio Feature Vectors

Figures 53 through 58 show the misclassification performance plots for the six possible ratio combinations of the circular polarized backscattered components $\sqrt{\bar{\sigma}_{RR}}$, $\sqrt{\bar{\sigma}_{LL}}$, and $\sqrt{\bar{\sigma}_{RL}}$ (see Table 5). As with the linear polarized ratio feature vectors, the circular polarized ratio feature vectors that have a lower energy component in the denominator tend to have a wider span of classification performance for the four aspect angles examined.

For the circular polarized ratio feature vectors, no one ratio type stands out as the best performer for the four aspects examined. Although the feature vector types RL/RR and RL/LL have a better overall grouping of performance curves for the four aspects, they do not provide the best classification performance levels. For the best results, a polarization agile radar system capable of measuring all the polarizations needed to construct the optimal ratio types for a given aspect would provide the best performance. With this system, and *a priori* knowledge of the aspect of the target (i.e., from tracking information), the optimized circular ratio feature vectors would provide very acceptable levels of performance at all aspect angles. Figure 59 shows a polarization agile system providing the best classification performance for the four examined aspects. The system utilizes the LL/RL ratio type for the near broadside aspects, the RR/LL or RL/LL type for the 45° aspect,

71

the RL/LL type for the 0° aspect, and the RL/RR type for the 180° aspect angle. With the polarization agile implementation, and the quasi roll independence of the circular components, the circular polarized ratio feature vector provides slightly better classification performance then the best linear polarized ratio vector feature type VV/HH.

5.5.5 Polarization Diverse Feature Vectors

As presented in Chapter 3, the polarization diverse feature vectors utilize the full backscattered polarization matrix, that is, for a linear diverse feature vector the backscattered components $\sqrt{\tilde{\sigma}_{HH}}$, $\sqrt{\tilde{\sigma}_{VV}}$, and $\sqrt{\tilde{\sigma}_{VH}}$ are used in the construction of the feature vector (see Table 2). The components $\sqrt{\tilde{\sigma}_{RR}}$, $\sqrt{\tilde{\sigma}_{LL}}$, and $\sqrt{\tilde{\sigma}_{RL}}$ are used in the construction of a circularly polarized diverse feature vectors (see Table 3). One advantage of a polarization diverse feature vector, such as the concatenation type feature vector, is: by utilizing the three polarization components a large feature space is created with only a few frequency samples.

Figures 60 through 63 show four plots of misclassification curves illustrating the performance of two types of polarization diverse feature vectors. Figures 60 and 61 show the concatenation type feature vector for the linear and circular polarized components, respectively. As in preceeding sections, 100 independent experiments were performed with the coherent nearest neighbor distance metric. Instead of using 10 equally spaced frequency only 4 equally spaced frequency samples across the GHz band were chosen for this case. Four frequency samples provides a 12 element concatenation feature vector (i.e., # of frequency samples * 3 polarization components, thus keeping the feature space dimension close to the 10 element space of the preceeding sections.

Here the levels of classification performance are very close to that

72

of the HH, RR, LL, and RL feature vectors types. With performance levels so close and the feature space size approximately equall; the basis for choosing a polarization diverse feature vector may lie in the cost of frequencies versus the cost of polarization agility. That is, whether the cost of six to eight additional frequency interrogations is more or less than the cost and of measureing two additional polarizations states.

Figures 62 and 63 show another type of polarization agile processing. These plots represent a summation of the three linear polarized (see Table 2) and three circular polarized (see Table 3) components at each frequency sample, respectively. As with the concatenation feature vector types presented above, Figure 62 and 63 represent a feature vector at four evenly spaced frequency samples. But, instead of yielding a 12 element feature vector only a 4 element feature vector is created. In Figure 62 the linear polarized summation feature vector type presents a 0% misclassification level from approximately 10 to 15 dBm^2 in noise power for four aspect angles examined. In Figure 63 the circular polarized summation feature vector type presents a 0% misclassification level clustered at a noise power level of approximately 17 dBm^2 for the four aspects. While the classification performance of the summation feature vector types is slightly less then that of the concatenation types, only four elements are contained in the feature vector versus 12 for the concatenation feature vector type.

In both types of polarization diverse feature vectors, the circular polarized feature vector perform at levels close to, or better, than their linear polarized counterparts. With the additional quality of immunity to the roll of a symmetrical target, the circular polarized diverse feature vectors present a appealing classification tool.

The linear polarized diverse feature vector may be improved by the deletion

of the VH component. As seen in Section 5.5.2, the VH component exhibits poor classification performance at the nose-on, and tail-on aspect angles. A concatenation and summation feature vector utilizing only the VV and HH components may prove to be significately better than the VV, HH, and VH combination for an equivalent feature space dimension.

5.5.6 Axial Ratio Feature Vectors

The axial ratio feature vectors are a non-coherent combination of the circular backscattered coefficients (see Table 6).

Figures 64 through 66 show the misclassification results for transmitting left circular (LAR), transmitting right circular (RAR), and a concatenation of the two. Figures 64 and 65 show that the performance of the non-coherent quantities are at noise power levels of about 10 to 15 dB below that of the coherent VV, HH, RR, LL, RL feature vector types employing the same feature space (i.e., 10 frequency samples). Even with the concatenation of the two axial ratio feature vector types RAR and LAR, the classification performance is increased only 5 dB while the feature spaced is doubled (Figure 66). Like the ratio feature vector types presented in Section 5.5.4, the use of axial ratio feature vectors could provide some additional noise immunities qualities in a multiplicative noise environment.

5.6 Classification Results for Larger Aspect Zones

In this section the classification performance of larger aspect zones is analyzed by expanding the catalog and test sets of the RSSE computer program. The experiments are performed by adding additional target feature vectors to the catalog and test sets at increments of $10°$. As in preceeding sections, 100 independent experiments were performed with 10 frequency samples, and the coherent nearest

neighbor distance metric. For this study, however, only the HH feature vector type and the 30 MHz bandwidth from 8-38 MHz were chosen to illustrate the performance of the larger aspect zones. As previously presented, the 10 frequency sample HH feature vector provides very good classification performance levels versus noise power. Also, the 8-38 MHz band is very close to the 8-16 MHz band in misclassification performance.

To begin this study, a set of "baseline" classification performance curves were generated. These curves, which serve as a reference to compare to the classification performance of the larger aspect zones, represent a pairwise classification between five feature vectors (one per target) in the test and catalog sets for each aspect angle examined. Figures 67 through 70 show the reference curves for azimuth aspects ranging from $0°$ to $180°$ by increments of $10°$ (azimuths angle of $120°$, $130°$, and $140°$ are not included). The four plots show that the misclassification levels of 1% range from 19 to 25 dBm^2 in noise power for all aspects. From the four figures the best classification performance levels are obtained at nose-on, tail-on, broadside, and close broadside (i.e., angles from $70°$ to $110°$). The worst classification performance is seen in the forward sector, at the aspect angles of $10°$ and $20°$, where the backscattered signal power is at a minimum.

Before the curves representing the misclassification performance of the larger aspect zones are analyzed; two output listings from the RSSE computer program are presented to clarify the counting of misclassification statistics for the larger aspect zones.

Shown in Figures 71 and 72 are the two computer output listings representing the misclassification statistics for a two angle and a three angle test and catalog set, respectively. In Figure 71 the Test Target Numbers (TT#) and the Catalog Target Numbers (CT#) are numbers ranging from 1 to 10. In each set the target

75

numbers 1&2, 3&4, 5&6, 7&8, and 9&10, represent the 0° & 10° azimuth angle positions for each of the five aircraft. Blocks enclosing the two angles represent the number of times the targets were correctly classified. Outside the blocks are the numbers of times the target feature vector was misclassified. For example, test target feature vector #1 was considered correctly classified 97 times (86 + 11), 86 times being the correct vector and 11 times being the wrong vector but the correct target. Therefore, out of 100 experiments, TT#1 was misclassified only 3 times (3%), once as target #2, once as target #3, and once as target #4. The average misclassification percentage for this case is the average of the 10 individual TT# misclassification percentages listed at the far right column of confusion matrix. The average misclassification percentage for the 10 dBm^2 noise power confusion matrix shown in Figure 71 is 9.2%. Finally, the numbers plotted are the average misclassification numbers tabulated from the incremented noise power confusion matrices.

Figure 72 shows a confusion matrix for a 3 angle test and catalog set at the noise power level of 30 dBm^2. In this section the misclassification performance results from a 4 angle test and catalog set are also presented, and the misclassification statistics for both the 3 and 4 angle cases are treated in a similar manner as the 2 angle test and catalog set presented above.

Figures 73 through 75 show the results for the two, three, and four, angle catalog sets for the forward aspect sector (i.e., 0, 10, 20, and 30 degrees). In Figure 73 the curves for the two angle catalog sets contains three performance curves representing the 0° & 10°, 10° & 20°, and 20° & 30° aspects. The performance curves in Figure 73 tend to reach a level of classification performance between the two individual angle cases shown in Figure 67 (i.e., the 0° & 10° performance curve lies between the 0° and 10° performance curves of Figure 67, ect...). Increasing

the catalog set to the three angle case, a 30° aspect zone, the classification performance decreases to the level of the worst single angle performance curve included in the three angle set (see Figure 67). Figure 74 shows two misclassification performance curves representing three angle catalog cases of 0° & 10° & 20°, and 10° & 20° & 30°. In each case the misclassification performance curves reach the level of performance of the 10° single angle case of Figure 67. Finally, in Figure 75 the four angle case for the forward sector is shown along with the four angle catalog sets representing the single angle catalog sets shown in Figures 68 through 70. In each cases the 0% misclassification level is attained at the level of the worst performing single angle catalog of the sector under test. The four angle forward sector catalog set attains misclassification levels at approximately the performance levels of the 10° single aspect angle catalog set shown in Figure 67. The four angle catalog set of 40°, 50° 60°, and 70°, attains misclassification levels at approximately the performance levels of the 60° single aspect angle catalog set shown in Figure 68. The four angle catalog set of 80°, 90° 100°, and 110°, attains misclassification levels at approximately the performance levels of the 100° single aspect angle catalog set shown in Figure 69. The rear sector four angle catalog set attains misclassification performance levels at approximately the performance levels of the 170° single aspect angle catalog set shown in Figure 70. The results clearly show that the misclassification statistics of an expanded angle catalog set perform at levels approximately equal to the statistics of the worst single angle catalog in the expanded catalog set.

```
DATA BASE TYPE: AIRCRAFT
FEATURE VECTOR TYPE: HH
ALGORITHM TYPE: NON-COHERENT NN
AZIMUTH: 0     ELEVATION: 0     ROLL: 0
START FREQUENCY: 8  MHZ    STOP FREQUENCY: 16 MHZ
NUMBER OF FREQUENCIES: KEY
CATALOG SET VECTORS: 5    TEST SET VECTORS: 5
NUMBER OF EXPERIMENTS: 100
90 % CONFIDENCE INTERVAL: 2.2%
```
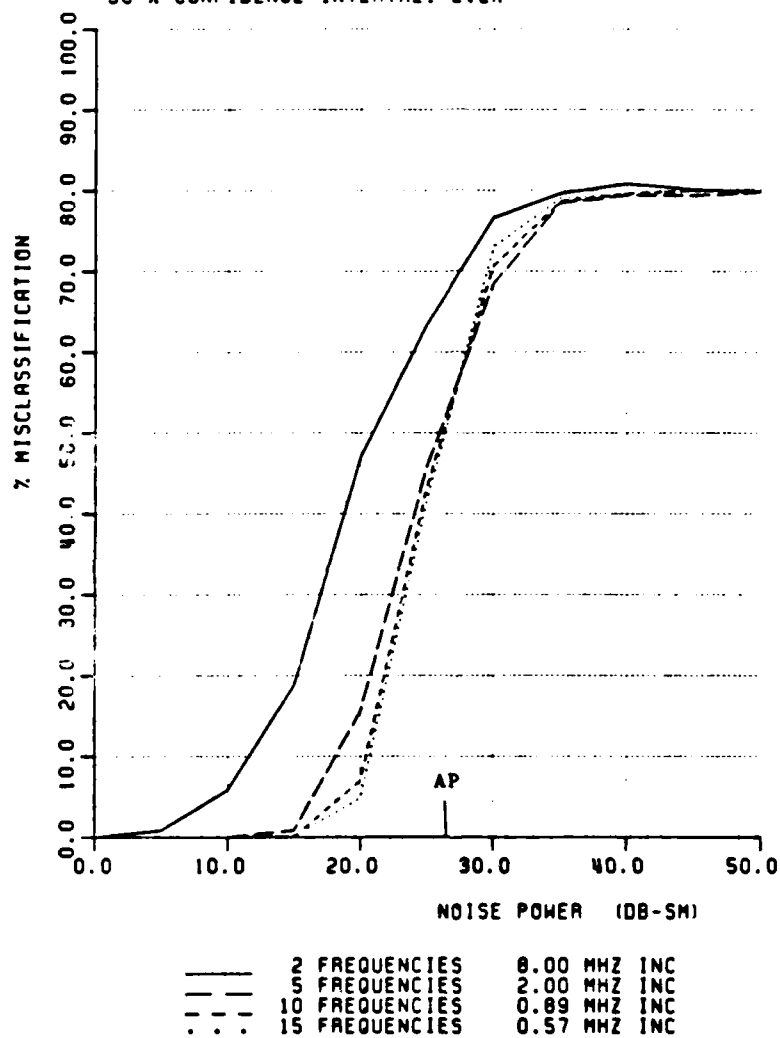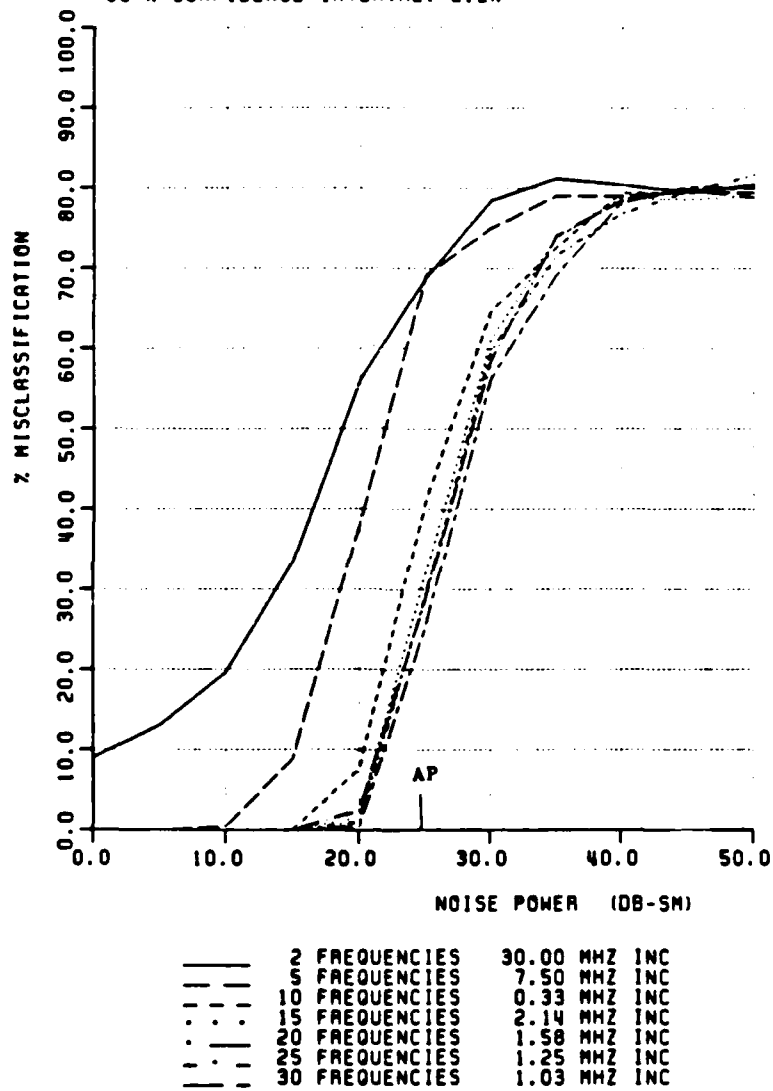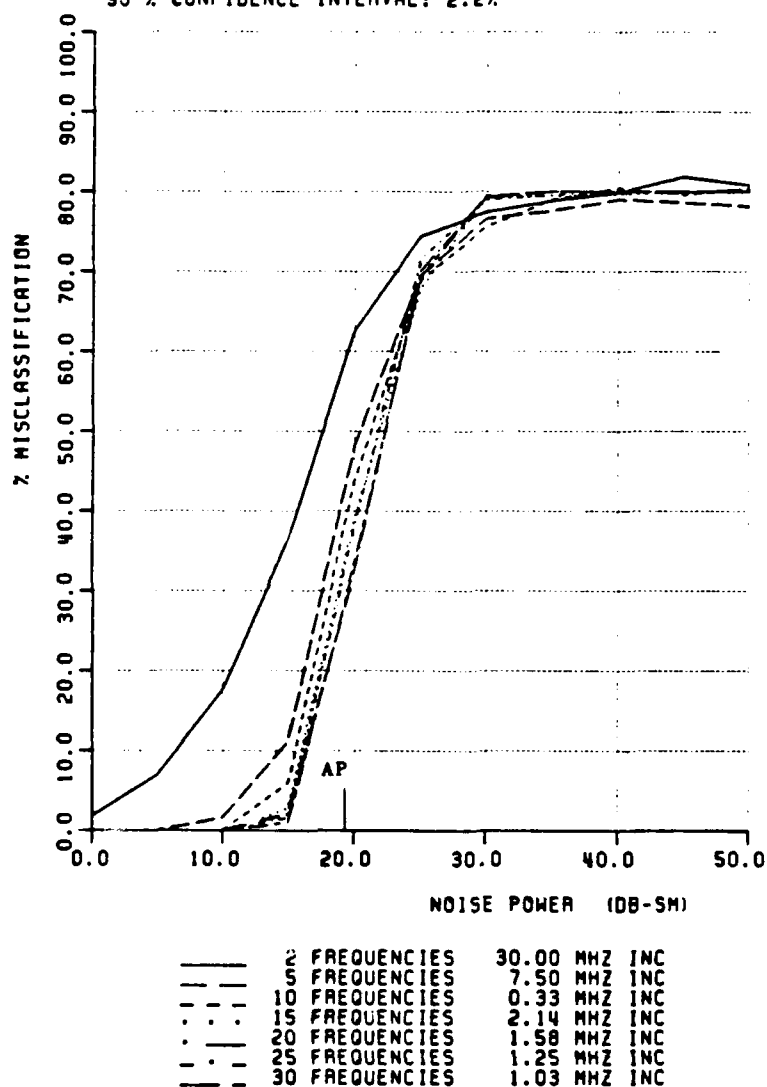
Figure 26: Number of Frequency Study for the 8-16 MHz Bandwidth

78

DATA BASE TYPE: AIRCRAFT
FEATURE VECTOR TYPE: HH
ALGORITHM TYPE: NON-COHERENT NN
AZIMUTH: 0   ELEVATION: 0   ROLL: 0
START FREQUENCY: 8 MHZ   STOP FREQUENCY: 38 MHZ
NUMBER OF FREQUENCIES: KEY
CATALOG SET VECTORS: 5   TEST SET VECTORS: 5
NUMBER OF EXPERIMENTS: 100
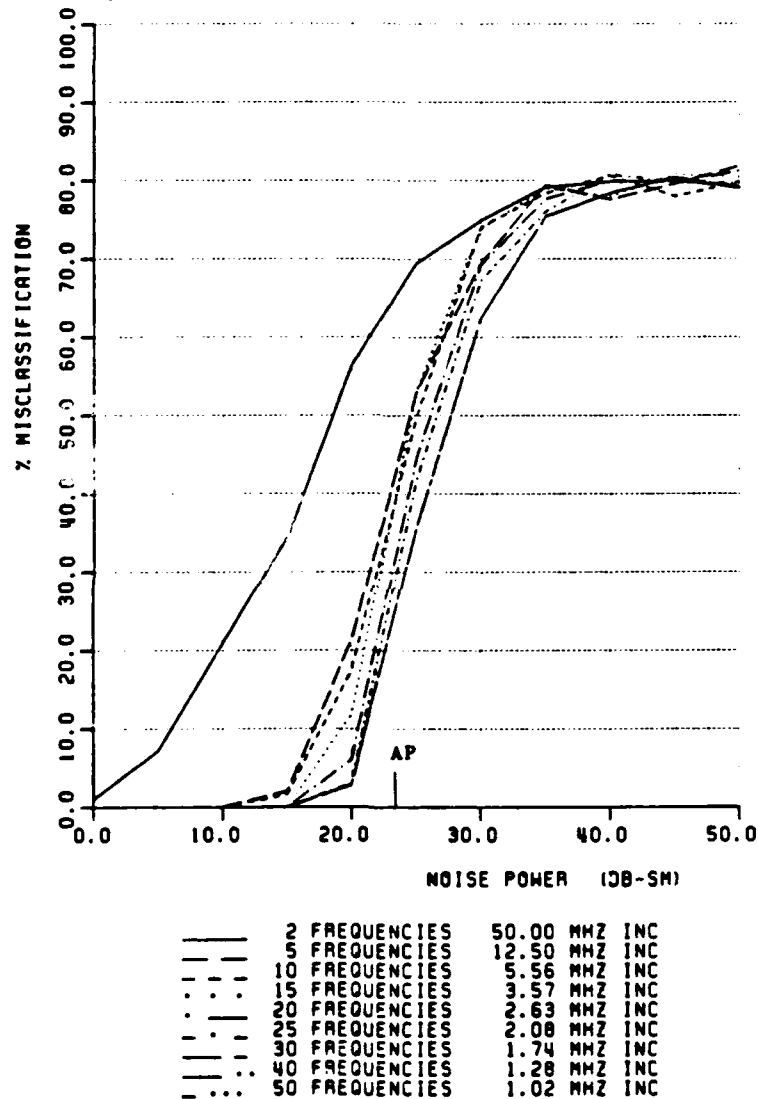90 % CONFIDENCE INTERVAL: 2.2%

	2 FREQUENCIES	30.00 MHZ INC
	5 FREQUENCIES	7.50 MHZ INC
	10 FREQUENCIES	0.33 MHZ INC
	15 FREQUENCIES	2.14 MHZ INC
	20 FREQUENCIES	1.58 MHZ INC
	25 FREQUENCIES	1.25 MHZ INC
	30 FREQUENCIES	1.03 MHZ INC

Figure 27: Number of Frequency Study for the 8-38 MHz Bandwidth

79

DATA BASE TYPE: AIRCRAFT
FEATURE VECTOR TYPE: MM
ALGORITHM TYPE: NON-COHERENT NN
AZIMUTH: 0   ELEVATION: 0   ROLL: 0
START FREQUENCY: 30 MHZ   STOP FREQUENCY: 60 MHZ
NUMBER OF FREQUENCIES: KEY
CATALOG SET VECTORS: 5   TEST SET VECTORS: 5
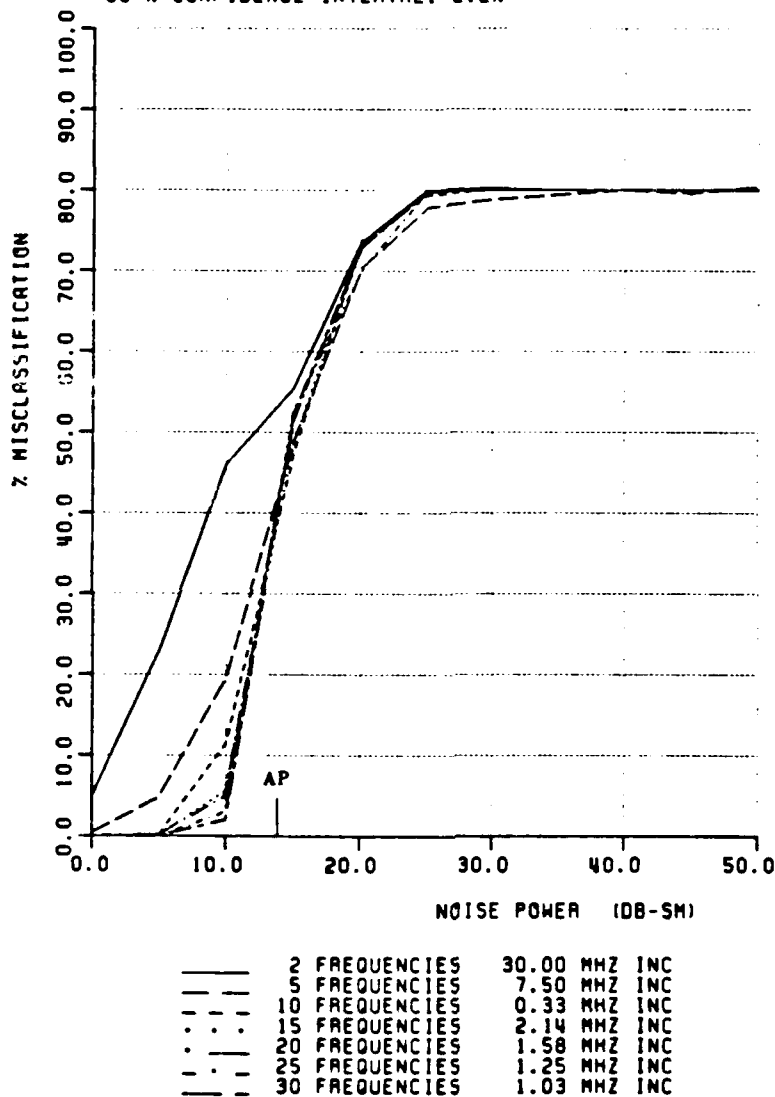NUMBER OF EXPERIMENTS: 100
90 % CONFIDENCE INTERVAL: 2.2%

	2 FREQUENCIES	30.00 MHZ INC
	5 FREQUENCIES	7.50 MHZ INC
	10 FREQUENCIES	0.33 MHZ INC
	15 FREQUENCIES	2.14 MHZ INC
	20 FREQUENCIES	1.58 MHZ INC
	25 FREQUENCIES	1.25 MHZ INC
	30 FREQUENCIES	1.03 MHZ INC

Figure 28: Number of Frequency Study for the 30-60 MHz Bandwidth

80

Figure 29: Number of Frequency Study for the 8-58 MHz Bandwidth

81

DATA BASE TYPE: AIRCRAFT
FEATURE VECTOR TYPE: HH
ALGORITHM TYPE: NON-COHERENT NN
AZIMUTH: 0   ELEVATION: 0   ROLL: 0
START FREQUENCY: 140MHZ   STOP FREQUENCY: 170MHZ
NUMBER OF FREQUENCIES: KEY
CATALOG SET VECTORS: 5   TEST SET VECTORS: 5
NUMBER OF EXPERIMENTS: 100
90 % CONFIDENCE INTERVAL: 2.2%

	2 FREQUENCIES	30.00 MHZ INC
	5 FREQUENCIES	7.50 MHZ INC
	10 FREQUENCIES	0.33 MHZ INC
	15 FREQUENCIES	2.14 MHZ INC
	20 FREQUENCIES	1.58 MHZ INC
	25 FREQUENCIES	1.25 MHZ INC
	30 FREQUENCIES	1.03 MHZ INC

Figure 30: Number of Frequency Study for the 140-170 MHz Bandwidth

82
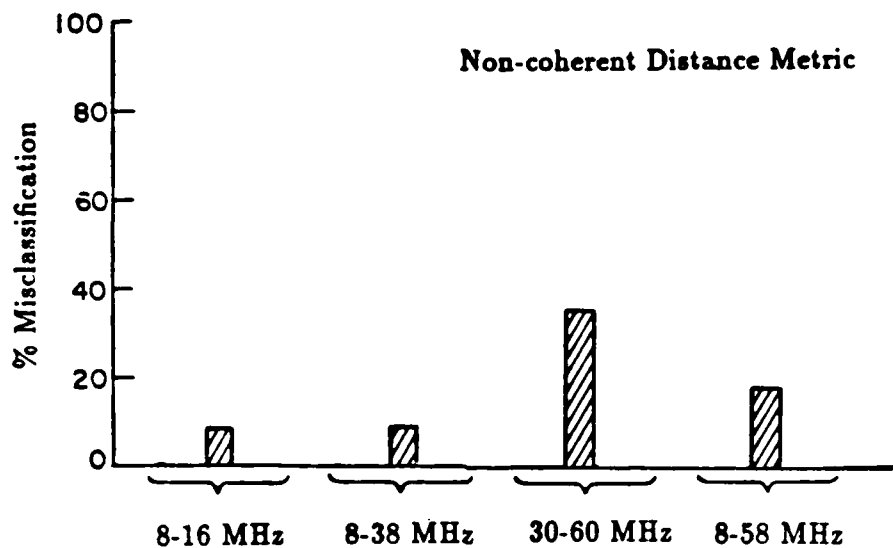
Figure 31: Bar Graph; $0°$ Aspect at 20 dBm^2 Noise Power
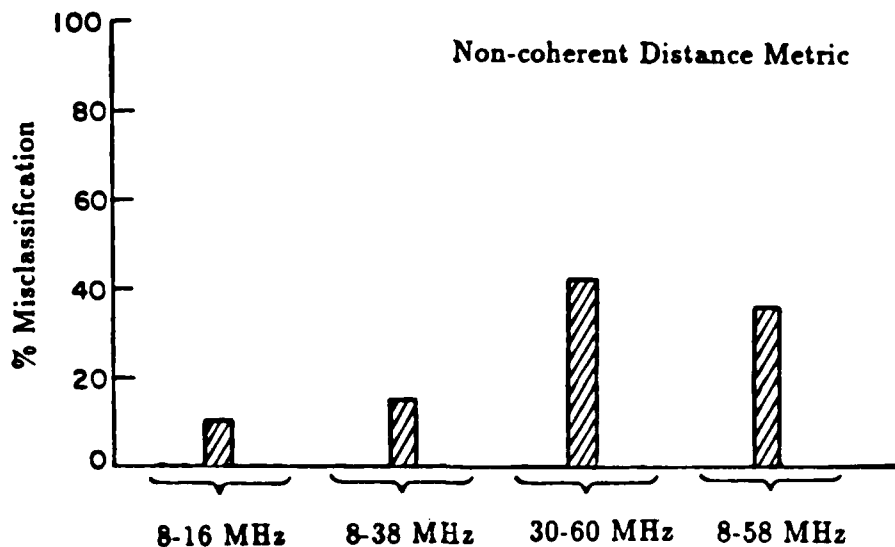
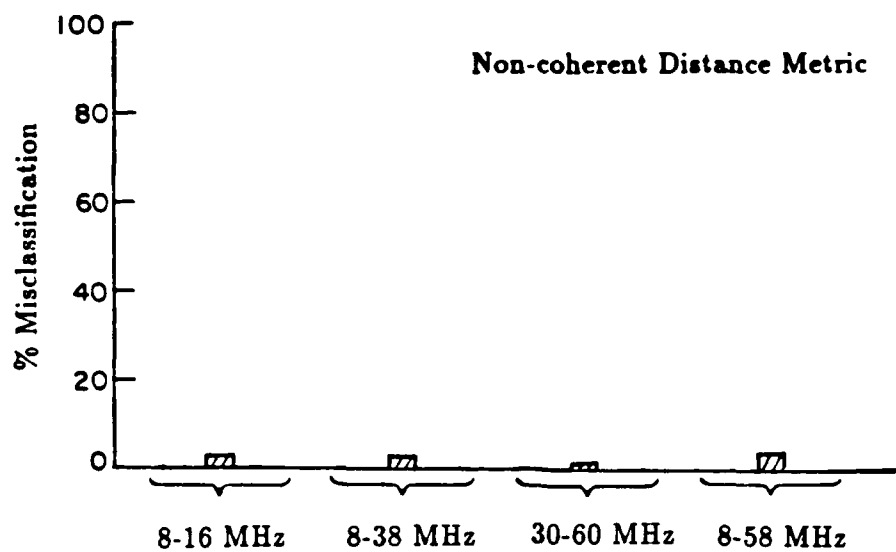Figure 32: Bar Graph; $45°$ Aspect at 20 dBm^2 Noise Power

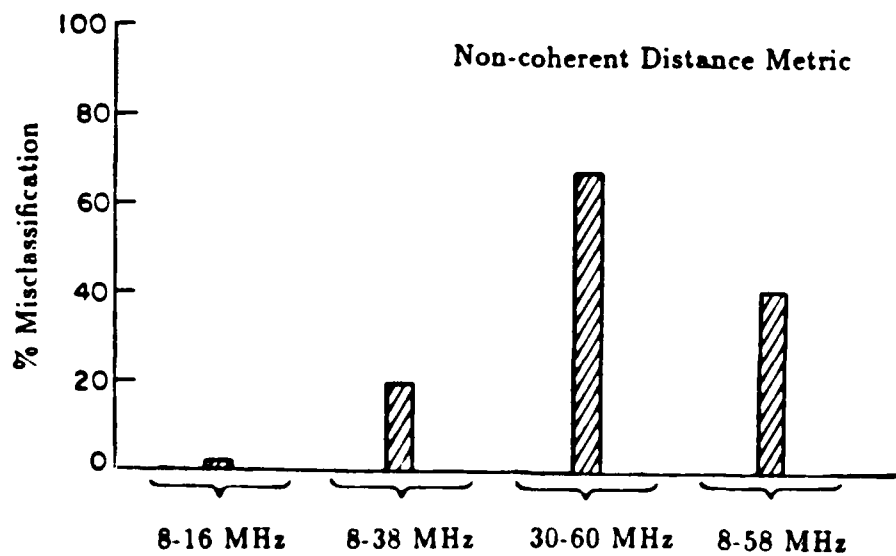Figure 33: Bar Graph; 90° Aspect at 20 dBm^2 Noise Power

Figure 34: Bar Graph; 180° Aspect at 20 dBm^2 Noise Power

87

DATA BASE TYPE: AIRCRAFT
FEATURE VECTOR TYPE: MM
ALGORITHM TYPE: KEY
AZIMUTH: 0   ELEVATION: 0   ROLL: 0
START FREQUENCY: 8 MHZ   STOP FREQUENCY: 16 MHZ
NUMBER OF FREQUENCIES: 2
CATALOG SET VECTORS: 5   TEST SET VECTORS: 5
NUMBER OF EXPERIMENTS: 100
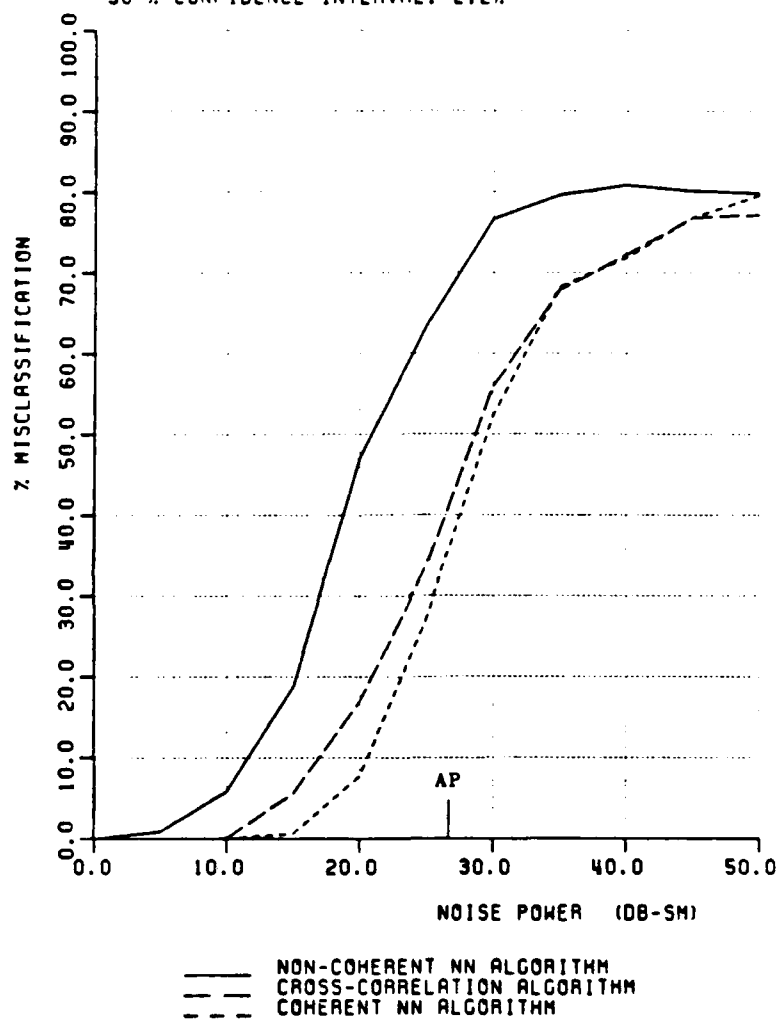90 % CONFIDENCE INTERVAL: 2.2%

NON-COHERENT NN ALGORITHM
CROSS-CORRELATION ALGORITHM
COHERENT NN ALGORITHM

Figure 35: Identification Algorithms: 8-16 MHz, 2 Frequencies

85
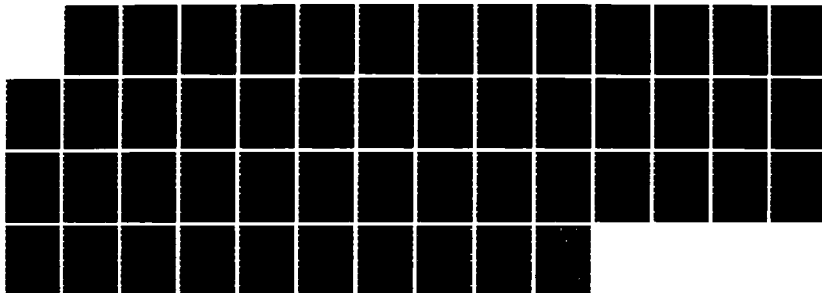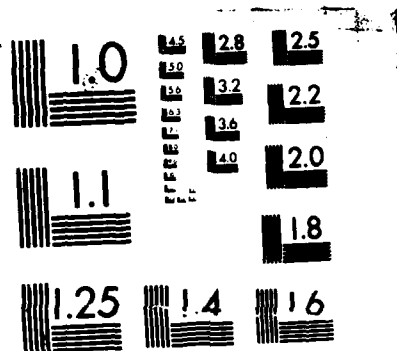
MICROCOPY RESOLUTION TEST CHART

NATIONAL BUREAU OF STANDARDS-1963-A

DATA BASE TYPE: AIRCRAFT
FEATURE VECTOR TYPE: HH
ALGORITHM TYPE: KEY
AZIMUTH: 0   ELEVATION: 0   ROLL: 0
START FREQUENCY: 8 MHZ   STOP FREQUENCY: 16 MHZ
NUMBER OF FREQUENCIES: 5
CATALOG SET VECTORS: 5   TEST SET VECTORS: 5
NUMBER OF EXPERIMENTS: 100
90 % CONFIDENCE INTERVAL: 2.2%

NON-COHERENT NN ALGORITHM
CROSS-CORRELATION ALGORITHM
COHERENT NN ALGORITHM

Figure 36: Identification Algorithms; 8-16 MHz, 5 Frequencies

86

DATA BASE TYPE: AIRCRAFT
FEATURE VECTOR TYPE: HH
ALGORITHM TYPE: KEY
AZIMUTH: 0   ELEVATION: 0   ROLL: 0
START FREQUENCY: 8 MHZ   STOP FREQUENCY: 16 MHZ
NUMBER OF FREQUENCIES: 10
CATALOG SET VECTORS: 5   TEST SET VECTORS: 5
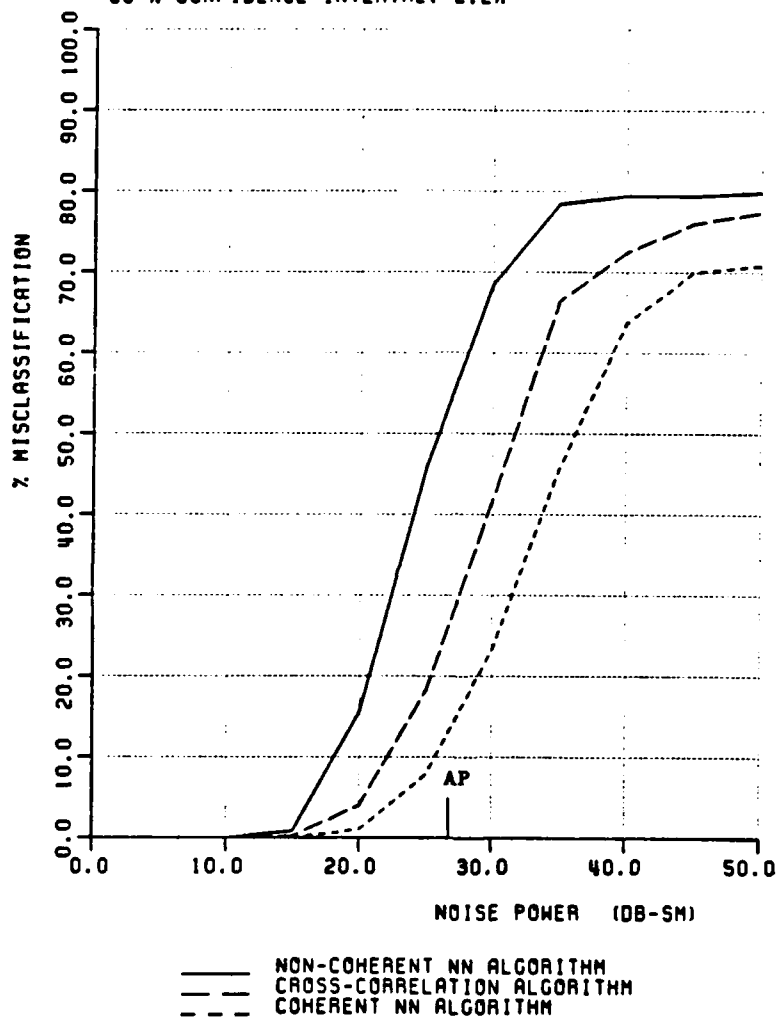NUMBER OF EXPERIMENTS: 100
90 % CONFIDENCE INTERVAL: 2.2%

NON-COHERENT NN ALGORITHM
CROSS-CORRELATION ALGORITHM
COHERENT NN ALGORITHM

Figure 37: Identification Algorithms; 8-16 MHz, 10 Frequencies

87

DATA BASE TYPE: AIRCRAFT
FEATURE VECTOR TYPE: HH
ALGORITHM TYPE: KEY
AZIMUTH: 0   ELEVATION: 0   ROLL: 0
START FREQUENCY: 8 MHZ   STOP FREQUENCY: 38 MHZ
NUMBER OF FREQUENCIES: 5
CATALOG SET VECTORS: 5   TEST SET VECTORS: 5
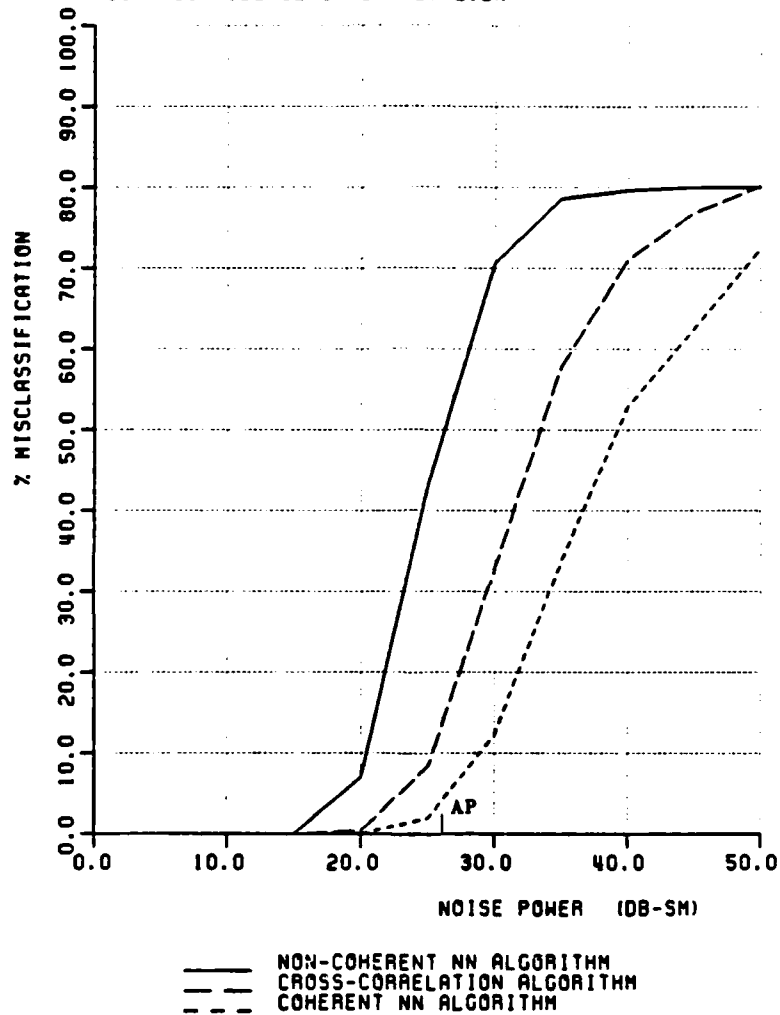NUMBER OF EXPERIMENTS: 100
90 % CONFIDENCE INTERVAL: 2.2%

Figure 38: Identification Algorithms; 8-38 MHz, 5 Frequencies

88

DATA BASE TYPE: AIRCRAFT
FEATURE VECTOR TYPE: MM
ALGORITHM TYPE: KEY
AZIMUTH: 0   ELEVATION: 0   ROLL: 0
START FREQUENCY: 8 MHZ   STOP FREQUENCY: 38 MHZ
NUMBER OF FREQUENCIES: 10
CATALOG SET VECTORS: 5   TEST SET VECTORS: 5
NUMBER OF EXPERIMENTS: 100
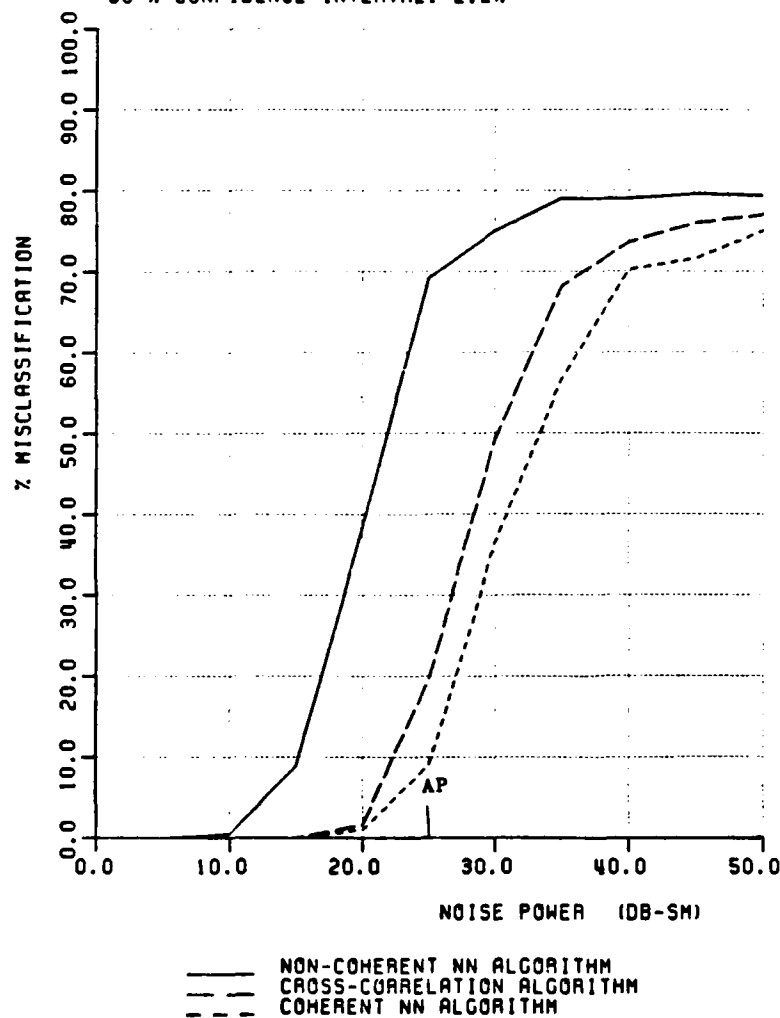90 % CONFIDENCE INTERVAL: 2.2%

NON-COHERENT NN ALGORITHM
CROSS-CORRELATION ALGORITHM
COHERENT NN ALGORITHM

Figure 39: Identification Algorithms; 8-38 MHz, 10 Frequencies

89

DATA BASE TYPE: AIRCRAFT
FEATURE VECTOR TYPE: MM
ALGORITHM TYPE: KEY
AZIMUTH: 0   ELEVATION: 0   ROLL: 0
START FREQUENCY: 8 MHZ   STOP FREQUENCY: 38 MHZ
NUMBER OF FREQUENCIES: 15
CATALOG SET VECTORS: 5   TEST SET VECTORS: 5
NUMBER OF EXPERIMENTS: 100
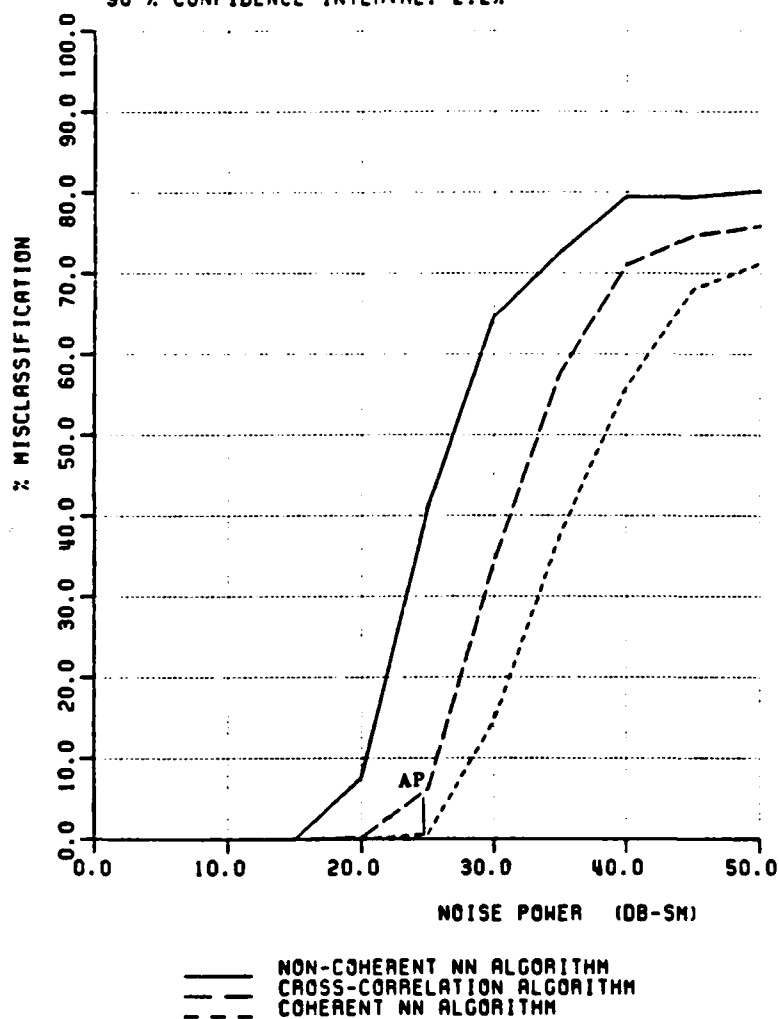90 % CONFIDENCE INTERVAL: 2.2%

NON-COHERENT NN ALGORITHM
CROSS-CORRELATION ALGORITHM
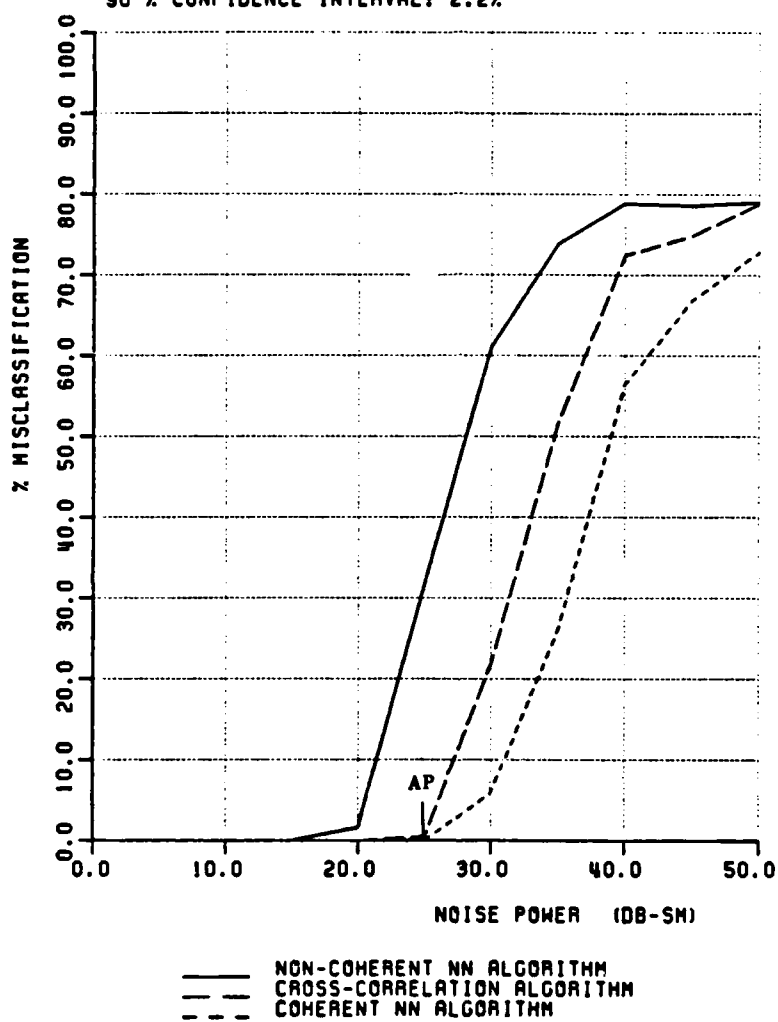COHERENT NN ALGORITHM

Figure 40: Identification Algorithms; 8-38 MHz, 15 Frequencies

90

DATA BASE TYPE: AIRCRAFT
FEATURE VECTOR TYPE: HH
ALGORITHM TYPE: COHERENT NN
AZIMUTH: KEY   ELEVATION: 0   ROLL: 0
START FREQUENCY: 8 MHZ   STOP FREQUENCY: 16 MHZ
NUMBER OF FREQUENCIES: 10
CATALOG SET VECTORS: 5   TEST SET VECTORS: 5
NUMBER OF EXPERIMENTS: 100
90 % CONFIDENCE INTERVAL: 2.2%

	0 DEG AZ	AVE POW = 26.3 DB-SM
	45 DEG AZ	AVE POW = 25.3 DB-SM
	90 DEG AZ	AVE POW = 31.2 DB-SM
	180 DEG AZ	AVE POW = 26.4 DB-SM

Figure 41: Feature Vector Type HH

91

DATA BASE TYPE: AIRCRAFT
FEATURE VECTOR TYPE: VV
ALGORITHM TYPE: COHERENT NN
AZIMUTH: KEY   ELEVATION: 0   ROLL: 0
START FREQUENCY: 8 MHZ   STOP FREQUENCY: 16 MHZ
NUMBER OF FREQUENCIES: 10
CATALOG SET VECTORS: 5   TEST SET VECTORS: 5
NUMBER OF EXPERIMENTS: 100
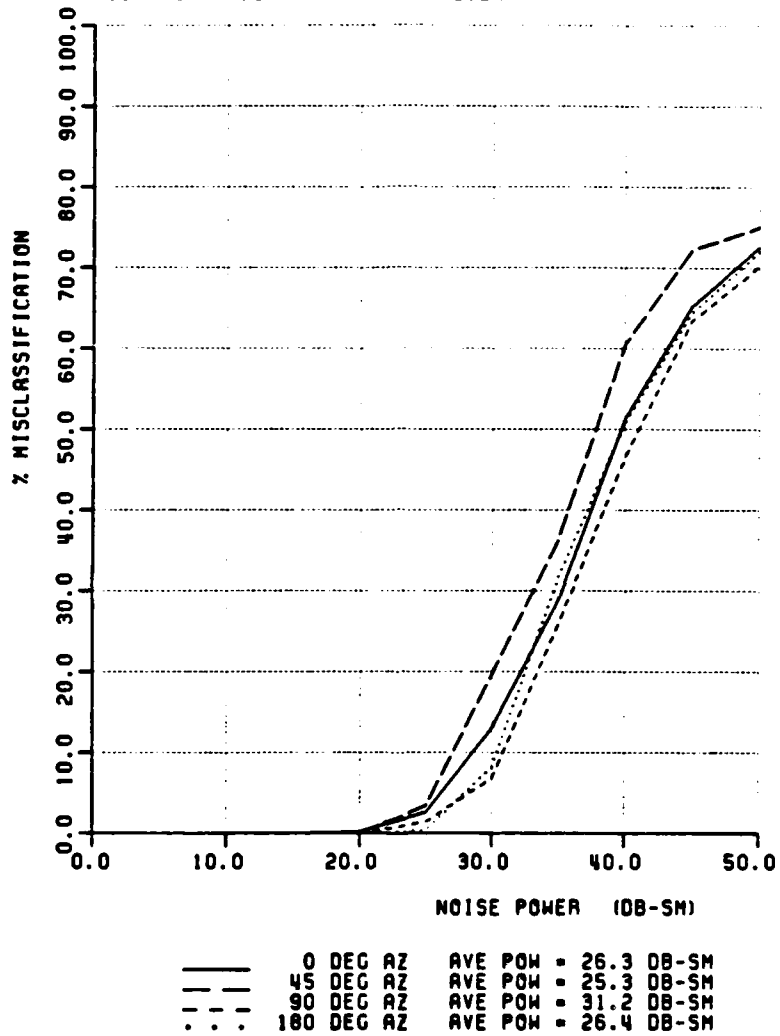90 % CONFIDENCE INTERVAL: 2.2%

NOISE POWER (DB-SM)

——	0 DEG AZ	AVE POW = 20.4 DB-SM
— —	45 DEG AZ	AVE POW = 19.3 DB-SM
– – –	90 DEG AZ	AVE POW = 30.6 DB-SM
. . .	180 DEG AZ	AVE POW = 18.6 DB-SM

Figure 42: Feature Vector Type VV

92

DATA BASE TYPE: AIRCRAFT
FEATURE VECTOR TYPE: VH
ALGORITHM TYPE: COHERENT NN
AZIMUTH: KEY   ELEVATION: 0   ROLL: 0
START FREQUENCY: 8 MHZ   STOP FREQUENCY: 16 MHZ
NUMBER OF FREQUENCIES: 10
CATALOG SET VECTORS: 5   TEST SET VECTORS: 5
NUMBER OF EXPERIMENTS: 100
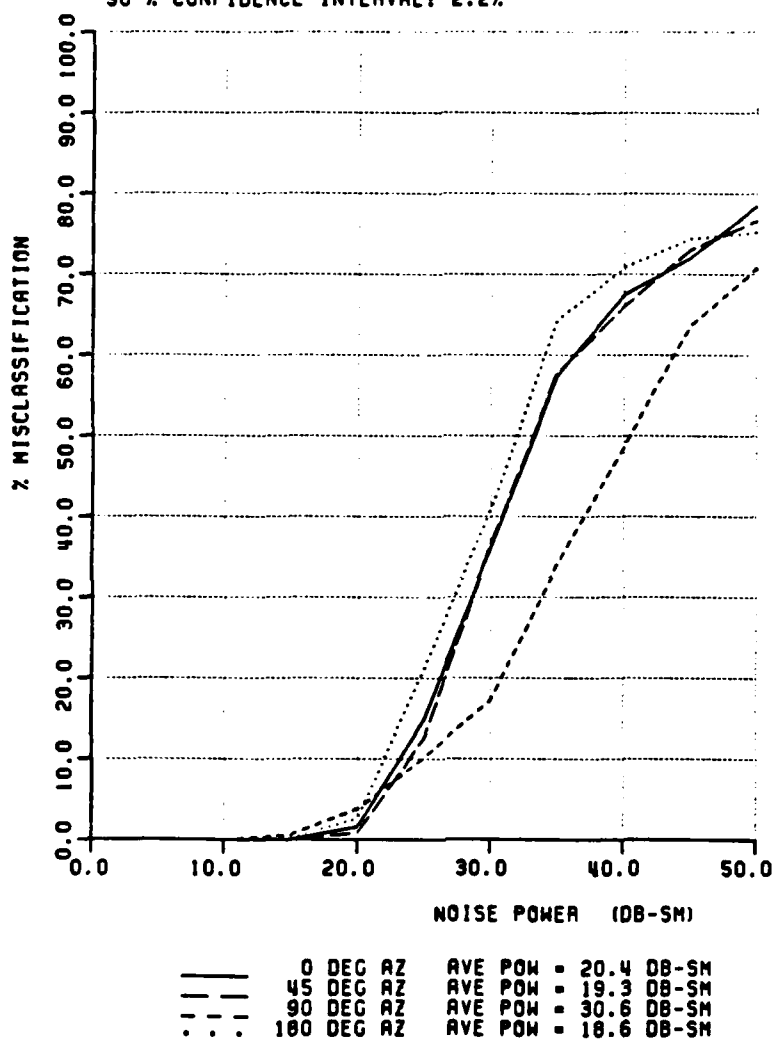90 % CONFIDENCE INTERVAL: 2.2%

	0 DEG AZ	AVE POW = 1.8 DB-SM
	45 DEG AZ	AVE POW = 17.2 DB-SM
	90 DEG AZ	AVE POW = 20.0 DB-SM
	180 DEG AZ	AVE POW = 3.5 DB-SM

Figure 43: Feature Vector Type VH

Figure 44: Feature Vector Type RR

94

DATA BASE TYPE: AIRCRAFT
FEATURE VECTOR TYPE: LL
ALGORITHM TYPE: COHERENT NN
AZIMUTH: KEY   ELEVATION: 0   ROLL: 0
START FREQUENCY: 8 MHZ   STOP FREQUENCY: 16 MHZ
NUMBER OF FREQUENCIES: 10
CATALOG SET VECTORS: 5   TEST SET VECTORS: 5
NUMBER OF EXPERIMENTS: 100
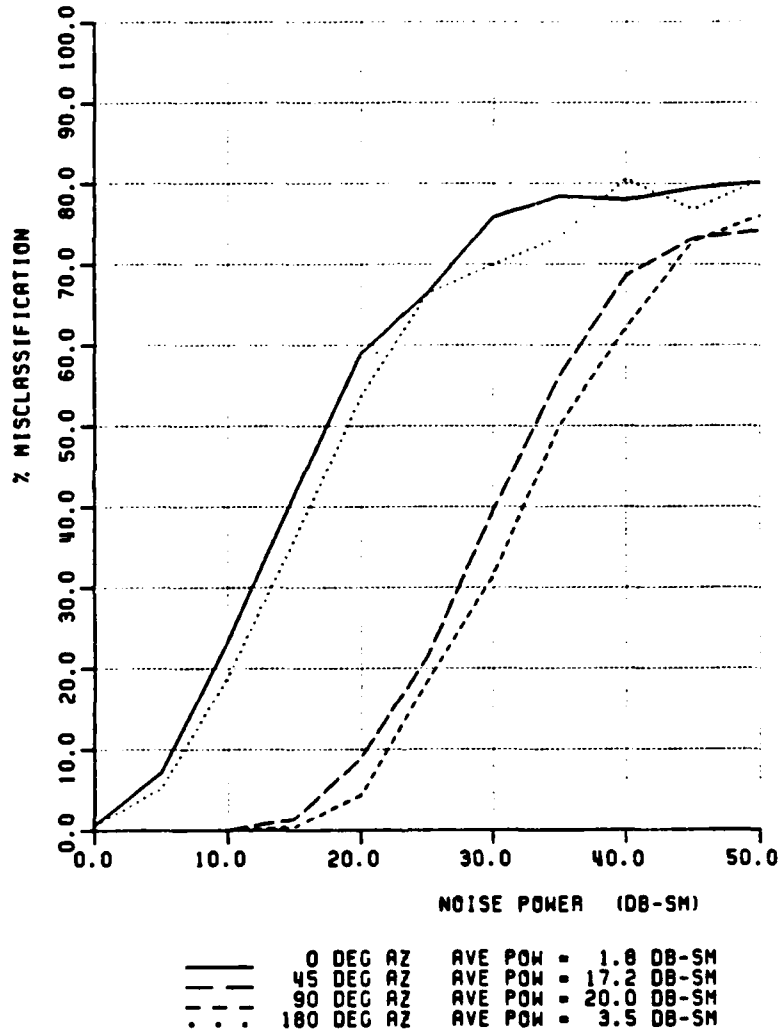90 % CONFIDENCE INTERVAL: 2.2%

———   0 DEG AZ   AVE POW = 21.7 DB-SM
— —   45 DEG AZ   AVE POW = 23.3 DB-SM
— — —   90 DEG AZ   AVE POW = 25.4 DB-SM
· · ·   180 DEG AZ   AVE POW = 20.6 DB-SM

Figure 45: Feature Vector Type LL

95

DATA BASE TYPE: AIRCRAFT
FEATURE VECTOR TYPE: RL
ALGORITHM TYPE: COHERENT NN
AZIMUTH: KEY   ELEVATION: 0   ROLL: 0
START FREQUENCY: 8 MHZ   STOP FREQUENCY: 16 MHZ
NUMBER OF FREQUENCIES: 10
CATALOG SET VECTORS: 5   TEST SET VECTORS: 5
NUMBER OF EXPERIMENTS: 100
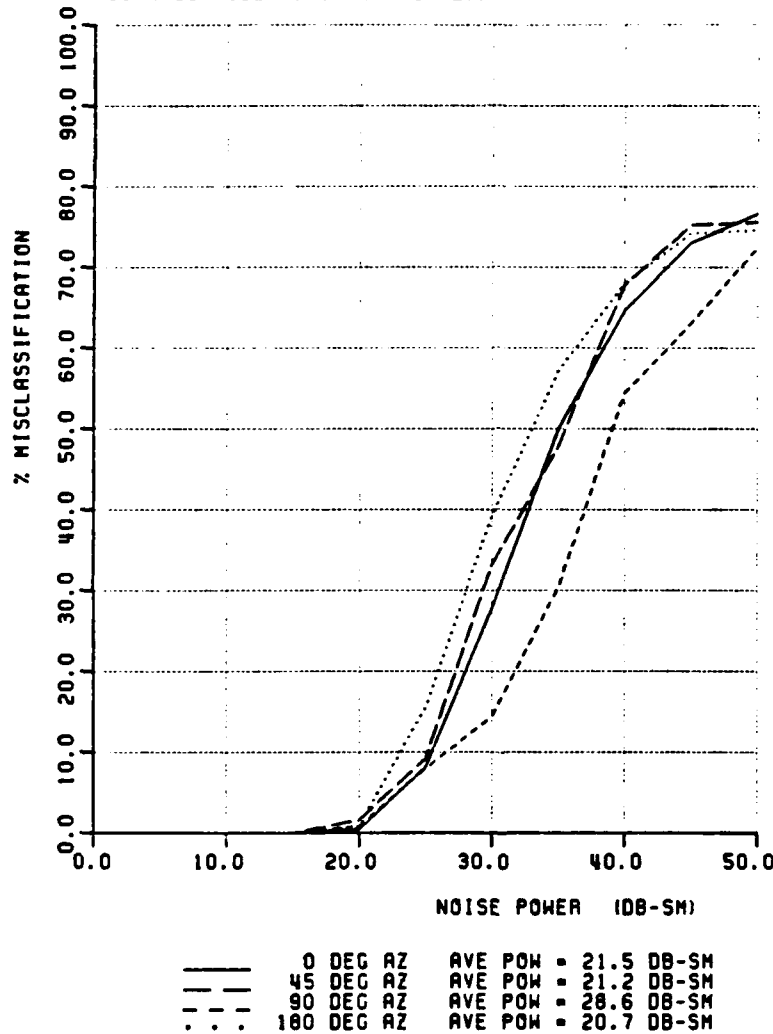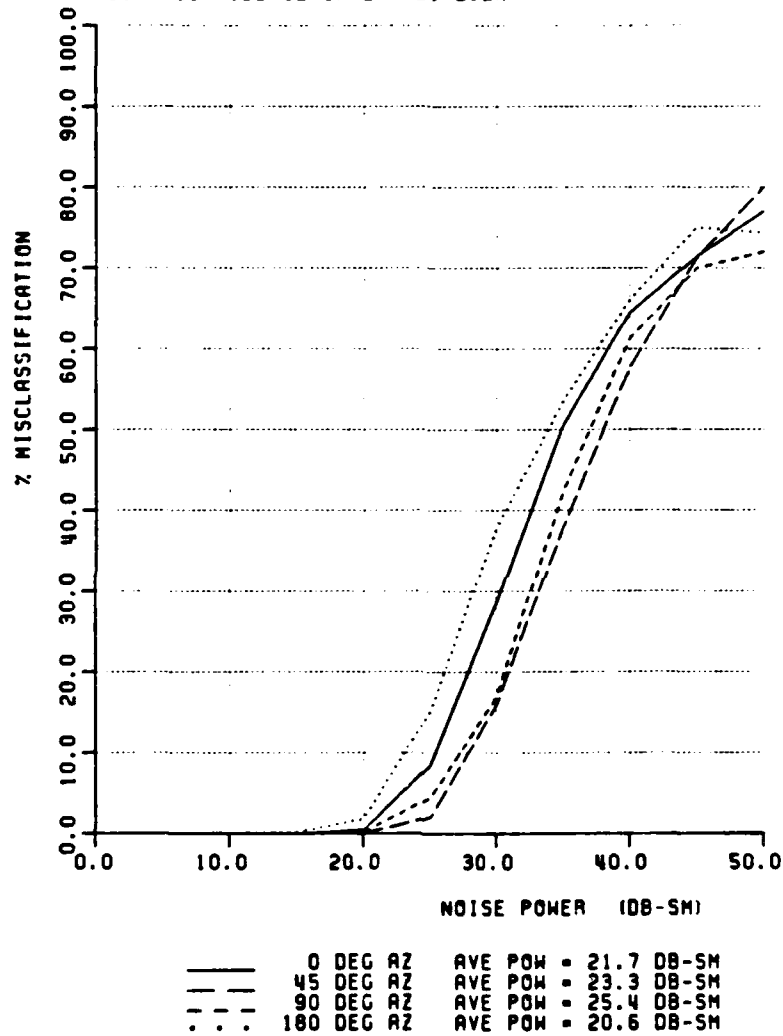90 % CONFIDENCE INTERVAL: 2.2%

0 DEG AZ	AVE POW = 21.1 DB-SM
45 DEG AZ	AVE POW = 20.7 DB-SM
90 DEG AZ	AVE POW = 29.2 DB-SM
180 DEG AZ	AVE POW = 21.8 DB-SM
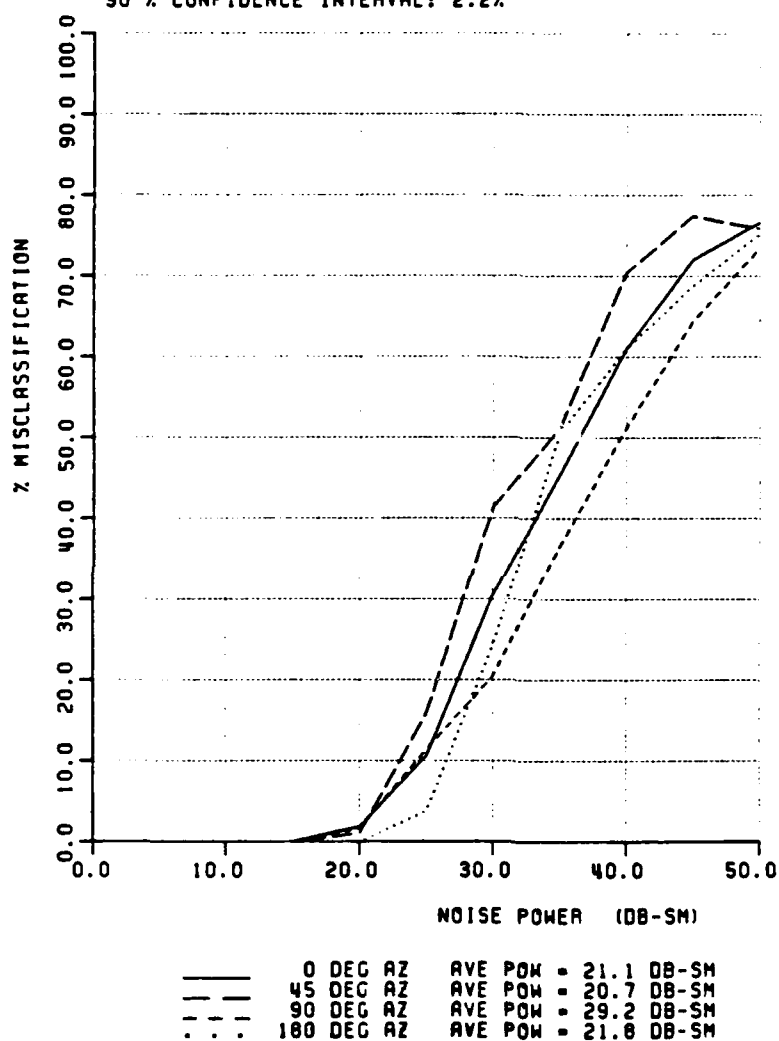
Figure 46: Feature Vector Type RL

96

DATA BASE TYPE: AIRCRAFT
FEATURE VECTOR TYPE: HH/VV
ALGORITHM TYPE: COHERENT NN
AZIMUTH: KEY   ELEVATION: 0   ROLL: 0
START FREQUENCY: 8 MHZ   STOP FREQUENCY: 16 MHZ
NUMBER OF FREQUENCIES: 10
CATALOG SET VECTORS: 5   TEST SET VECTORS: 5
NUMBER OF EXPERIMENTS: 100
90 % CONFIDENCE INTERVAL: 2.2%

% MISCLASSIFICATION

NOISE POWER   (DB-SM)

```
_____      0 DEG AZ    AVE POW = 24.5 DB-SM
_ _ _       45 DEG AZ    AVE POW = 23.6 DB-SM
_ _ _       90 DEG AZ    AVE POW = 31.2 DB-SM
. . .      180 DEG AZ    AVE POW = 24.3 DB-SM
```

Figure 47: Feature Vector Type HH/VV

97

DATA BASE TYPE: AIRCRAFT
FEATURE VECTOR TYPE: HH/VH
ALGORITHM TYPE: COHERENT NN
AZIMUTH: KEY   ELEVATION: 0   ROLL: 0
START FREQUENCY: 8 MHZ   STOP FREQUENCY: 16 MHZ
NUMBER OF FREQUENCIES: 10
CATALOG SET VECTORS: 5   TEST SET VECTORS: 5
NUMBER OF EXPERIMENTS: 100
90 % CONFIDENCE INTERVAL: 2.2%

Figure 48: Feature Vector Type HH/VH

98

NOISE POWER (DB-SM)

——	0 DEG AZ	AVE POW = 24.5 DB-SM
– –	45 DEG AZ	AVE POW = 23.6 DB-SM
– – –	90 DEG AZ	AVE POW = 31.2 DB-SM
. . .	180 DEG AZ	AVE POW = 24.3 DB-SM

Figure 49: Feature Vector Type VV/HH

99

DATA BASE TYPE: AIRCRAFT
FEATURE VECTOR TYPE: VV/VH
ALGORITHM TYPE: COHERENT NN
AZIMUTH: KEY   ELEVATION: 0   ROLL: 0
START FREQUENCY: 8 MHZ   STOP FREQUENCY: 16 MHZ
NUMBER OF FREQUENCIES: 10
CATALOG SET VECTORS: 5   TEST SET VECTORS: 5
NUMBER OF EXPERIMENTS: 100
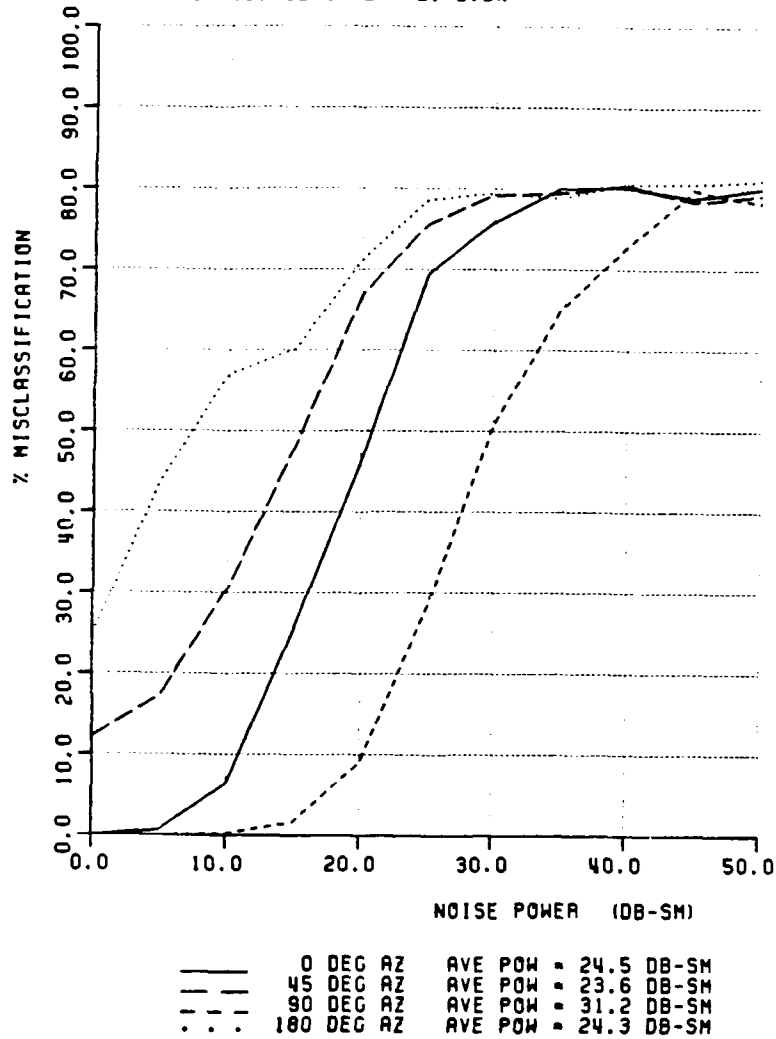90 % CONFIDENCE INTERVAL: 2.2%

——	0 DEG AZ	AVE POW = 17.5 DB-SM
— —	45 DEG AZ	AVE POW = 19.8 DB-SM
— · —	90 DEG AZ	AVE POW = 28.2 DB-SM
· · ·	180 DEG AZ	AVE POW = 15.9 DB-SM

Figure 50: Feature Vector Type VV/VH

100

DATA BASE TYPE: AIRCRAFT
FEATURE VECTOR TYPE: VH/HH
ALGORITHM TYPE: COHERENT NN
AZIMUTH: KEY   ELEVATION: 0   ROLL: 0
START FREQUENCY: 8 MHZ   STOP FREQUENCY: 16 MHZ
NUMBER OF FREQUENCIES: 10
CATALOG SET VECTORS: 5   TEST SET VECTORS: 5
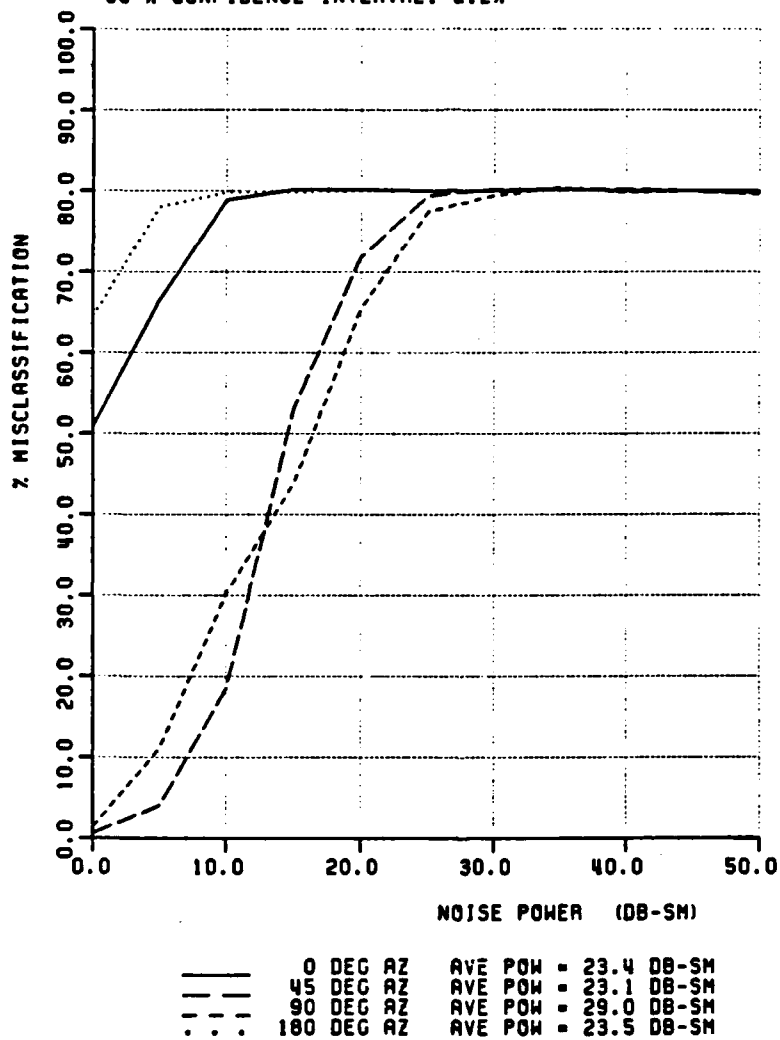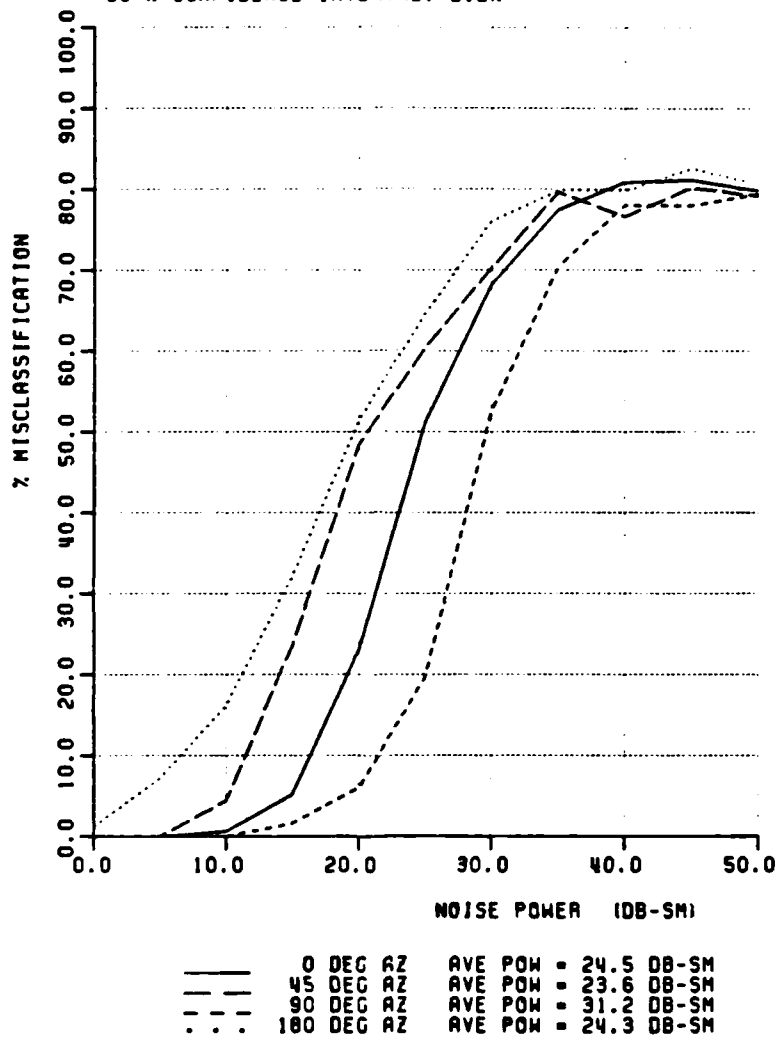NUMBER OF EXPERIMENTS: 100
90 % CONFIDENCE INTERVAL: 2.2%

NOISE POWER   (DB-SM)

———	0 DEG AZ	AVE POW = 23.4 DB-SM
— —	45 DEG AZ	AVE POW = 23.1 DB-SM
– – –	90 DEG AZ	AVE POW = 29.0 DB-SM
. . .	180 DEG AZ	AVE POW = 23.5 DB-SM

Figure 51: Feature Vector Type VH/HH

101

DATA BASE TYPE: AIRCRAFT
FEATURE VECTOR TYPE: VH/VV
ALGORITHM TYPE: COHERENT NN
AZIMUTH: KEY   ELEVATION: 0   ROLL: 0
START FREQUENCY: 8 MHZ   STOP FREQUENCY: 16 MHZ
NUMBER OF FREQUENCIES: 10
CATALOG SET VECTORS: 5   TEST SET VECTORS: 5
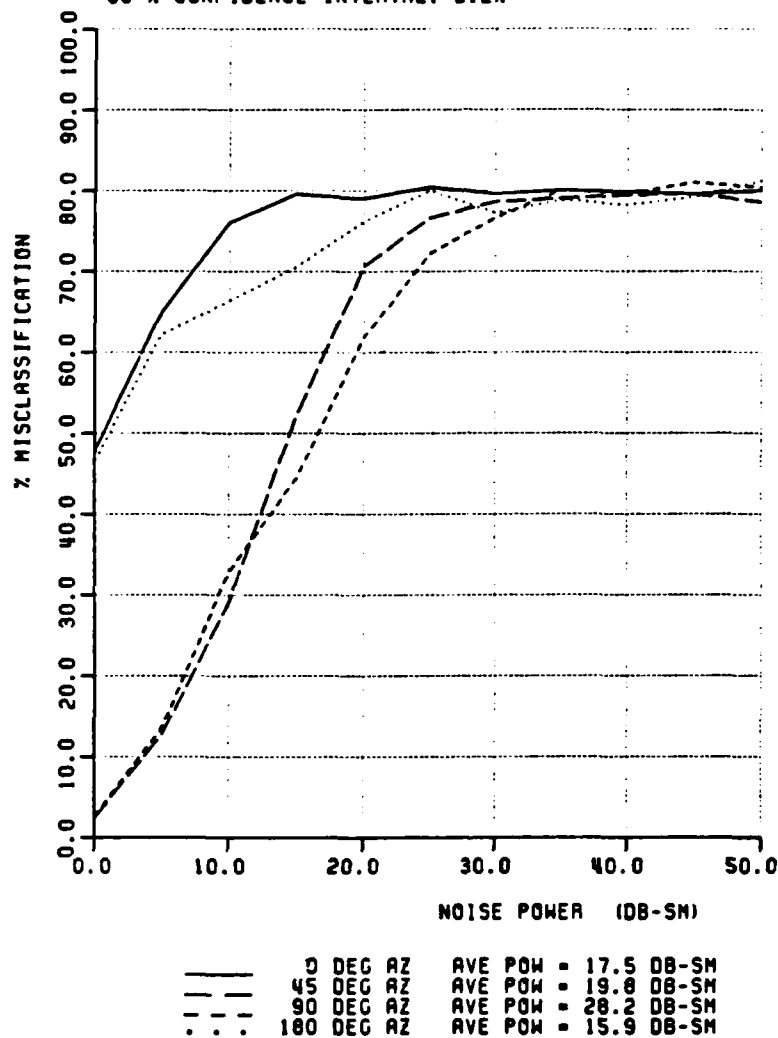NUMBER OF EXPERIMENTS: 100
90 % CONFIDENCE INTERVAL: 2.2%

	0 DEG AZ	AVE POW = 17.5 DB-SM
	45 DEG AZ	AVE POW = 19.8 DB-SM
	90 DEG AZ	AVE POW = 28.2 DB-SM
	180 DEG AZ	AVE POW = 15.9 DB-SM

Figure 52: Feature Vector Type VH/VV

102

DATA BASE TYPE: AIRCRAFT
FEATURE VECTOR TYPE: RR/LL
ALGORITHM TYPE: COHERENT NN
AZIMUTH: KEY   ELEVATION: 0   ROLL: 0
START FREQUENCY: 8 MHZ   STOP FREQUENCY: 16 MHZ
NUMBER OF FREQUENCIES: 10
CATALOG SET VECTORS: 5   TEST SET VECTORS: 5
NUMBER OF EXPERIMENTS: 100
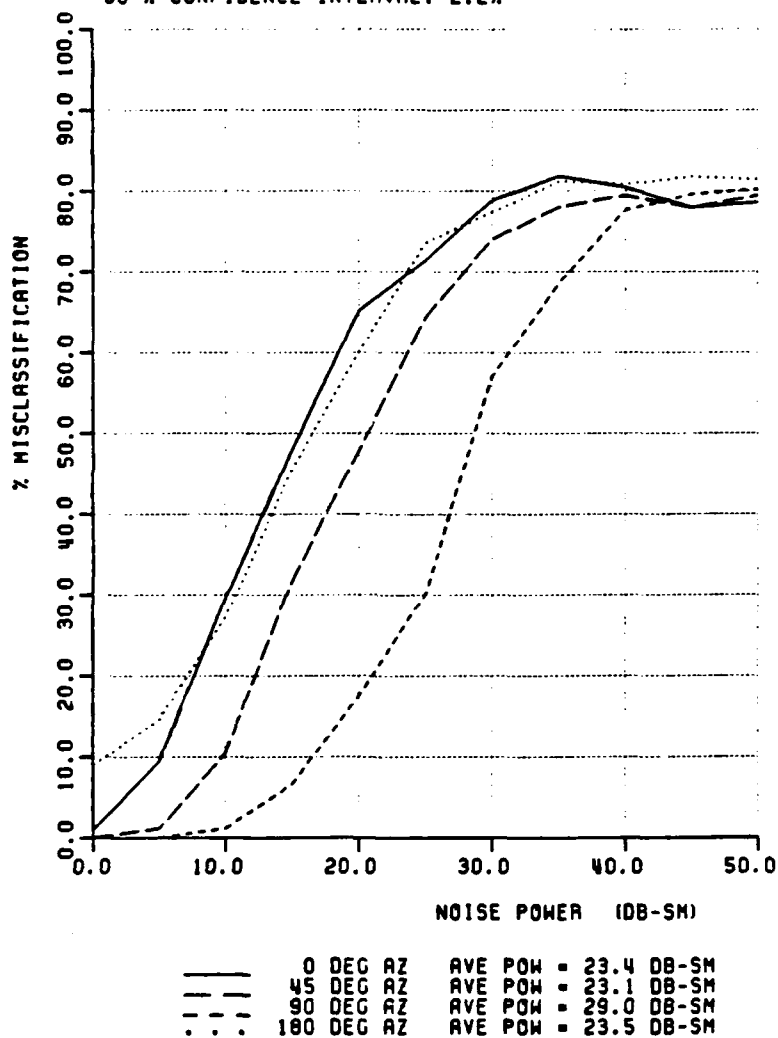90 % CONFIDENCE INTERVAL: 2.2%

NOISE POWER (DB-SM)

	0 DEG AZ	AVE POW = 21.6 DB-SM
	45 DEG AZ	AVE POW = 22.5 DB-SM
	90 DEG AZ	AVE POW = 27.3 DB-SM
	180 DEG AZ	AVE POW = 20.7 DB-SM

Figure 53: Feature Vector Type RR/LL

103

DATA BASE TYPE: AIRCRAFT
FEATURE VECTOR TYPE: RR/RL
ALGORITHM TYPE: COHERENT NN
AZIMUTH: KEY   ELEVATION: 0   ROLL: 0
START FREQUENCY: 8 MHZ   STOP FREQUENCY: 16 MHZ
NUMBER OF FREQUENCIES: 10
CATALOG SET VECTORS: 5   TEST SET VECTORS: 5
NUMBER OF EXPERIMENTS: 100
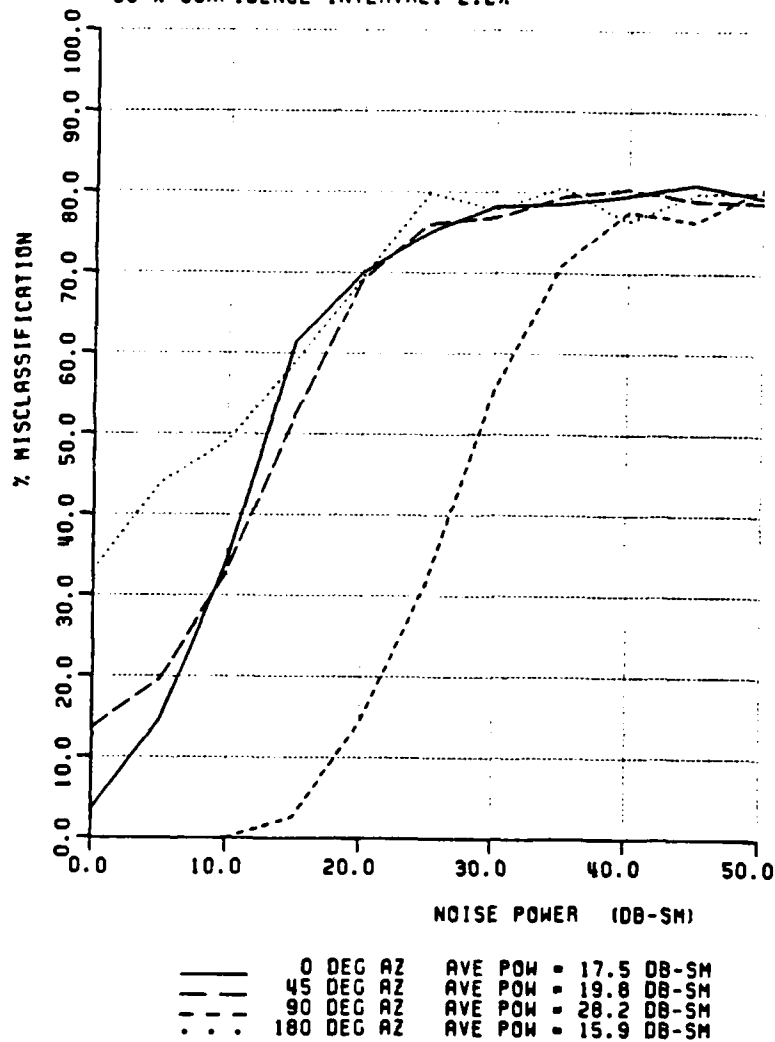90 % CONFIDENCE INTERVAL: 2.2%

NOISE POWER (DB-SM)

———	0 DEG AZ	AVE POW = 21.6 DB-SM
— —	45 DEG AZ	AVE POW = 21.1 DB-SM
– – –	90 DEG AZ	AVE POW = 29.4 DB-SM
. . .	180 DEG AZ	AVE POW = 21.4 DB-SM

Figure 54: Feature Vector Type RR/RL

104

DATA BASE TYPE: AIRCRAFT
FEATURE VECTOR TYPE: LL/RR
ALGORITHM TYPE: COHERENT NN
AZIMUTH: KEY   ELEVATION: 0   ROLL: 0
START FREQUENCY: 8 MHZ   STOP FREQUENCY: 16 MHZ
NUMBER OF FREQUENCIES: 10
CATALOG SET VECTORS: 5   TEST SET VECTORS: 5
NUMBER OF EXPERIMENTS: 100
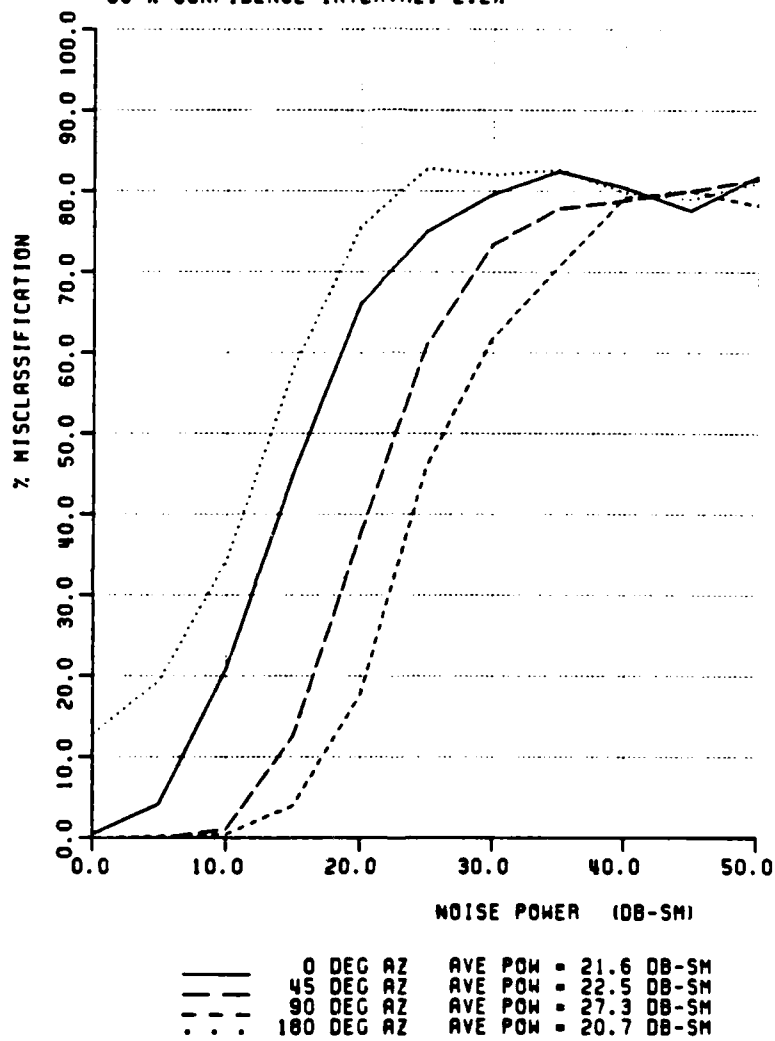90 % CONFIDENCE INTERVAL: 2.2%

	0 DEG AZ	AVE POW = 21.6 DB-SM
	45 DEG AZ	AVE POW = 22.5 DB-SM
	90 DEG AZ	AVE POW = 27.3 DB-SM
	180 DEG AZ	AVE POW = 20.7 DB-SM

Figure 55: Feature Vector Type LL/RR

105

DATA BASE TYPE: AIRCRAFT
FEATURE VECTOR TYPE: LL/RL
ALGORITHM TYPE: COHERENT NN
AZIMUTH: KEY   ELEVATION: 0   ROLL: 0
START FREQUENCY: 8 MHZ   STOP FREQUENCY: 16 MHZ
NUMBER OF FREQUENCIES: 10
CATALOG SET VECTORS: 5   TEST SET VECTORS: 5
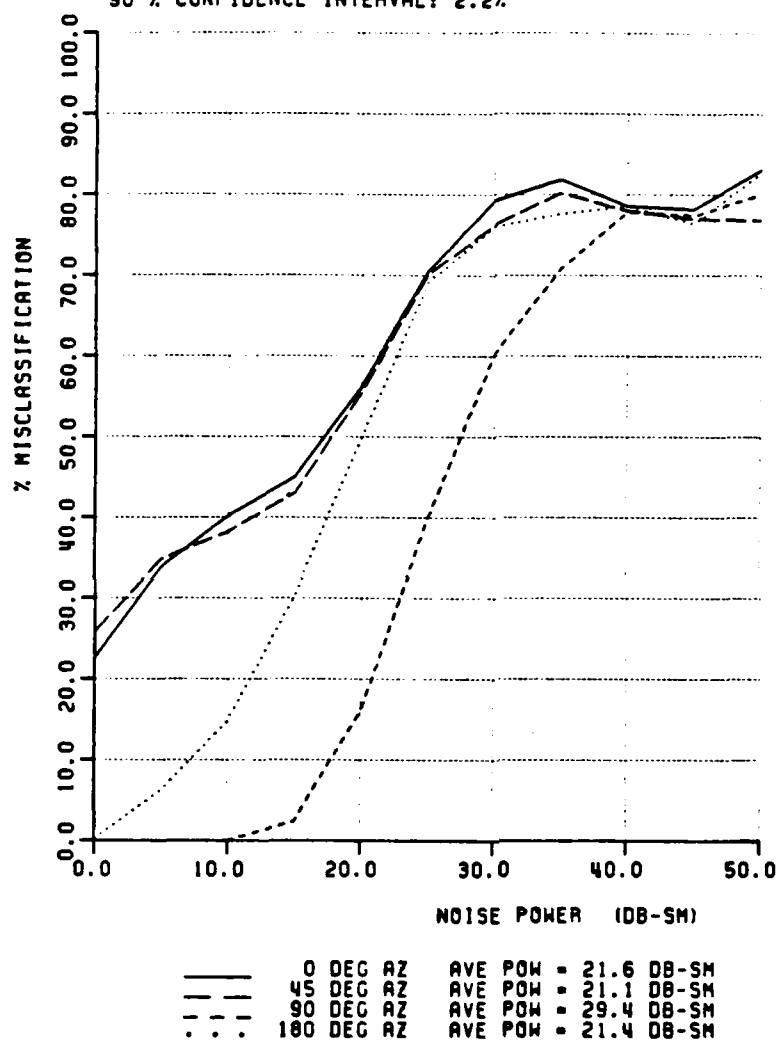NUMBER OF EXPERIMENTS: 100
90 % CONFIDENCE INTERVAL: 2.2%

Y axis: % MISCLASSIFICATION (0.0 to 100.0)
X axis: NOISE POWER (DB-SM) (0.0 to 50.0)

		AVE POW	
———	0 DEG AZ	AVE POW = 21.7 DB-SM
— —	45 DEG AZ	AVE POW = 22.5 DB-SM
– – –	90 DEG AZ	AVE POW = 28.1 DB-SM
· · ·	180 DEG AZ	AVE POW = 21.4 DB-SM

Figure 56: Feature Vector Type LL/RL

106

DATA BASE TYPE: AIRCRAFT
FEATURE VECTOR TYPE: RL/RR
ALGORITHM TYPE: COHERENT NN
AZIMUTH: KEY   ELEVATION: 0   ROLL: 0
START FREQUENCY: 8 MHZ   STOP FREQUENCY: 16 MHZ
NUMBER OF FREQUENCIES: 10
CATALOG SET VECTORS: 5   TEST SET VECTORS: 5
NUMBER OF EXPERIMENTS: 100
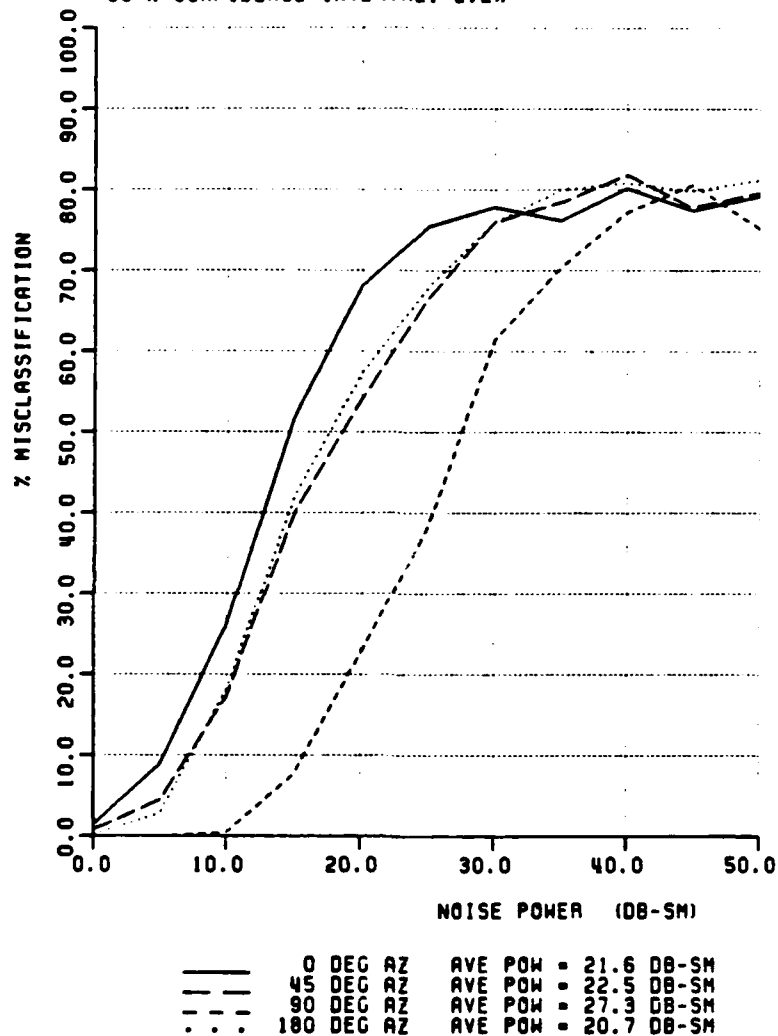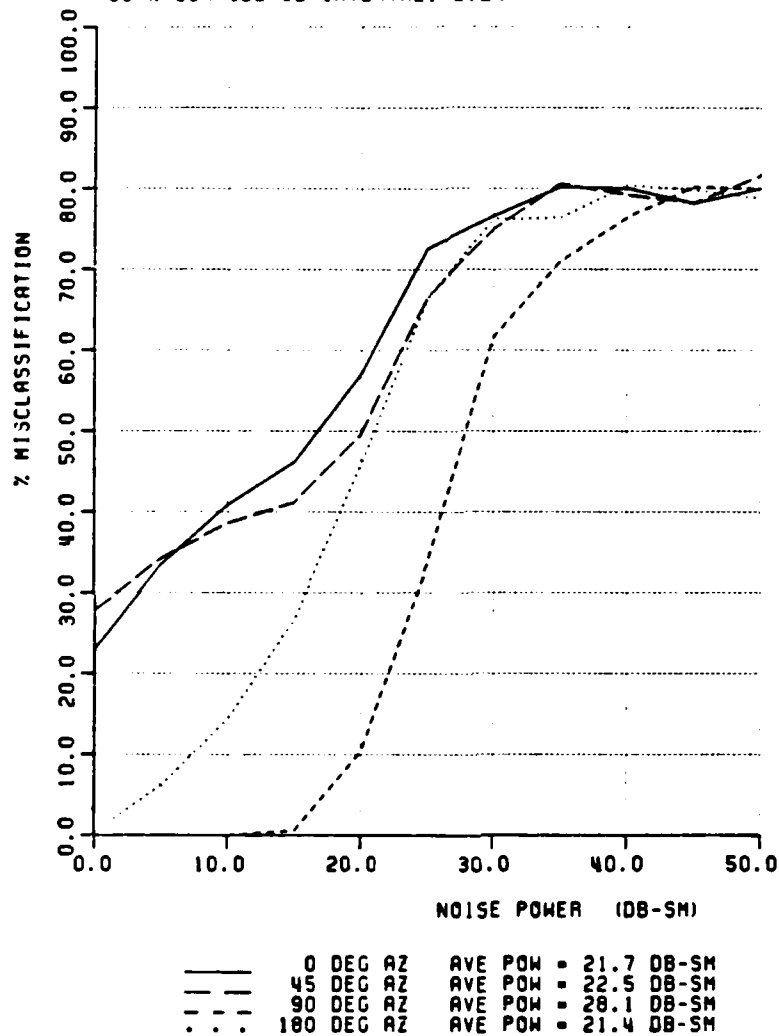90 % CONFIDENCE INTERVAL: 2.2%

	0 DEG AZ	AVE POW = 21.6 DB-SM
	45 DEG AZ	AVE POW = 21.1 DB-SM
	90 DEG AZ	AVE POW = 29.4 DB-SM
	180 DEG AZ	AVE POW = 21.4 DB-SM

Figure 57: Feature Vector Type RL/RR

107

DATA BASE TYPE: AIRCRAFT
FEATURE VECTOR TYPE: RL/LL
ALGORITHM TYPE: COHERENT NN
AZIMUTH: KEY   ELEVATION: 0   ROLL: 0
START FREQUENCY: 8 MHZ   STOP FREQUENCY: 16 MHZ
NUMBER OF FREQUENCIES: 10
CATALOG SET VECTORS: 5   TEST SET VECTORS: 5
NUMBER OF EXPERIMENTS: 100
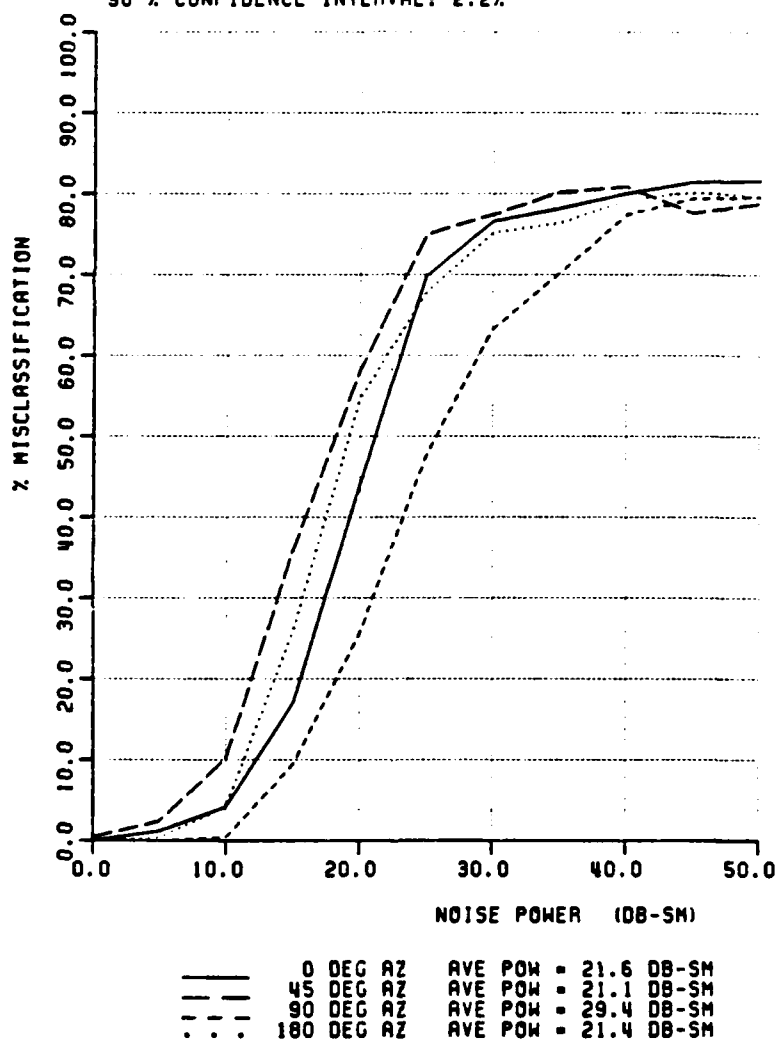90 % CONFIDENCE INTERVAL: 2.2%

Figure 58: Feature Vector Type RL/LL

108

DATA BASE TYPE: AIRCRAFT
FEATURE VECTOR TYPE: AGILE
ALGORITHM TYPE: COHERENT NN
AZIMUTH: KEY   ELEVATION: 0   ROLL: 0
START FREQUENCY: 8 MHZ   STOP FREQUENCY: 16 MHZ
NUMBER OF FREQUENCIES: 10
CATALOG SET VECTORS: 5   TEST SET VECTORS: 5
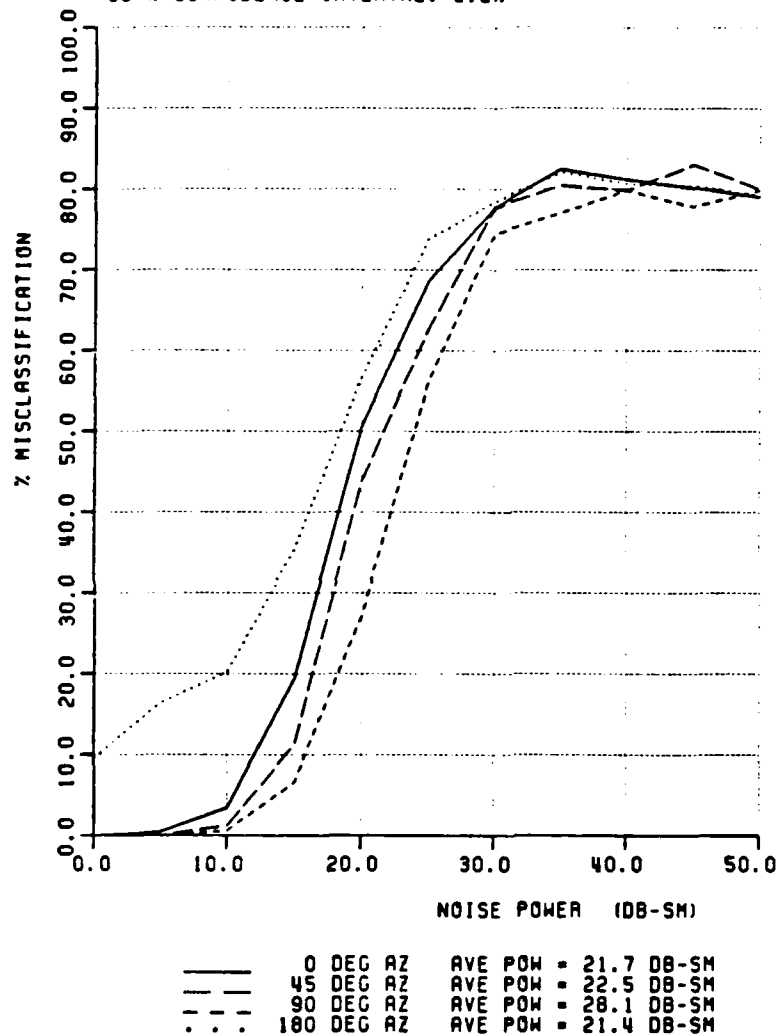NUMBER OF EXPERIMENTS: 100
90 % CONFIDENCE INTERVAL: 2.2%

——	0 DEG AZ	AVE POW =	21.7 DB-SM
— —	45 DEG AZ	AVE POW =	22.5 DB-SM
– – –	90 DEG AZ	AVE POW =	28.1 DB-SM
. . .	180 DEG AZ	AVE POW =	21.4 DB-SM

Figure 59: Feature Vector Type AGILE

109

Figure 60: Linear Polarization Diverse Feature Vector (CONCAT)

DATA BASE TYPE: AIRCRAFT
FEATURE VECTOR TYPE: CIRCULAR POL-DIVERSE (CONCAT)
ALGORITHM TYPE: COHERENT NN
AZIMUTH: KEY   ELEVATION: 0   ROLL: 0
START FREQUENCY: 8 MHZ   STOP FREQUENCY: 16 MHZ
NUMBER OF FREQUENCIES: 4
CATALOG SET VECTORS: 5   TEST SET VECTORS: 5
NUMBER OF EXPERIMENTS: 100
90 % CONFIDENCE INTERVAL: 2.2%
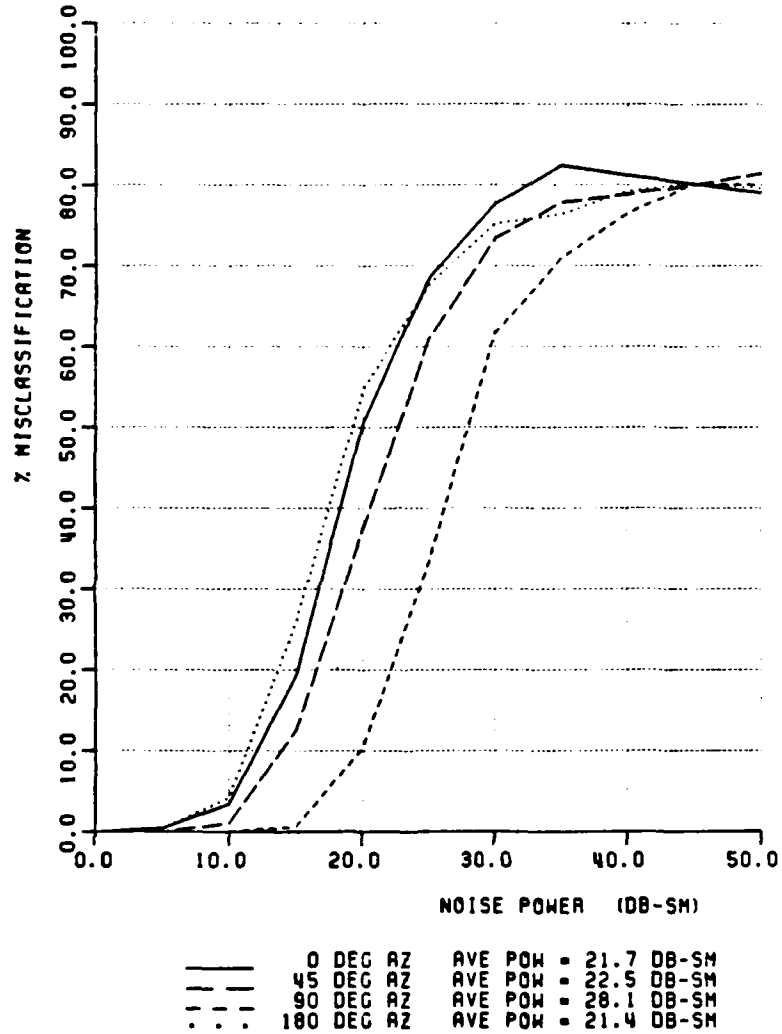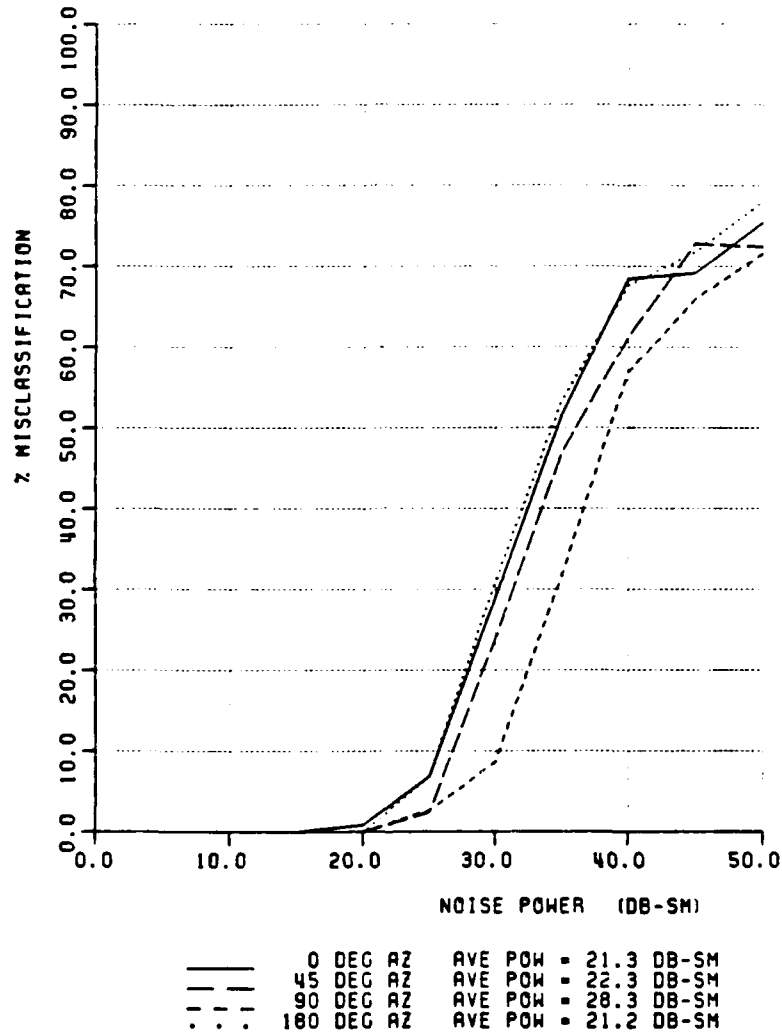

Figure 61: Circular Polarization Diverse Feature Vector (CONCAT)

111

DATA BASE TYPE: AIRCRAFT
FEATURE VECTOR TYPE: LINEAR POL-DIVERSE (SUM)
ALGORITHM TYPE: COHERENT NN
AZIMUTH: KEY   ELEVATION: 0   ROLL: 0
START FREQUENCY: 8 MHZ   STOP FREQUENCY: 16 MHZ
NUMBER OF FREQUENCIES: 4
CATALOG SET VECTORS: 5   TEST SET VECTORS: 5
NUMBER OF EXPERIMENTS: 100
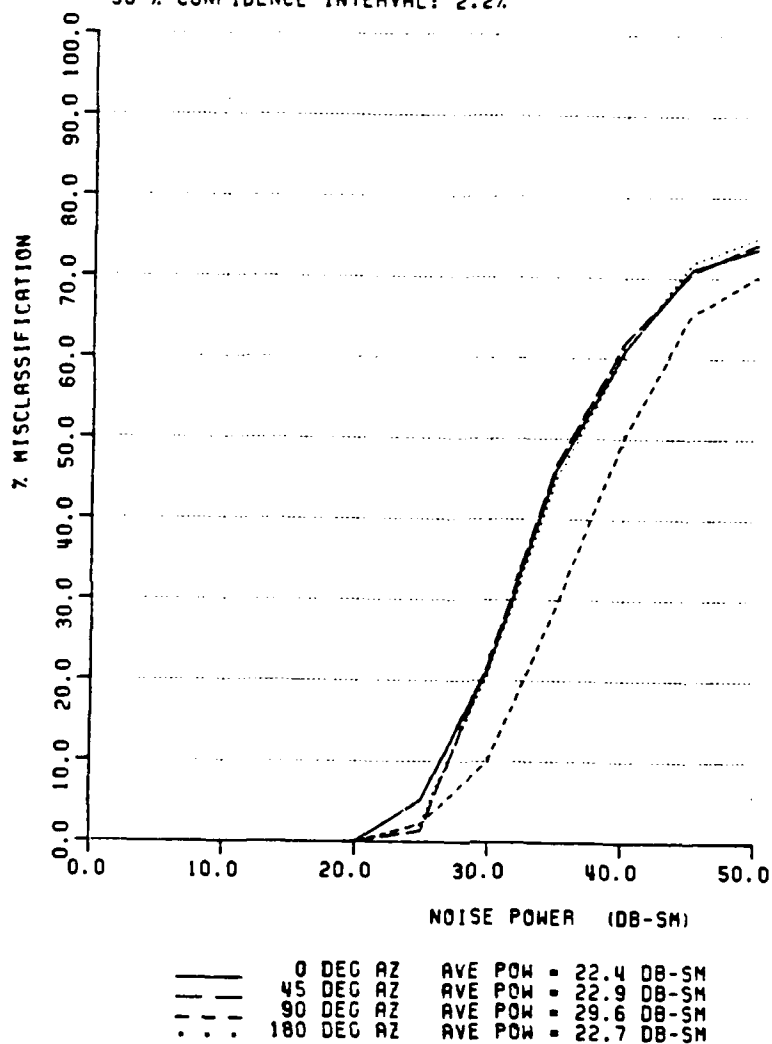90 % CONFIDENCE INTERVAL: 2.2%
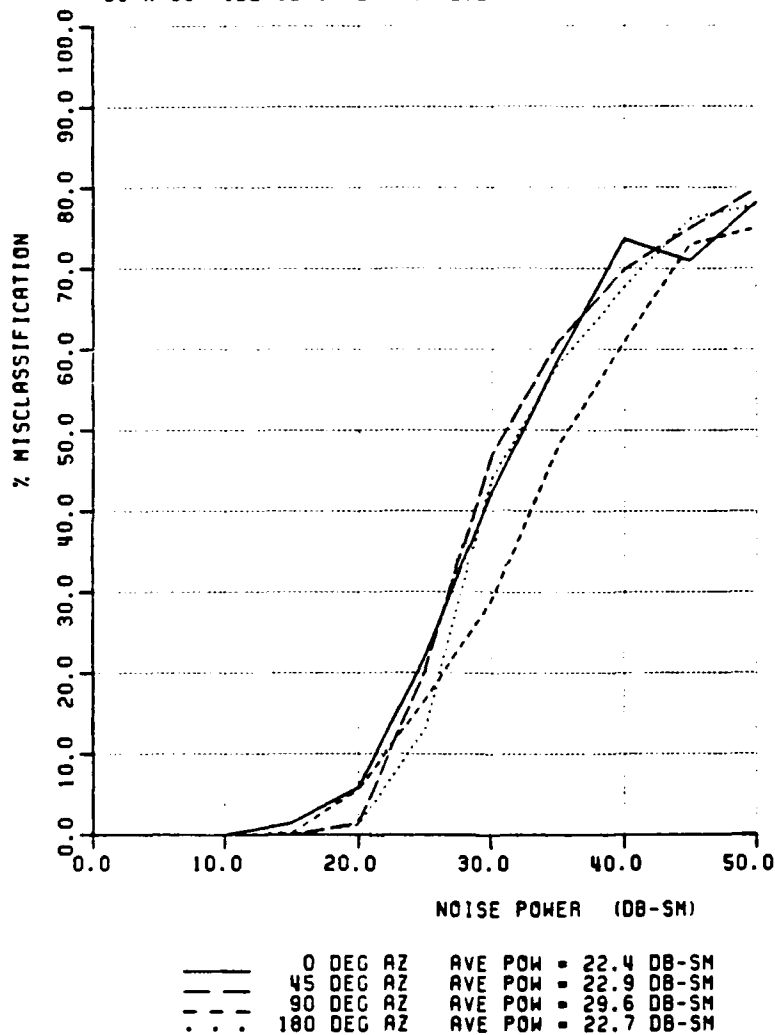
Figure 62: Linear Polarization Diverse Feature Vector (SUM)

112
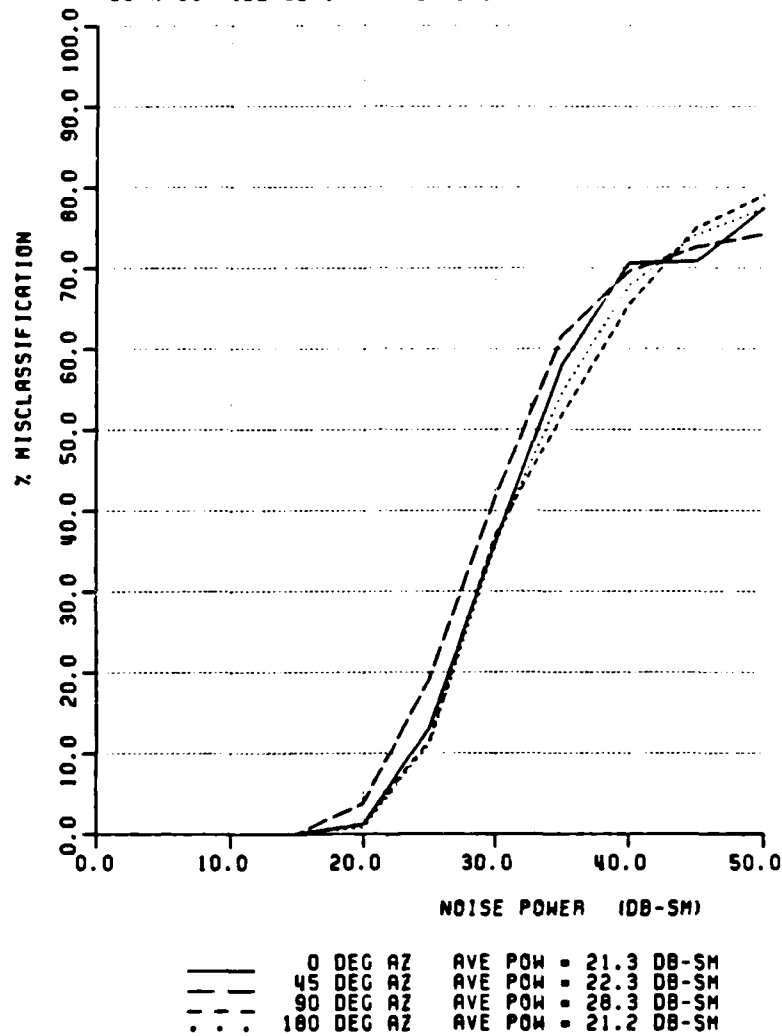
Figure 63: Circular Polarization Diverse Feature Vector (SUM)

113

DATA BASE TYPE: AIRCRAFT
FEATURE VECTOR TYPE: LEFT AXIAL RATIO (LAR)
ALGORITHM TYPE: COHERENT NN
AZIMUTH: KEY   ELEVATION: 0   ROLL: 0
START FREQUENCY: 8 MHZ   STOP FREQUENCY: 16 MHZ
NUMBER OF FREQUENCIES: 10
CATALOG SET VECTORS: 5   TEST SET VECTORS: 5
NUMBER OF EXPERIMENTS: 100
90 % CONFIDENCE INTERVAL: 2.2%

———	0 DEG AZ	AVE POW = 21.7 DB-SM
— —	45 DEG AZ	AVE POW = 22.5 DB-SM
– – –	90 DEG AZ	AVE POW = 28.1 DB-SM
· · ·	180 DEG AZ	AVE POW = 21.4 DB-SM

Figure 64: Feature Vector Type LAR

114

DATA BASE TYPE: AIRCRAFT
FEATURE VECTOR TYPE: RIGHT AXIAL RATIO (RAR)
ALGORITHM TYPE: COHERENT NN
AZIMUTH: KEY   ELEVATION: 0   ROLL: 0
START FREQUENCY: 8 MHZ   STOP FREQUENCY: 16 MHZ
NUMBER OF FREQUENCIES: 10
CATALOG SET VECTORS: 5   TEST SET VECTORS: 5
NUMBER OF EXPERIMENTS: 100
90 % CONFIDENCE INTERVAL: 2.2%

NOISE POWER   (DB-SM)

```
———          0 DEG AZ    AVE POW = 21.6 DB-SM
— —         45 DEG AZ    AVE POW = 21.1 DB-SM
— — —       90 DEG AZ    AVE POW = 29.4 DB-SM
. . .      180 DEG AZ    AVE POW = 21.6 DB-SM
```

Figure 65: Feature Vector Type RAR

115

DATA BASE TYPE: AIRCRAFT
FEATURE VECTOR TYPE: AXIAL RATIO CONCAT
ALGORITHM TYPE: COHERENT NN
AZIMUTH: KEY   ELEVATION: 0   ROLL: 0
START FREQUENCY: 8 MHZ   STOP FREQUENCY: 16 MHZ
NUMBER OF FREQUENCIES: 10
CATALOG SET VECTORS: 5   TEST SET VECTORS: 5
NUMBER OF EXPERIMENTS: 100
90 % CONFIDENCE INTERVAL: 2.2%

		AVE POW = 21.7 DB-SM
————	0 DEG AZ	AVE POW = 21.7 DB-SM
— —	45 DEG AZ	AVE POW = 22.1 DB-SM
— — —	90 DEG AZ	AVE POW = 28.5 DB-SM
. . .	180 DEG AZ	AVE POW = 21.2 DB-SM

Figure 66: Concatenation of Axial Ratio Feature Vectors

116

Figure 67: 0, 10, 20, 30 Aspect Misclassification Results

117

DATA BASE TYPE: AIRCRAFT
FEATURE VECTOR TYPE: MM
ALGORITHM TYPE: COHERENT NN
AZIMUTH: KEY   ELEVATION: 0   ROLL: 0
START FREQUENCY: 8 MHZ   STOP FREQUENCY: 38 MHZ
NUMBER OF FREQUENCIES: 10
CATALOG SET VECTORS: 5   TEST SET VECTORS: 5
NUMBER OF EXPERIMENTS: 100
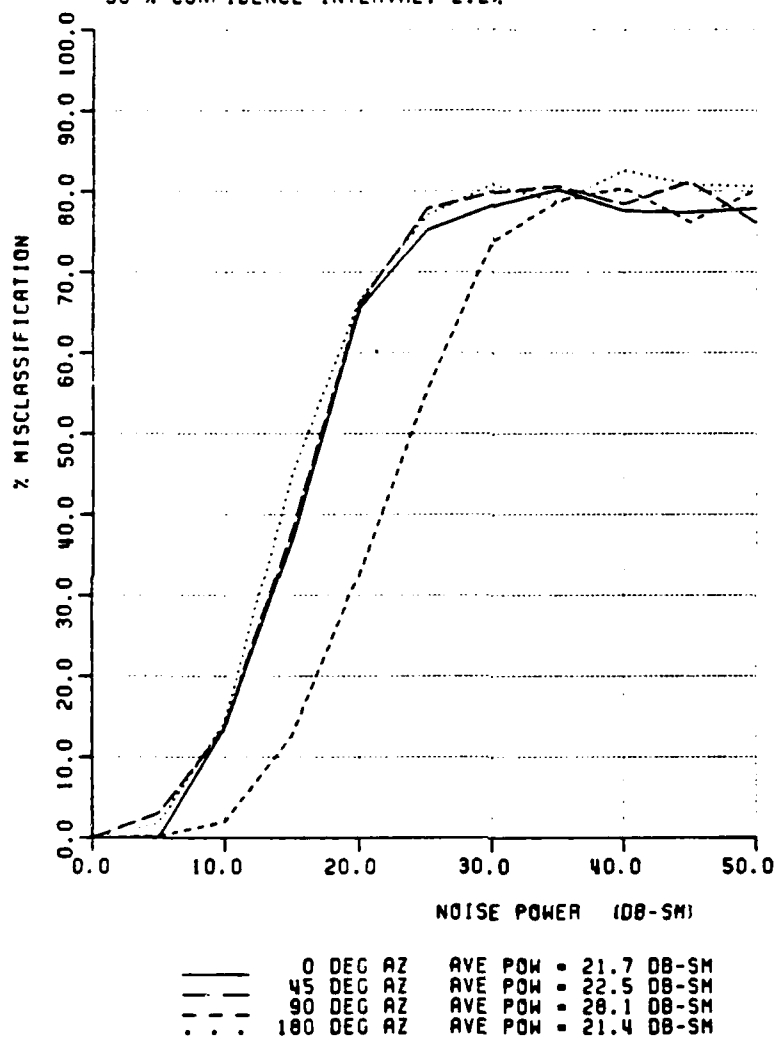90 % CONFIDENCE INTERVAL: 2.2%

40 DEG AZ   AVE POW = 25.4 DB-SM
50 DEG AZ   AVE POW = 21.7 DB-SM
60 DEG AZ   AVE POW = 22.0 DB-SM
70 DEG AZ   AVE POW = 25.6 DB-SM

Figure 68: 40, 50, 60, 70 Aspect Misclassification Results

118

DATA BASE TYPE: AIRCRAFT
FEATURE VECTOR TYPE: HH
ALGORITHM TYPE: COHERENT NN
AZIMUTH: KEY   ELEVATION: 0   ROLL: 0
START FREQUENCY: 8 MHZ   STOP FREQUENCY: 38 MHZ
NUMBER OF FREQUENCIES: 10
CATALOG SET VECTORS: 5   TEST SET VECTORS: 5
NUMBER OF EXPERIMENTS: 100
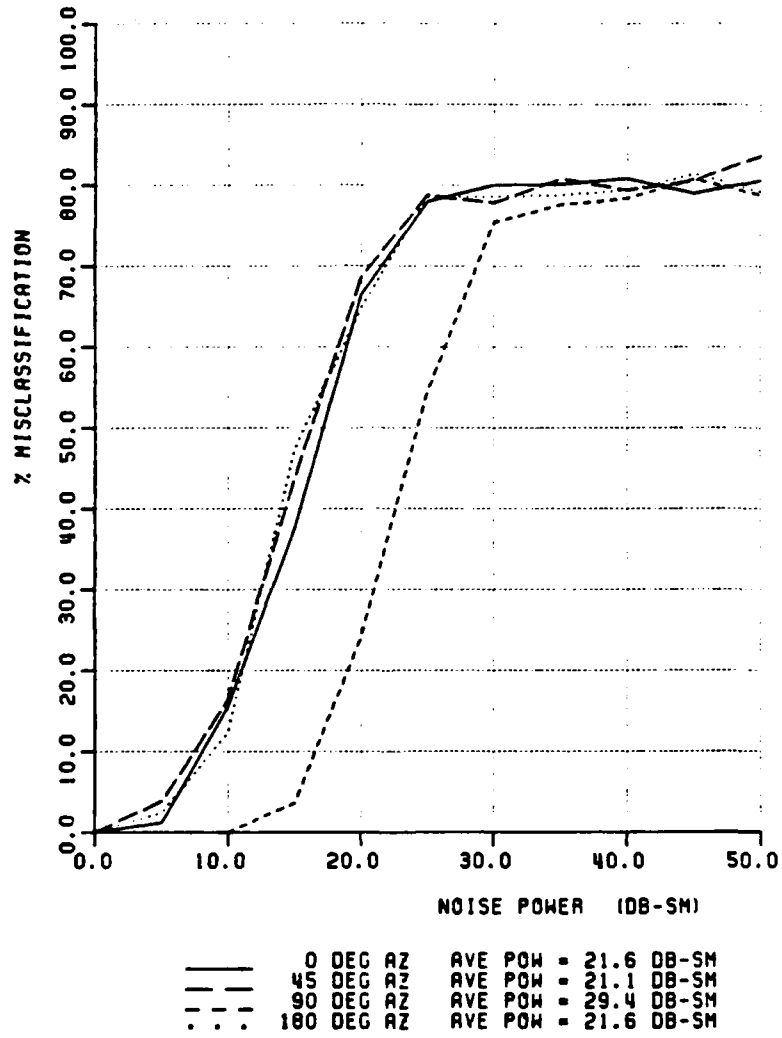90 % CONFIDENCE INTERVAL: 2.2%

```
_____    80 DEG AZ    AVE POW = 28.2 DB-SM
_  _  _    90 DEG AZ    AVE POW = 32.9 DB-SM
_ _ _     100 DEG AZ    AVE POW = 27.5 DB-SM
. . .     110 DEG AZ    AVE POW = 25.3 DB-SM
```

Figure 69: 80, 90, 100, 110 Aspect Misclassification Results

119

DATA BASE TYPE: AIRCRAFT
FEATURE VECTOR TYPE: MM
ALGORITHM TYPE: COHERENT NN
AZIMUTH: KEY   ELEVATION: 0   ROLL: 0
START FREQUENCY: 8 MHZ   STOP FREQUENCY: 39 MHZ
NUMBER OF FREQUENCIES: 10
CATALOG SET VECTORS: 5   TEST SET VECTORS: 5
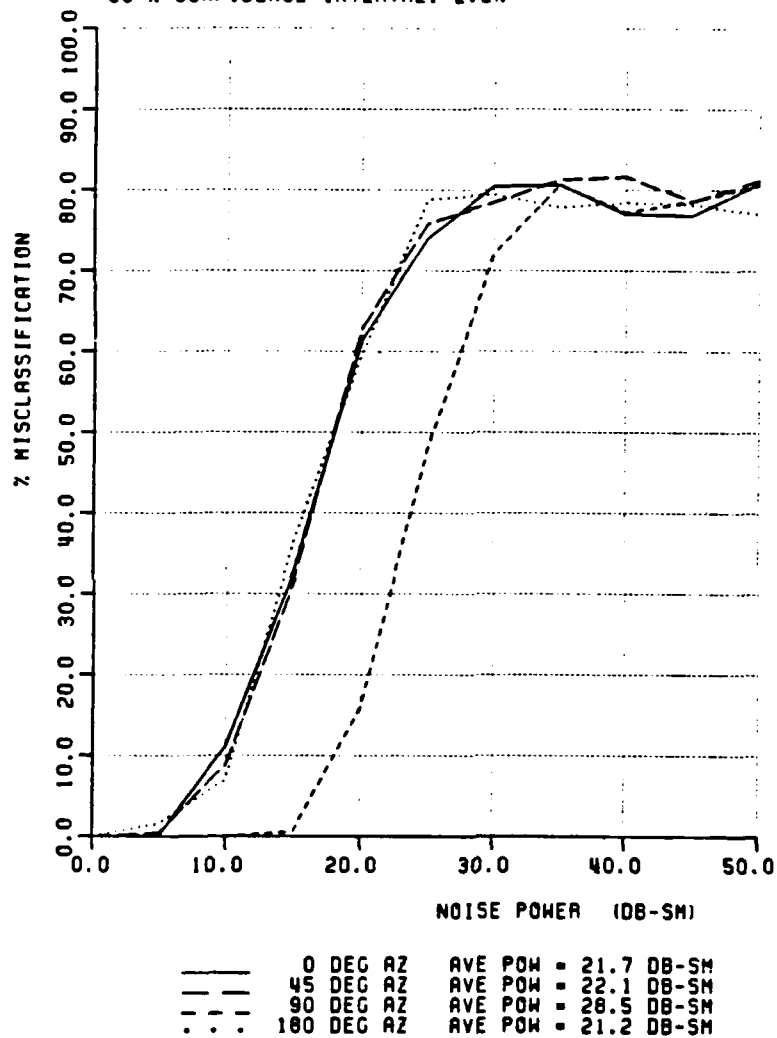NUMBER OF EXPERIMENTS: 100
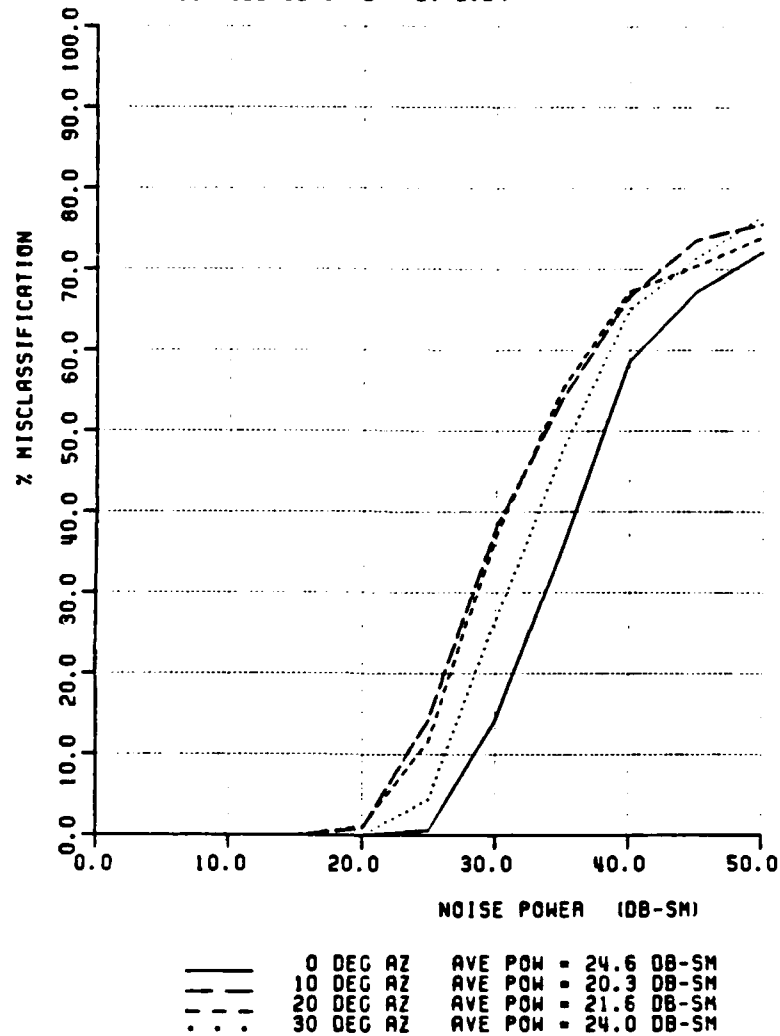90 % CONFIDENCE INTERVAL: 2.2%

```
_____   150 DEG AZ    AVE POW = 23.1 DB-SM
_____   160 DEG AZ    AVE POW = 22.9 DB-SM
_ _ _     170 DEG AZ    AVE POW = 22.6 DB-SM
. . .     180 DEG AZ    AVE POW = 23.9 DB-SM
```
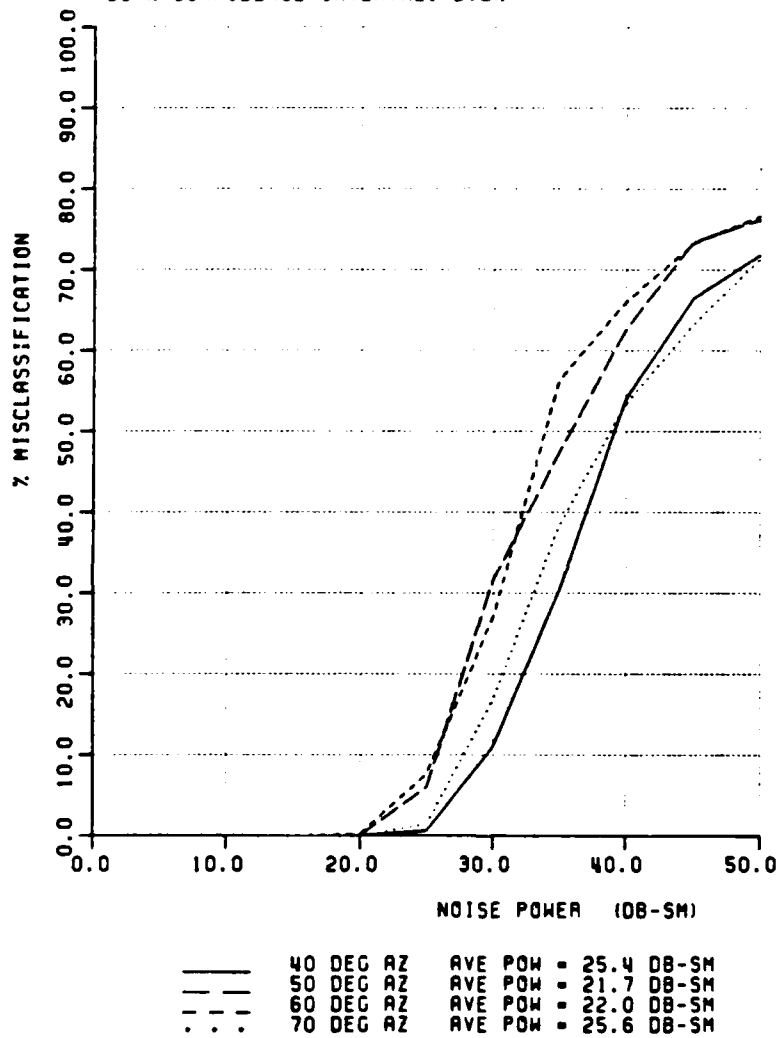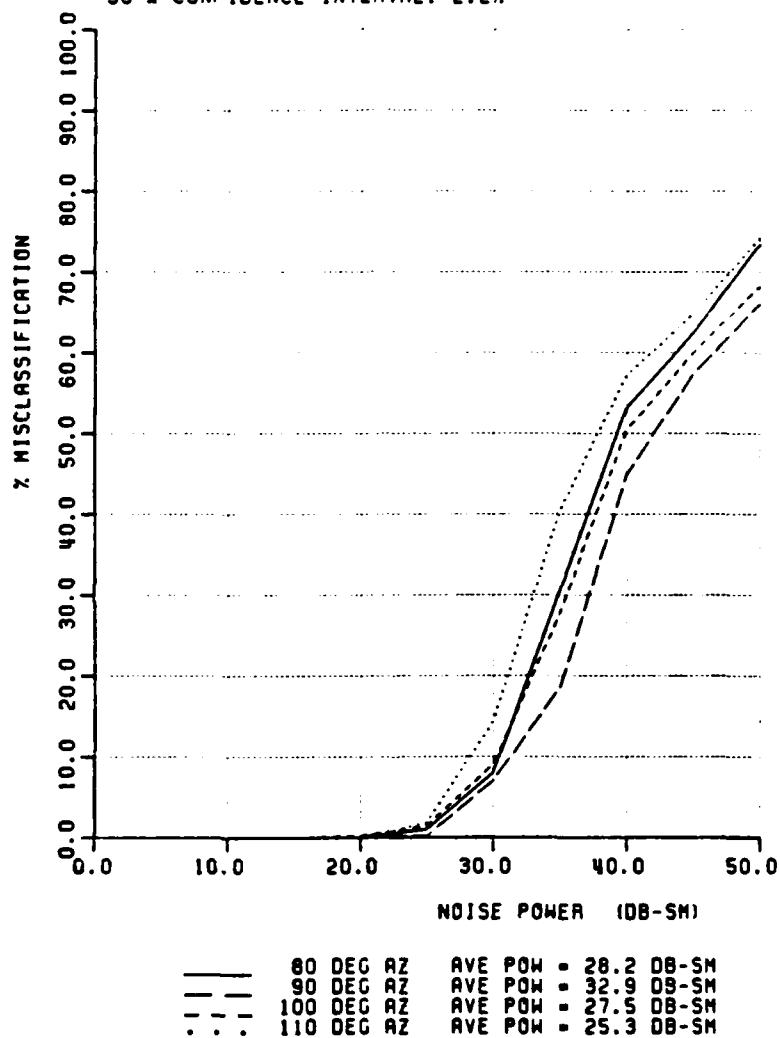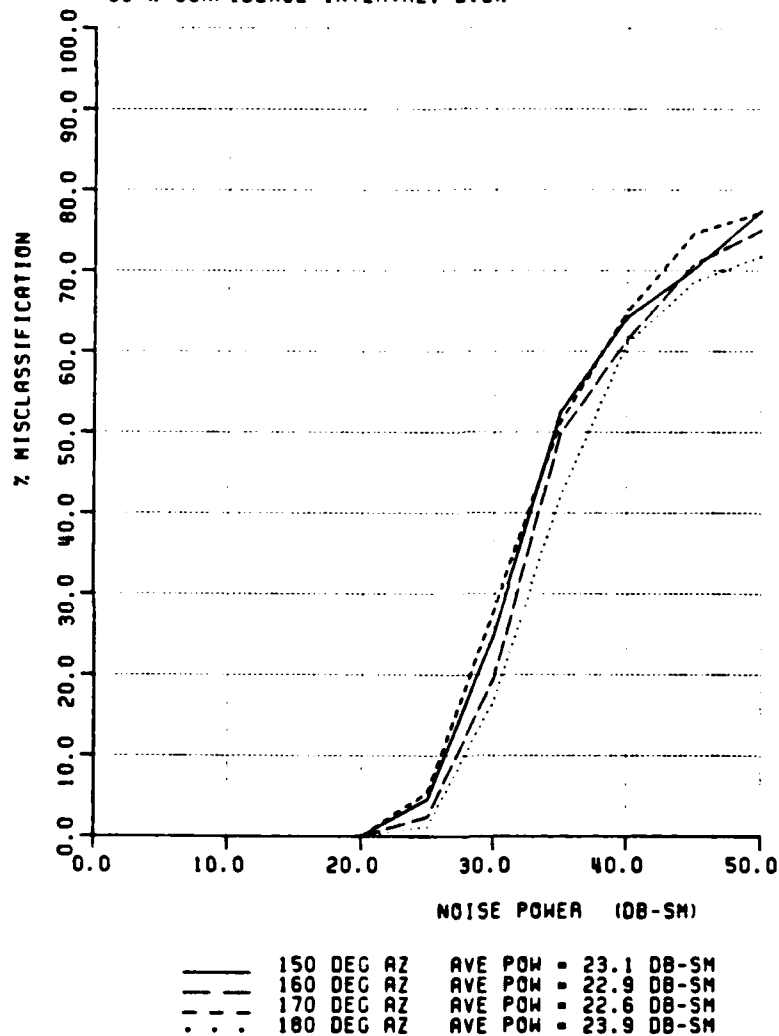
Figure 70: 150, 160, 170, 180 Aspect Misclassification Results

120

```
8.0 - 38.0 MHz    10 Frequencies

Nearest Neighbor Algorithm - Vector "COHERENT" distance metric

   Classification Table for Noise power =  25.00 DBSM

TT#\CT#   1    2    3    4    5    6    7    8    9   10    % MIS-CLASS
        ---------
  1     | 86   11 |  0    1    0    1    0    1    0    0      3.00
        |         |
  2     |  7   67 |  0    5    2    8    3    8    0    0     26.00
        ---------|---------
  3        0    1 | 95    2 |  1    0    0    0    0    1      3.00
                 |         |
  4        1    6 |  2   83 |  2    1    0    3    1    1     15.00
                 ---------|---------
  5        1    0    0    1 | 97    0 |  0    0    1    0      3.00
                          |         |
  6        0    7    0    0 |  2   84 |  6    0    0    1     14.00
                          ---------|---------
  7        0    2    0    3    0    5 | 77   13 |  0    C     10.00
                                    |         |
  8        1    7    0    6    0    1 | 10   75 |  0    0     15.00
                                    ---------|---------
  9        0    0    0    1    0    0    0    0 | 97    2 |    1.00
                                             |         |
 10        0    0    2    0    0    0    0    0 |  0   98 |    2.00
                                             ---------
```

Average misclassification percentage :   9.20 %

Misclassification percentage is based on the test targets name.

Figure 71: Example; Double Angle Confusion Matrix

121

8.0 - 16.0 MHz   10 Frequencies

Nearest Neighbor Algorithm - Vector "COHERENT" distance metric

Classification Table for Noise power = 30.00 DBSM

TT#\CT#	1	2	3	4	5	6	7	8	9	10	11	12	13	14	15	% MIS-CLASS
1	37	16	6	0	6	0	12	14	2	2	3	0	1	0	1	41.00
2	26	27	9	0	6	0	9	17	2	0	2	1	0	0	1	38.00
3	1	13	36	0	8	3	1	8	2	15	11	1	0	0	1	50.00
4	0	0	0	82	2	0	0	0	0	0	0	0	0	14	2	16.00
5	4	2	7	2	46	7	1	5	5	0	4	5	2	2	8	45.00
6	0	1	0	1	7	67	0	0	0	0	12	12	0	0	0	25.00
7	7	5	0	0	2	0	68	6	4	0	0	1	6	1	0	22.00
8	7	6	12	0	3	0	4	46	14	1	4	0	0	0	3	36.00
9	1	1	1	0	6	1	5	8	60	1	2	7	2	1	4	27.00
10	0	3	14	0	0	1	0	3	1	69	9	0	0	0	0	22.00
11	1	1	12	0	3	8	0	4	3	11	49	8	0	0	0	32.00
12	0	0	3	0	1	17	0	0	5	0	7	63	0	0	4	30.00
13	1	0	0	0	0	0	7	2	1	0	0	2	85	2	0	13.00
14	2	0	0	8	2	0	0	1	0	0	0	1	2	69	15	14.00
15	1	0	1	5	6	0	0	2	0	0	2	3	0	7	73	20.00

Average misclassification percentage :   28.73 %

Misclassification percentage is based on the test targets name.

Figure 72: Example; Three Angle Confusion Matrix

122

Figure 73: Double Angle Catalog Misclassification Results

123

DATA BASE TYPE: AIRCRAFT
FEATURE VECTOR TYPE: HH
ALGORITHM TYPE: COHERENT NN
AZIMUTH: KEY   ELEVATION: 0   ROLL: 0
START FREQUENCY: 8 MHZ   STOP FREQUENCY: 38 MHZ
NUMBER OF FREQUENCIES: 10
CATALOG SET VECTORS: 15   TEST SET VECTORS: 15
NUMBER OF EXPERIMENTS: 100
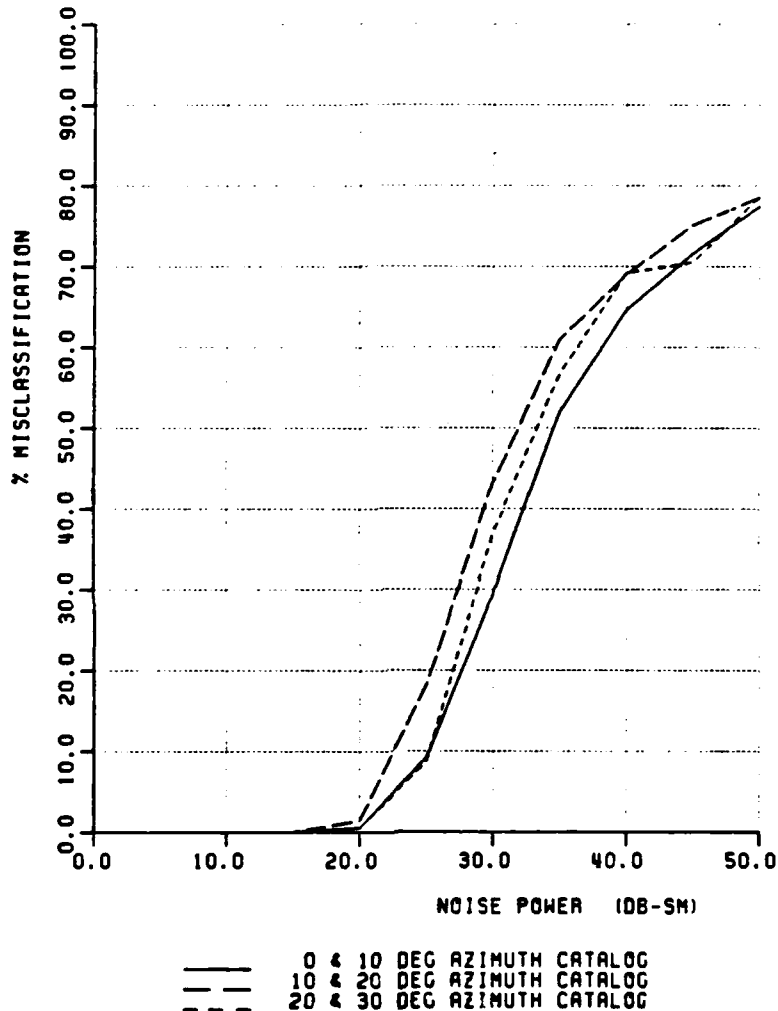90 % CONFIDENCE INTERVAL: 1.3%

0.10.20 DEG AZIMUTH CATALOG
10.20.30 DEG AZIMUTH CATALOG

Figure 74: Three Angle Catalog Misclassification Results

124

DATA BASE TYPE: AIRCRAFT
FEATURE VECTOR TYPE: HH
ALGORITHM TYPE: COHERENT NN
AZIMUTH: KEY   ELEVATION: 0   ROLL: 0
START FREQUENCY: 8 MHZ   STOP FREQUENCY: 38 MHZ
NUMBER OF FREQUENCIES: 10
CATALOG SET VECTORS: 20   TEST SET VECTORS: 20
NUMBER OF EXPERIMENTS: 100
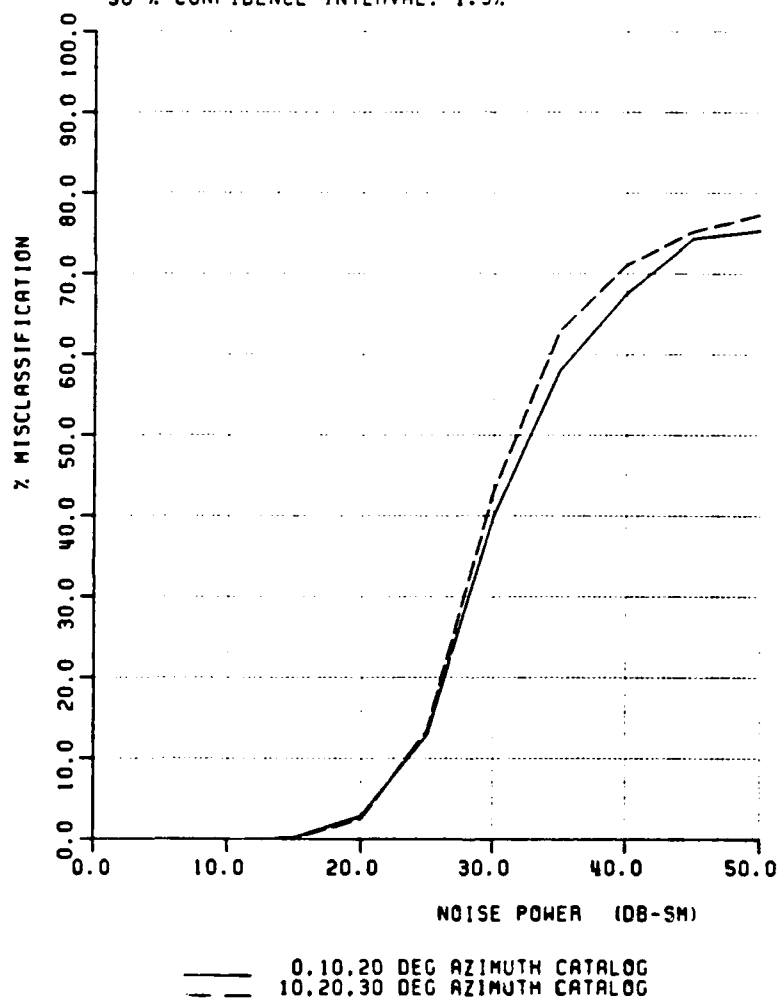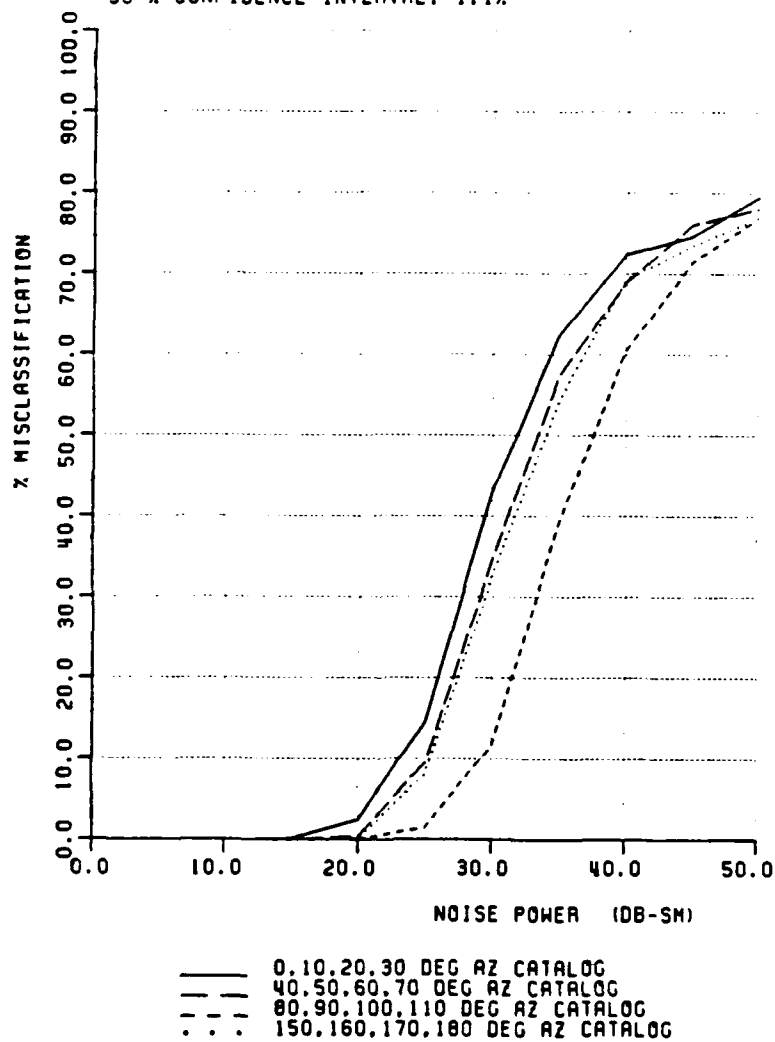90 % CONFIDENCE INTERVAL: 1.1%

———— 0,10,20,30 DEG AZ CATALOG
— — 40,50,60,70 DEG AZ CATALOG
— — 80,90,100,110 DEG AZ CATALOG
· · · 150,160,170,180 DEG AZ CATALOG

Figure 75: Four Angle Catalog Misclassification Results

125

CHAPTER VI

SUMMARY OF RESULTS

This report has examined five aspects of radar target identification techniques applied against a polarization diverse aircraft data base. Plots have been generated to examine misclassification performance levels versus such parameters as: the number of frequencies, frequency bandwidth, classification algorithms, various feature vectors, and an expanded aspect catalog set. Some high points from these five aspects can be summarized as follows:

* The backscattered response of the aircraft scatterer typically die out before 3.5 transit times across the length of the target. To meet Shannon's criterion the sampling rate Δf must satisfy $\Delta f \leq \frac{c}{3.5l}$, where l is the largest dimension of the aircraft. From this criterion the minimum number of frequencies for a given bandwidth can be derived from the following relationship:

Number of Frequencies $= \frac{BW * 3.5l}{c}$, where BW is the frequency bandwidth.

* The lower frequency bands of the aircraft data base provided the highest immunity to the additive white zero mean Gaussian noise model. The near resonance frequency bandwidth of 8 - 16 MHz for the measured polarization schemes of HH and VV contained the largest monostatic radar returns, thus providing the highest noise immunity. As a function of aspect the highest signal energy was encountered most often at broadside incidence (i.e., 90° azimuth, 0° elevation and roll), making the 90° aspect the most immune to additive noise and the best aspect for target

identification.

* The classification algorithm study has shown that the Coherent Nearest Neighbor distance metric provides approximately a 10 dB improvement in noise immunity over the Non-Coherent distance metric and approximately a 5 dB improvement over the Time Domain Cross Correlation method. Although coherent intrinsic (exact) phase measurements are difficult to obtain, a 10 dB improvement is clearly a significant gain in performance.

* Of all the feature vector types examined, the co-pol linear feature vectors FV^{HH} and FV^{VV}, the circular feature vectors FV^{LL}, FV^{RR}, and FV^{RL}, and the polarization diverse feature vector FV^{CONCAT} (both linear and circular), provided the best classification performance against the additive white zero mean Gaussian noise model. Out of the seven feature vectors mentioned above, no one type exhibited any significant advantage in classification performance over the others. However, the circular feature vectors do provide some independence in regard to the roll of the aircraft, especially in the symmetric look angles of nose-on and tail-on. The polarization diverse feature vectors require a smaller number of frequency samples to provide the same classification levels. It also should be metioned that the ratio feature vectors types were not fully examined. The ratio types may provide some additional benefits in a multiplicative noise environment by virtue of the division of the backscattered components.

* Increasing the catalog set by adding additional feature vectors that cover a range of aspects tend to decrease the classification performance level relative to that of the worst single angle catalog set level.

127

REFERENCES

[1] A. A. Ksienski, Y. T. Lin, and L. J. White, "Low Frequency Approach to Target Identification," *Proceedings of the IEEE*, Vol. 63, pp. 1651-1660, December 1975.

[2] A. A. Ksienski, "Target Identification Techniques," *Radar Target Identification Short Course Notes*, The Ohio State University Dept. of Electrical Engineering, Columbus, Ohio, 1975.

[3] A. A. Ksienski and Y. T. Lin, "Airplane Identification From Low Frequency Scattering Data," International IEEE/G-AP Symposium at the Univ. of Ill. October 1972.

[4] E. K. Walton and J. D. Young, "Surface Ship Target Classification Using HF Multifrequency Radar," Final Report 712352-1, The Ohio State University ElectroScience Laboratory, Columbus, Ohio, May 1980.

[5] E. K. Walton, "Processing And Analysis of VHF Radar Data for Target Classification," Final Report 712331-2, The Ohio State University ElectroScience Laboratory, Columbus, Ohio, March 1980.

[6] E. K. Walton, D. L. Moffatt, F. D. Garber, A. J. Kamis, and C. Y. Lai, "NCTR Using A Polarization-Agile Coherent Radar System," Final Report 716559-2, The Ohio State University ElectroScience Laboratory, Columbus, Ohio, January 1986.

[7] F. D. Garber, "Applications of Compact-Range Data to Radar System Simulation and Evaluation," The Ohio State University Dept. of Electrical Engineering, Columbus, Ohio, 1985.

[8] D. L. Moffatt and R. K. Mains, "Detection and Discrimination of Radar Targets," *IEEE Trans. on Antennas and Propagation*, Vol. AP-23, pp. 358-367, May 1975.

[9] C. W. Chuang and D. L. Moffatt, "Natural Resonances of Radar Targets Via Prony's Method and Target Discrimination," *IEEE Transactions on Aerospace and Electronic Systems*, Vol. AES-12, pp. 583-589, November 1976.

[10] S. N. Srihari, "Comparative Evaluation of the Sebestyen and Nearest-Neighbor Classifiers for Radar Aircraft Identification," Technical Report 3815-3, The Ohio State University ElectroScience Laboratory, Columbus, Ohio, June 1976.

[11] Y. T. Lin and A. A. Ksienski, "Identification of Complex Geometrical Shapes by Low-Frequency Radar Returns," *The Radio and Electronic Engineer*, Vol. 46, No. 10, pp. 472-486, October 1976.

[12] H. C. Lin, "Identification of Catalogued and Uncatalogued Classes," Ph.D. Dissertation, The Ohio State University ElectroScience Laboratory, Columbus, Ohio, December 1978.

[13] H. C. Lin and A. A. Ksienski, "Optimum Frequencies for Aircraft Classification," *IEEE Transactions on Aerospace and Electronic Systems*, Vol. AES-17, No. 5, September 1981.

[14] J. S. Chen, "Automatic Target Classification Using HF Multifrequency Radars," Ph.D. Dissertation, The Ohio State University ElectroScience Laboratory, Columbus, Ohio, 1983.

[15] J. S. Chen and E. K. Walton, "Development and Comparison of Two Target Classification Techniques for Resonance Region Radars," *IEEE Transactions on Aerospace and Electronic Systems* , Vol. AES-22, No. 1, pp. 15-22, January 1986.

[16] N. F. Chamberlain, "Surface Ship Classification Using Multipolarization, Multifrequency Sky-Wave Resonance Radar," Technical Report 714190-9, The Ohio State University ElectroScience Laboratory, Columbus, Ohio, 1984.

[17] N. F. Chamberlain, "Ground Vehicle Classification Using Multipolarization, Multifrequency Resonance Radar," Technical Report 714190-10, The Ohio State University ElectroScience Laboratory, Columbus, Ohio, July 1985.

[18] E. K. Walton and J. D. Young, "The Ohio State University Compact Radar Cross-section Measurement Range," *IEEE Trans. on Antennas and Propagation*, Vol. AP-32, No. 11, pp. 1218-1223, November 1984.

[19] D. F. Kimball, "Enhanced Techniques For Broadband Radar Backscatter Measurements," Technical Report 714190-4, The Ohio State University ElectroScience Laboratory, Columbus, Ohio, December 1983.

[20] A. J. Kamis, F. D. Garber, and E. K. Walton, "Radar Target Classification Studies - Software Development and Documentation," Technical Report 716559-1, The Ohio State University ElectroScience Laboratory, Columbus, Ohio, September 1985.

[21] F. J. Harris, "On the Use of Windows for Harmonic Analysis with the Discrete Fourier Transform," *Proceedings of the IEEE*, Vol. 66, pp. 51-81, January 1978.

[22] W. B. Goggins, P. Blacksmith, and G. J. Sletten, "Phase Signature Radars," *IEEE Transactions on Antennas and Propagation*, Vol. AP-22, No. 6, pp. 1218-1223, November 1974.

[23] A. V. Oppenheim and R. W. Schafer, *Digital Signal Processing*, Prentice-Hall, 1975.

[24] M. Abramowitz and I. A. Stegun, ed. *Handbook of Mathematical Functions*, National Bureau of Standards, Washington D.C., 1965.

[25] M. H. DeGroot, *Probability and Statistics*, Addison-Wesley, 1975.

APPENDIX A

BACKSCATTERED COEFFICIENTS

A.1 Linear Polarized Measured Coefficients

The RSSE feature vectors are derived by using various linear and non-linear combinations of the complex backscattered coefficients from six simulated RSSE radar types. Three of these feature vectors were obtained from direct measurements on scale model aircraft in the OSU compact range. They are the linear polarized complex backscattered coefficients: $\tilde{\sigma}_{HH}^{BS}$, $\tilde{\sigma}_{VV}^{BS}$, and $\tilde{\sigma}_{VH}^{BS}$.

A simple representation of the measurement process for the transmit horizontal, receive horizontal, backscattered coefficient, $\tilde{\sigma}_{HH}^{BS}$, can be illustrated as shown in Figure 76.

For time harmonic fields, we have: $\quad \tilde{E}_t = E_o e^{jwt}$

In the far field, we can write:

$$\vec{\tilde{E}}^i = \vec{\tilde{E}}^t \big|_{z=z_i} = \hat{x}\tilde{E}_t \epsilon^{-jkz_i} = \vec{\tilde{E}}_H^i$$

$$\left[\tilde{E}^s\right] = \left[\sqrt{\frac{\tilde{\sigma}}{4\pi}}\right]\left[\tilde{E}^i\right]\epsilon^{-jks}$$

So;

$$\left[\begin{array}{c} \tilde{E}_H^s \\ \tilde{E}_V^s \end{array}\right] = \left[\begin{array}{cc} \sqrt{\frac{\tilde{\sigma}_{HH}}{4\pi}} & \sqrt{\frac{\tilde{\sigma}_{HV}}{4\pi}} \\ \sqrt{\frac{\tilde{\sigma}_{VH}}{4\pi}} & \sqrt{\frac{\tilde{\sigma}_{VV}}{4\pi}} \end{array}\right]\left[\begin{array}{c} \tilde{E}_H^i \\ 0 \end{array}\right]\epsilon^{-jks}$$

The Matrix multipication yields:

$$\vec{\tilde{E}}^r = \vec{\tilde{E}}^{BS}\big|_{s=z_s} = \hat{x}\tilde{E}_H^i\sqrt{\frac{\tilde{\sigma}_{HH}^{BS}}{4\pi}}\epsilon^{-jkz_s} + \hat{y}\tilde{E}_H^i\sqrt{\frac{\tilde{\sigma}_{VH}^{BS}}{4\pi}}\epsilon^{-jkz_s}$$

$$= \vec{\tilde{E}}_H^{BS} + \vec{\tilde{E}}_V^{BS}$$

130

At the terminals of the Mono-static Horizontal Polarized Radar, we have:

$$\vec{E}_r = \vec{E}^r \odot \hat{x} = \vec{E}_H^{BS} \sqrt{\frac{\tilde{\sigma}_{HH}^{\overline{BS}}}{4\pi}} = \vec{E}_t \sqrt{\frac{\tilde{\sigma}_{HH}^{\overline{BS}}}{4\pi}} e^{-jk(z_i+z_s)}$$

Calibrating out the Radar Range dependence (ie. dropping the $e^{-jk(z_i+z_s)}$ term), we obtain;

$$\sqrt{4\pi}\frac{\tilde{E}_r}{E_t} = \sqrt{\tilde{\sigma}_{HH}^{BS}} \quad \text{or} \quad \tilde{\sigma}_{HH}^{BS} = 4\pi\frac{\tilde{E}_r^2}{\tilde{E}_t^2}$$

Similarly, we can illustrate the measurment process for the other two backscattered coefficients: $\tilde{\sigma}_{VV}^{BS}$, and $\tilde{\sigma}_{VH}^{BS}$.

Also; $\tilde{\sigma}_{VH}^{BS} = \tilde{\sigma}_{HV}^{BS}$ by the reciprocity theorem.

A.2 Circular Polarized Synthesized Coefficients

To obtain the circular polarized feature vectors, synthesized circular polarized radars are created by using the linear polarized backscattered coefficients in a polarization transformation. The derivation of the Left - Left circular antenna shown in Figure 77 is as follows:

Transmitting Left Circular Polarization (LCP)

$$\epsilon(t, z) = \left(\frac{E_0}{\sqrt{2}}\right) [\hat{x} \sin(wt - kz) + \hat{y} \cos(wt - kz)]$$

Or in Phasor Notation;

$$\vec{E}^t = \hat{x}\left(\frac{\tilde{E}_t}{\sqrt{2}}\right) e^{-j(kz+90°)} + \hat{y}\left(\frac{\tilde{E}_t}{\sqrt{2}}\right) e^{-jkz} = \frac{\tilde{E}_t}{\sqrt{2}} [-j\hat{x} + \hat{y}] e^{-jkz}$$

$$= -j\vec{E}_H^t + \vec{E}_V^t$$

$$\vec{E}^i = \vec{E}^t |_{z=z_i} = \left(\frac{\tilde{E}_t}{\sqrt{2}}\right) e^{-jkz_i} [-j\hat{x} + \hat{y}] = -j\vec{E}_H^i + \vec{E}_V^i$$

$$\left[\tilde{E}^s\right] = \left[\sqrt{\frac{\tilde{\sigma}}{4\pi}}\right] \left[\tilde{E}^i\right] e^{-jks}$$

So;

$$\begin{bmatrix} \tilde{E}_H^s \\ \tilde{E}_V^s \end{bmatrix} = \begin{bmatrix} \sqrt{\frac{\tilde{\sigma}_{HH}}{4\pi}} & \sqrt{\frac{\tilde{\sigma}_{HV}}{4\pi}} \\ \sqrt{\frac{\tilde{\sigma}_{VH}}{4\pi}} & \sqrt{\frac{\tilde{\sigma}_{VV}}{4\pi}} \end{bmatrix} \begin{bmatrix} -j\tilde{E}_H^i \\ \tilde{E}_V^i \end{bmatrix} e^{-jks}$$

The Matrix multipication yields:

$$\vec{E}^r = \vec{E}^{BS} |_{s=z_s} = \hat{x} \left[-j\tilde{E}_H^i \sqrt{\frac{\tilde{\sigma}_{HH}^{BS}}{4\pi}} + \tilde{E}_V^i \sqrt{\frac{\tilde{\sigma}_{HV}^{BS}}{4\pi}}\right] e^{-jkz_s}$$

$$+ \hat{y} \left[-j\tilde{E}_H^i \sqrt{\frac{\tilde{\sigma}_{VH}^{BS}}{4\pi}} + \tilde{E}_V^i \sqrt{\frac{\tilde{\sigma}_{HH}^{BS}}{4\pi}}\right] e^{-jkz_s}$$

$$= \vec{E}_H^r + \vec{E}_V^r$$

At the terminals of the Mono-static LCP Synthesized Radar, we have:

$$\tilde{E}_r = \left(\vec{\tilde{E}}_H^r + \vec{\tilde{F}}_V^r\right) \odot \underbrace{\left(\frac{-j\hat{x} + \hat{y}}{\sqrt{2}}\right)}_{antenna} = \tfrac{1}{\sqrt{2}}\left(-j\tilde{E}_H^r + \tilde{E}_V^r\right)$$

$$\tilde{E}_r = \tfrac{1}{\sqrt{2}}\left[\tilde{E}_H^i\sqrt{\tilde{\sigma}_{HH}^{BS}} - j\tilde{E}_V^i\sqrt{\tilde{\sigma}_{HV}^{\overline{BS}}} - j\tilde{E}_H^i\sqrt{\tilde{\sigma}_{VH}^{\overline{BS}}} + \tilde{E}_V^i\sqrt{\tilde{\sigma}_{VV}^{BS}}\right]e^{-jkz_s}$$

$$\tilde{E}_r = \frac{\tilde{E}_t}{2\sqrt{4\pi}}\left[-\sqrt{\tilde{\sigma}_{HH}^{BS}} + \sqrt{\tilde{\sigma}_{VV}^{BS}} - 2j\sqrt{\tilde{\sigma}_{VH}^{BS}}\right]e^{-jk(z_i + z_s)}$$

Calibrating out the Radar Range dependence (ie. dropping the $e^{-jk(z_i + z_s)}$ term), we obtain;

$$\sqrt{\tilde{\sigma}_{LL}^{BS}} = \sqrt{4\pi}\frac{\tilde{E}_r}{\tilde{E}_t} = \tfrac{1}{2}\left[\sqrt{\tilde{\sigma}_{VV}^{BS}} - \sqrt{\tilde{\sigma}_{HH}^{BS}}\right] - j\sqrt{\tilde{\sigma}_{VH}^{BS}}$$

Similarly, we can derive $\sqrt{\tilde{\sigma}_{RR}^{BS}}$, and $\sqrt{\tilde{\sigma}_{RL}^{BS}}$ as;

$$\sqrt{\tilde{\sigma}_{RR}^{BS}} = \tfrac{1}{2}\left[\sqrt{\tilde{\sigma}_{HH}^{BS}} - \sqrt{\tilde{\sigma}_{VV}^{BS}}\right] - j\sqrt{\tilde{\sigma}_{VH}^{BS}}$$

$$\sqrt{\tilde{\sigma}_{LR}^{BS}} = \sqrt{\tilde{\sigma}_{RL}^{BS}} = \tfrac{-j}{2}\left[\sqrt{\tilde{\sigma}_{VV}^{BS}} + \sqrt{\tilde{\sigma}_{HH}^{BS}}\right]$$
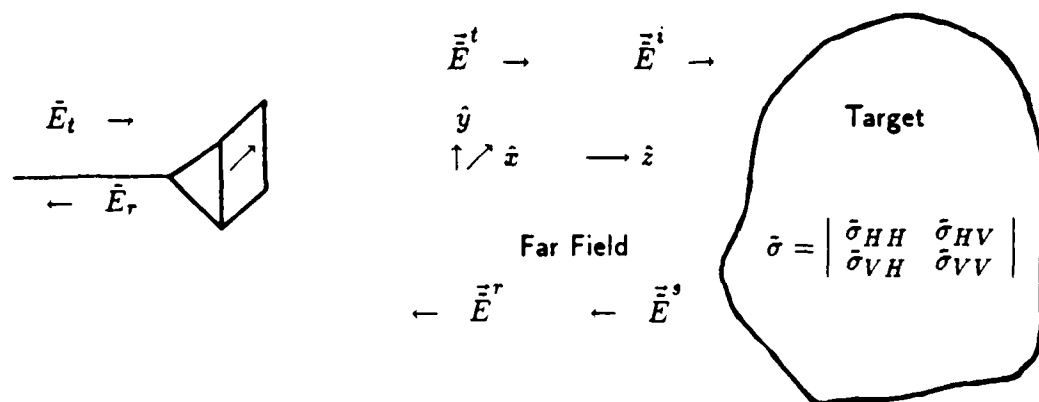
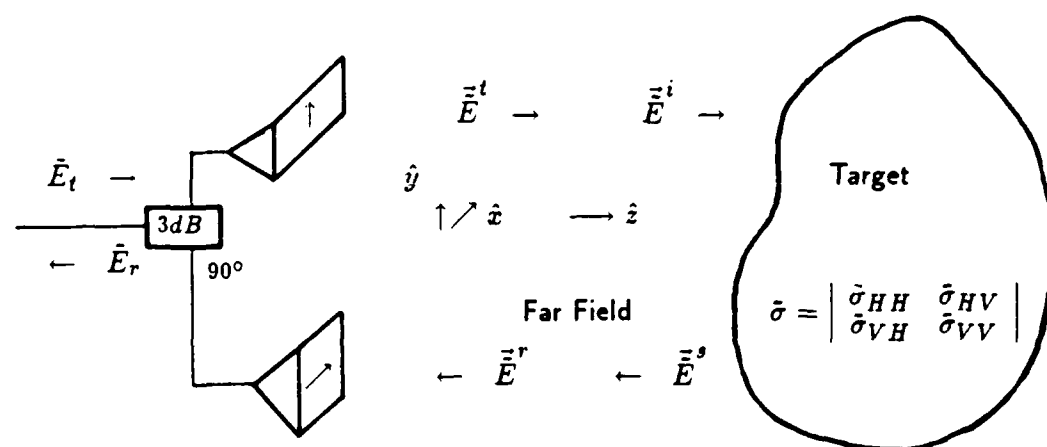Figure 76: Representation of the Measurement Process for the $\tilde{\sigma}_{HH}^{BS}$ Coefficient

Figure 77: Representation of the Measurement Process for the $\tilde{\sigma}_{LL}^{BS}$ Coefficient

134

END

6 — 81

DTIC